

SELF-RECURRENT WAVELET NEURAL NETWORK BASED INDIRECT
ADAPTIVE CONTROL ARCHITECTURE WITH MODIFIED ADAPTIVE
LEARNING RATES FOR THE SPEED CONTROL OF MOTION PLATFORMS

A THESIS SUBMITTED TO
THE GRADUATE SCHOOL OF NATURAL AND APPLIED SCIENCES
OF
MIDDLE EAST TECHNICAL UNIVERSITY

BY

EVİRİM ONUR ARI

IN PARTIAL FULFILLMENT OF THE REQUIREMENTS
FOR
THE DEGREE OF DOCTOR OF PHILOSOPHY
IN
ELECTRICAL AND ELECTRONICS ENGINEERING

FEBRUARY 2015

Approval of the thesis:

**SELF-RECURRENT WAVELET NEURAL NETWORK BASED INDIRECT
ADAPTIVE CONTROL ARCHITECTURE WITH MODIFIED ADAPTIVE
LEARNING RATES FOR THE SPEED CONTROL OF MOTION PLATFORMS**

submitted by **EVİRİM ONUR ARI** in partial fulfillment of the requirements for the degree of **Doctor of Philosophy in Electrical and Electronics Engineering Department, Middle East Technical University** by,

Prof. Dr. Gülbin Dural
Dean, Graduate School of **Natural and Applied Sciences**

Prof. Dr. Gönül Turhan Sayan
Head of Department, **Electrical and Electronics Engineering**

Prof. Dr. Erol Kocaođlan
Supervisor, **Electrical and Electronics Engineering**

Examining Committee Members:

Prof. Dr. Mübeccel Demirekler
Electrical and Electronics Engineering Department, METU

Prof. Dr. Erol Kocaođlan
Electrical and Electronics Engineering Department, METU

Prof. Dr. Eres Söylemez
Mechanical Engineering Department, METU

Prof. Dr. Kemal Leblebiciođlu
Electrical and Electronics Engineering Department, METU

Assist. Prof. Dr. Yakup Özkazanç
Electrical and Electronics Eng. Dep., Hacettepe Uni.

Date:

I hereby declare that all information in this document has been obtained and presented in accordance with academic rules and ethical conduct. I also declare that, as required by these rules and conduct, I have fully cited and referenced all material and results that are not original to this work.

Name, Last Name: EVRİM ONUR ARI

Signature :

ABSTRACT

SELF-RECURRENT WAVELET NEURAL NETWORK BASED INDIRECT ADAPTIVE CONTROL ARCHITECTURE WITH MODIFIED ADAPTIVE LEARNING RATES FOR THE SPEED CONTROL OF MOTION PLATFORMS

Ari, Evrim Onur

Ph.D., Department of Electrical and Electronics Engineering

Supervisor : Prof. Dr. Erol Kocaođlan

February 2015, 151 pages

Motion platforms are widely employed in military systems for the purpose of controlling payloads like optical sensors, antennas, guns etc. One of the most critical components of these platforms is the motion control sub-system which is responsible for controlling the speed of the platform. In this thesis, the components of the speed control are investigated in detail and finally a novel control architecture was proposed in order to improve the transient performance of the speed control without any adverse effect on its robustness. This architecture is a form of indirect adaptive control using Self-Recurrent Wavelet Neural Networks (SRWNNs). The architecture is enhanced by a novel parameter update method in order to guarantee fast convergence, and an additional algorithm for structural evolution. The performance of the proposed architecture has been shown with simulations and verified with experiments. Moreover, its performance is compared with several robust RST-based control designs.

Keywords: Motion Platforms, Lumped-Mass Systems, Multi-body System, Wavelet Networks, Adaptive Control

ÖZ

HAREKETLİ PLATFORMLARIN HIZ DENETİMİ İÇİN KENDİNİ TEKRARLAYAN DALGACIK SINIR AĞI TEMELLİ DEĞİŞTİRİLMİŞ UYARLAMALI ÖĞRENME HIZLI DOLAYLI UYUMLU DENETİM YAPISI

Arı, Evrim Onur

Doktora, Elektrik ve Elektronik Mühendisliği Bölümü

Tez Yöneticisi : Prof. Dr. Erol Kocaođlan

Şubat 2015 , 151 sayfa

Askeri sistemlerde hareketli platformlar optik sensör, anten, silah gibi faydalı yüklerin kontrolü amacıyla sıkça kullanılmaktadır. Bu platformların en önemli bileşenlerinden bir tanesi hareket denetim alt sistemidir ve temel olarak platformun hız denetiminden sorumludur. Bu tezde, bu tip hareketli platformların hız denetimine yönelik olarak detaylı inceleme ve deneyler gerçekleştirilmiş, sonuç olarak da hız denetimi geçiş rejimi başarımını gürbüzlüğü olumsuz etkilemeksizin iyileştiren bir denetim mimarisi önerilmiştir. Bu mimari Kendini-Tekrarlayan Dalgacık Yapay Sinir Ağı yapılarını kullanan bir dolaylı uyumlama denetlecine hızlı kararlı durumu garantileyen yeni bir parametre güncelleme yöntemi ve yapısal öğrenme algoritması eklenerek oluşturulmuştur. önerilen denetim mimarisinin başarımı gerek benzetim, gerekse deneylerle sınanmıştır. Ayrıca, önerilen yöntemin RST temelli gürbüz denetim algoritmaları ile başarım kıyaslaması yapılmış ve tüm bulgular bu tezde raporlanmıştır.

Anahtar Kelimeler: Hareketli Platformlar, Çok Kütleli Sistemler, Esnek Elemanlı Sistemler, Dalgacık Ağları, Uyumlu Denetim

Durmaksızın sorarız,
Ta ki bir avuç toprak,
Ağzımızı kapatana kadar,
Peki ama bu mudur yanıt?
HEINRICH HEINE

Aylin, Melis & DEVRİM'e...

ACKNOWLEDGMENTS

I believe that making a Ph.D. is like running a marathon: This dissertation is the "final 42 kms" of it; but there is a planned, disciplined, very intense effort during more than 1000 kms behind it. It is this effort and the ability to give this effort which makes the athlete to be able to run the race seamlessly; but more importantly stronger in life, against anything encountered thereupon. I hope this thesis work will also provide me with the same wisdom during my engineering career. As for the acknowledgements: First of all I would like to thank to my thesis supervisor Prof. Erol Kocaođlan for his great guidance and endless understanding during our cooperative study of three years. I feel really very lucky for having the chance to study with such a great mentor. Prof. Eres Söylemez and Prof. Kemal Leblebiciođlu have also had very valuable contributions on this study by their technical critics and enlightening ideas during our committee meetings. I am also very thankful to Aselsan Inc. for presenting me such a great medium in order to conduct my studies while working. Special thanks goes to Bülent Bilgin, and Burak Gürcan for their "all time encouragement and supervision" whenever I lost my motivation. I would like to thank to my team mates Dr. Murat Gültekin, Zafer Yumrukçal and Ercan Çandır for keeping me isolated from day long duties whenever I needed spare time to concentrate on this thesis work. Besides all these engineering team mates, I am also very lucky to have a great family media during my life, which allowed me to succeed in completing my Ph.D.: I would like to thank to my father and my mother for their endless efforts aiming their children to be well educated; my older brother for being a role model in scientific curiosity. Last but not least, my thanks goes to my dear wife Aylin and our beloved daughter Melis. I am very proud to be husband of such a great person, and father of such an energetic and cheerful daughter. I also appreciate them for sacrificing their valuable time in order for me to study on this thesis work.

TABLE OF CONTENTS

ABSTRACT	v
ÖZ	vi
ACKNOWLEDGMENTS	viii
TABLE OF CONTENTS	ix
LIST OF TABLES	xiii
LIST OF FIGURES	xiv
LIST OF ABBREVIATIONS	xxi
LIST OF SYMBOLS	xxiii

CHAPTERS

1	INTRODUCTION	1
1.1	Motion Platforms	1
1.2	Typical Motion Control Architecture for Motion Platforms	1
1.3	Goal and Scope of The Study	11
2	LITERATURE SURVEY AND MODELING	13
2.1	A Summary of the Literature	13
2.2	The Setup Utilized for Experiments	39

2.3	Chapter Summary	40
3	SYSTEM IDENTIFICATION AND MODELING	41
3.1	Control of Brushless Electric Motors	41
3.1.1	Simplified Electro-mechanical Model	44
3.1.1.1	Analysis	46
3.1.2	Investigation of the Frequency Domain Behaviour .	47
3.1.3	Closed-Loop System Performance	50
3.1.4	Performance Obtained with a Real System	51
3.1.5	Section Summary - Contributions	56
3.2	Non-linear Effects in The Motion Transmission Part	57
3.2.1	BACKLASH	57
3.2.1.1	Backlash Modeling	58
	The Dead-Zone Model [40]:	58
3.2.1.2	Measuring Backlash Experimentally .	61
3.2.2	FRICTION	65
3.2.2.1	Coulomb Friction Model	66
3.2.2.2	Experimental Results on Friction . . .	67
3.3	Distributed Inertia Model for The Mechanical Components .	70
3.3.1	Analysis in s-domain	70
3.3.2	An Investigation of Frequency-domain Behavior for Second Mass Speed Output	72
3.3.3	Effects of System Parameters on Dynamic Behaviour	74

3.3.4	Controllability and Observability Analysis	76
3.3.5	Some Studies on the Experimental Setup	81
3.3.5.1	Transfer Function Identification	81
3.3.5.2	Discrepancies Between Experimental Results and Linear Behaviour	89
3.4	Reference Controller Designs	93
3.4.1	Proportional-Integral-Derivative with Filter (PIDF) Design	96
3.4.2	Sample Fuzzy Controller Design	98
3.4.3	The Method of Truxal and Guillemin (Direct Pole- Placement)	100
3.4.4	Section Summary	105
3.5	Chapter Summary	105
4	SELF-RECURRENT WAVELET NEURAL NETWORK BASED IN- DIRECT ADAPTIVE CONTROLLER WITH OPTIMIZED ADAP- TIVE LEARNING RATES AND STRUCTURE LEARNING	109
4.1	Wavelets and Wavelet Neural Networks	109
4.1.1	Indirect Adaptive Controller Employing SRWNNs	110
4.1.2	Modified Adaptive Learning Rates (MALR)	111
4.1.3	Control Architecture	116
4.2	Simulations	117
4.3	Experiments	120
4.4	Performance Comparison with Robust Control Designs on a Benchmark System	124

4.5	Automatic Determination of the Network Complexity - Self Evolution	131
4.6	Contributions	134
5	CONCLUSION	135
	REFERENCES	137
	APPENDICES	
A	GENETIC ALGORITHMS USED TO FIT TRANSFER FUNCTION TO FRF DATA	145
	CURRICULUM VITAE	149

LIST OF TABLES

TABLES

Table 1.1	Components of a Typical Motion Platform's Speed Control System . . .	6
Table 3.1	Parameters of the System Model Given in Fig. 3.3 and Sample Values Used During Simulations	45
Table 3.2	Parameter Definitions for the Backlash Model Schematic of Fig. 3.14	60
Table 3.3	Experimentally obtained backlash angles for the system under study (motor side).	66
Table 3.4	Experimentally obtained static friction values.	70
Table 3.5	Parameters of the model given in Fig. 3.19	71
Table 3.6	Properties of the assumed transfer function employed during the genetic algorithm process.	85
Table 3.7	Zeros and Poles of the Transfer Function $G(s)$ Evaluated Using Genetic Algorithm Method.	87
Table 3.8	PIDF Controller Parameters and Performance Measures.	98
Table 4.1	Performance Comparison on Benchmark System Control	128
Table A.1	Parameters of the Genetic Algorithm Used for Transfer Function Fitting to FRF.	147
Table A.2	Basic Performance Figures of the Employed Genetic Algorithm. . .	147

LIST OF FIGURES

FIGURES

Figure 1.1 A typical example of a motion platform: Leopard-2A4 [®] Main Battle Tank from Krauss Maffei Wegman. In this system optics and gun motion control are performed independently.(Photo Courtesy of KMW Inc.)	2
Figure 1.2 Another example of a motion platform: Pedestal Mount Stinger Launching System - PMS ATILGAN [®] .(In this system the payload is eight land-to-air missiles and optics to detect and track possible threats.(Photo Courtesy of Aselsan Inc.)	2
Figure 1.3 Another example of a motion platform: Stabilized Machine Gun Platform - STAMP [®] .In this system the payload is a machine gun and optics to detect and track possible threats. (Photo Courtesy of Aselsan Inc.)	3
Figure 1.4 In the KORKUT air defense system developed by Aselsan Inc. there are independent motion platforms on the same system (one for optics / RADARs and other for the gun) (Photo Courtesy of Aselsan Inc.)	3
Figure 1.5 General structure of a director type gun control system - Case of a Main Battle Tank (MBT) [35]	4
Figure 1.6 Schematics showing the components and their interfaces of a typical (electrically actuated) motion platform’s speed control loop - Case of A Main Battle Tank (MBT)	10
Figure 2.1 System model schematic used by [8] with linear model’s original, dominant and closed-loop poles.	14
Figure 2.2 Step position responses for gun position control: LQG/LTR simulation (left), H^∞ simulation (right) [15] under firing disturbance.	15
Figure 2.3 Experimental result with variable structure control (VSC) given in[16].(Note the chattering in gun speed)	16
Figure 2.4 Torque sensor drawing and mechanical model employed in [11].	17

Figure 2.5 Control architecture with FLC compensation (left) and improvement of control performance after utilization of the FLC (right, with solid lines) as given in [20].	18
Figure 2.6 (Simulink models used for system dynamics (left) and H^∞ controller (right) in [29].	20
Figure 2.7 2 mass system model (left) and Resonance-Ration Control (RRC) as employed in [27]. Here K_r term is to be adjusted to achieve desired inertia ratio of the two masses, corresponding to the resonance frequency .	20
Figure 2.8 Schematic of the system under consideration in [34]. Such systems are usually equivalent to motion platforms subject to our study.	21
Figure 2.9 3 mass system schematic (left) and Frequency Response Function (FRF) (right) for the test system used in [30].	21
Figure 2.10 Control architecture for the speed control of a 3 mass system, as used in [30].	22
Figure 2.11 Surface Acoustic Wave (SAW) shaft torque transducers (left) and measurement infrastructure used by O’Sullivan and colleagues [66].	22
Figure 2.12 Schematic of the quick return mechanism (left) and proposed control architecture (right) in [50].	23
Figure 2.13 FRFs of the open-loop system (left) and closed-loop system (right) showing speed control performances achieved with PI control cascaded with different type of resonance suppression methods in [49].	24
Figure 2.14 Step response of the first mass speed with different type of resonance suppression methods used in conjunction with PI control ([48]). Although bi-quad filtering seems to give the best result for the single experiment, its robustness is unacceptably poor.	25
Figure 2.15 The state feedbacks grouped considering their effects on closed-loop pole locations for a two mass system [67]. Here m terms stand for torques; T terms stand for time constants (stiffness and inertias) and ω terms stand for angular speed	26
Figure 2.16 Block diagram representation of the three-mass mechanical system with simplified dynamics ignoring viscous damping terms.	27
Figure 2.17 General control architecture used in [68], in which Model-Reference Adaptive Control is combined with Neuro-Fuzzy Controller.	27

Figure 2.18 Internal structure of the "Speed Controller Fuzzy Neural Network" given in Fig. 2.17.	28
Figure 2.19 Speed output, speed error, motor torque and weight update plots from a sample speed controller operation obtained in [68].	29
Figure 2.20 A time-domain comparison plot from our simulations with the same neuro-fuzzy controller in [68] used for a three-mass system; showing the poor convergence performance with under-damped step response at steady state.	30
Figure 2.21 Typical weight updates from a simulation conducted by us, employing the neuro-fuzzy MRAC architecture proposed in [68]. This graph shows that the convergence of the architecture proposed by the authors is not guaranteed.	31
Figure 2.22 The sliding surface implemented in the adaptive neuro-fuzzy structure and a sample phase portrait as given in[74].	31
Figure 2.23 The non-linear adaptive control architecture proposed in [73].	32
Figure 2.24 Simple architecture proposed with model-predictive control (top) and motor torque mapping from first and third mass speeds for the model predictive control design performed (top) in [79] and [81].	33
Figure 2.25 General adaptive control scheme (a), and Model-Reference Adaptive Control (MRAC) scheme (b).	35
Figure 2.26 Test setup on which experiments have been conducted.	39
Figure 3.1 Structure of a typical brushless motor (left) and its cross-sectional schematic (right). Rotating magnetic field created by appropriate excitation of the field windings (electronic commutation) is necessary for successful operation of such a motor.	42
Figure 3.2 Typical field orientation architecture for the current control of a PMSM.	43
Figure 3.3 Schematic representing the system model used for analysis.	44
Figure 3.4 Frequency response function plot of the SISO system models given in equations (3.13) and (3.14).	48
Figure 3.5 Open- (left) Closed-loop (right) frequency response function plot of the SISO system models given in equations (3.13) and (3.14) obtained with PI control with parameters $K_P = 1$ and $K_I = 1000$	48

Figure 3.6 Experimentally Obtained Open Loop System FRF for MO case. . .	53
Figure 3.7 Experimentally Obtained Open Loop System FRF for MCL case. . .	54
Figure 3.8 Experimentally Obtained Closed Loop System FRF for MO case. . .	54
Figure 3.9 Experimentally Obtained Closed Loop System FRF for MCL case. . .	55
Figure 3.10 Phase difference between theoretical and experimental MO FRF findings.(Note the linear trend indicating transport delay).	55
Figure 3.11 Backlash phenomenon between two paired gears schematized. . . .	57
Figure 3.12 Utilization of anti-backlash pinion to avoid backlash. Note that, the drawing is two-dimensional and there are two different gears on top of each other on the right-hand side gear; pre-loaded with small springs. [87]	58
Figure 3.13 A typical example of a pre-loaded anti-backlash gear assembly with idler gears schematic (left), and an example of a direct pre-load mechanism (right - inside the red ellipse). [87]	59
Figure 3.14 Schematic showing the backlash phenomenon in a two-mass system, where torque from a motor is transferred to a load via a shaft with a backlash angle of α . (refer to Table 3.2 for the list of parameters given in the figure)	59
Figure 3.15 Non-linear dead-zone function used for modeling the backlash behavior.	61
Figure 3.16 Figure illustrating the identification of backlash via indirect dynamic identification approach.	62
Figure 3.17 Sample backlash measurement experiment with the system under study. (a) Overall experiment data; (b) A typical motor position jump inside the backlash region, during a torque pulse; (c) Change in the behavior of the system at the end of backlash region.	64
Figure 3.18 The experimentally measured static friction. Positive direction friction data (red), its average (blue). Negative direction friction data (green), its average (black). The high speed friction plots are given as a reference for modeling error by ignoring viscous behavior.	69
Figure 3.19 Schematic representation of the linear three-mass mechanical system model.	70
Figure 3.20 Typical Frequency Response Function (FRF) plot for the second mass speed output of a 3 mass system.	73

Figure 3.21 Simplified system model with all damping terms neglected.	74
Figure 3.22 Torque input to second mass speed output FRF change w.r.t. first mass inertia, J_m	76
Figure 3.23 Torque input to second mass speed output FRF change w.r.t. second mass inertia, J_g	77
Figure 3.24 Torque input to second mass speed output FRF change w.r.t. third mass inertia, J_l	77
Figure 3.25 Torque input to second mass speed output FRF change w.r.t. first shaft stiffness, k_{s1}	78
Figure 3.26 Torque input to second mass speed output FRF change w.r.t. second shaft stiffness, k_{s2}	78
Figure 3.27 Plot of time domain data for torque, angular speed and current frequency for the frequency sweep experiment.	83
Figure 3.28 Magnitude of the Frequency Response Function of the system obtained using the measured sine-sweep data.	84
Figure 3.29 Magnitude and Phase of the Frequency Response Function of the system obtained using the measured sine-sweep data (blue) and $G(s)$ evaluated using the genetic algorithm search method (red).	86
Figure 3.30 Experimentally obtained and transfer function fitted frequency response function plots with a delay of $17ms$ and phase offset of 22°	88
Figure 3.31 Frequency response of the plant for different motor current (torque) input amplitudes.	90
Figure 3.32 Gyro noise for the stationary system, whose level is in the order of 0.002 deg/s peak-peak.	92
Figure 3.33 Time domain data from frequency sweep tests, at the frequency $0.75Hz$	93
Figure 3.34 Time domain data from frequency sweep tests, at the frequency $2Hz$	94
Figure 3.35 Time domain data from frequency sweep tests, at the frequency $5Hz$	94
Figure 3.36 Time domain data from frequency sweep tests, at the frequency $7Hz$	95
Figure 3.37 Time domain data from frequency sweep tests, at the frequency $18Hz$	95

Figure 3.38 Time domain data from frequency sweep tests, at the frequency $38Hz$	96
Figure 3.39 Simulink Model used to perform simulations for the response of $G(s)$ with a simple PIDF controller.	97
Figure 3.40 Step response of the closed loop system employing a PIDF controller.	97
Figure 3.41 Membership functions of the 7 fuzzy sets used for both input and output variables.	98
Figure 3.42 Fuzzy Logic Controller I/O mapping with the membership functions given in Fig. 3.41 and a 49-rule rule base.	99
Figure 3.43 Simulink Implementation of the closed loop system with fuzzy logic controller.	99
Figure 3.44 Step response of the closed-loop system given in Fig. 3.43.	100
Figure 3.45 Typical closed loop control structure.	101
Figure 3.46 Structure of the controller in Truxal and Guillemin design.	102
Figure 3.47 Open-loop FRF with Truxal-Guillemin design simulation of three mass linear system.	103
Figure 3.48 Closed-loop FRF with Truxal-Guillemin design simulation of three mass linear system.	104
Figure 3.49 Controller output during a sine-sweep velocity reference with Truxal-Guillemin design simulation of three mass linear system.	104
Figure 4.1 Plot of the Gaussian derivative wavelet.	110
Figure 4.2 Recurrent Neural Network in State-Space Model form. ([58])	110
Figure 4.3 SRWNN internal structure proposed in [60]	112
Figure 4.4 SRWNN based iterative adaptive controller (SRWNN IAC) structure similar to the one in [69].	116
Figure 4.5 Step Response with the original ALR algorithm (Top two plots) and the Modified ALR algorithm (bottom two plots).	118
Figure 4.6 Step Response when stiffness values are reduced by 50%. The Truxal-Guillemin design(Top two plots) and SRWNN IAC (bottom two plots).	119

Figure 4.7 Experimental result showing the convergence performance of the SRWNN identifier with ALR.	121
Figure 4.8 Experimental result showing the convergence performance of the SRWNN identifier with MALR.	122
Figure 4.9 Experimental results for the comparison of proposed SRWNN IAC and high performance PI controller.	123
Figure 4.10 The schematic and block diagrams showing the structure of the benchmark three mass system ([33])	125
Figure 4.11 Frequency Response Functions of the benchmark system in [33].	127
Figure 4.12 Performance of the SRWNN identifier for the un-loaded benchmark system in [33]. Initial (top 3 plots) and steady-state (bottom 3 plots)	129
Figure 4.13 Step Response for the un-loaded benchmark system utilising SRWNN-MALR IAC. Initial (top 2 plots) and steady-state (bottom 2 plots).	130
Figure 4.14 A Simulation showing the result of the evolutionary algorithm for the identifier during un-loaded benchmark system identification simulations.	133

LIST OF ABBREVIATIONS

AC	Alternating Current
ACC	American Control Conference
ALR	Adaptive Learning Rates
ANN	Artificial Neural Network
DC	Direct Current
DSP	Digital Signal Processor
EKF	Extended Kalman Filter
FLC	Fuzzy Logic Control
FNN	Fuzzy Neural Network
FRF	Frequency Response Function
IAC	Indirect Adaptive Control
IGBT	Insulated Gate Bipolar Transistor
LPF	Low-Pass Filter
LQG	Linear Quadratic Gaussian
LQR	Linear Quadratic Regulator
LTR	Loop Transfer Recovery
MALR	Modified Adaptive Learning Rates
MBT	Main Battle Tank
MIMO	Multi-Input Multi-Output
MMF	Magneto-Motive Force
MCL	Motor Coupled to Load
MIMO	Multi-Input Multi-Output
MO	Motor Only
MOSFET	Metal-Oxide Semiconductor Field Effect Transistor
MPC	Model-Predictive Control
MRAC	Model-Reference Adaptive Control
MTBF	Mean-Time Between Failures
NF	Neuro-Fuzzy

PC	Personal Computer
PI	Proportional-Integral
PID	Proportional-Integral-Derivative
PIDF	Proportional-Integral-Derivative with Filter
PWM	Pulse Width Modulation
RRC	Resonance-Ratio Control
RTWT	Real-Time Windows Target
PMSM	Permanent Magnet Synchronous Motor
RRC	Resonance Ratio Control
RST	Actually this is not an abbreviation, R, S and T represent different polynomials used inside the control loop in this very popular control technique
SAW	Surface Acoustic Wave
SIDF	Sinusoidal-Input Describing Function
SISO	Single-Input Single-Output
SMC	Sliding-Mode Control
SRWNN	Self-Recurrent Wavelet Neural Network
VSC	Variable Structure Control
WNN	Wavelet Neural Network

LIST OF SYMBOLS

ELECTRICAL MOTORS

t_e	Electrical Torque
L_m	Equivalent Magnetizing Inductance
L_r	Equivalent Rotor Inductance
i_{qds}^e	Equivalent Stator Current Vector in Electrical Frame
λ_{qdr}^e	Equivalent Magnetic Flux Vector Created by Rotor Magnets in Electrical Frame.
k_t	Torque Constant
I_{eq}	Armature Current
V_{in}	Terminal voltage of the equivalent permanent magnet DC motor.(applied by the motor driver)
I_m	Armature current developed in the equivalent DC motor armature circuit
R_a	Armature resistance of the equivalent permanent magnet DC motor
L_a	Armature inductance of the equivalent permanent magnet DC motor
E_a	Back-emf voltage of the equivalent permanent magnet DC motor
T_m	Mechanical torque developed on motor shaft
θ_m	Motor shaft position reflected to the load side
J_m	Equivalent load-side inertia of the motor shaft and gear box
θ_g	Gearbox output angular position
T_g	Torque at the gearbox output
θ_l	Angular position of the Load
c_s	Equivalent damping coefficient for connections between motor and the load
k_s	Equivalent stiffness coefficient for connections between the motor and the load
J_l	Equivalent load inertia
k_e	Back-emf constant of the equivalent DC motor
k_t	Torque constant of the equivalent DC motor
n_g	Gear ratio of the gearbox

f_1	Lower resonance frequency of the open-loop (V->I) transfer function of the electro-mechanical model in MCL case
f_1	Anti-resonance frequency of the open-loop (V->I) transfer function of the electro-mechanical model in MCL case
f_3	Higher resonance frequency of the open-loop (V->I) transfer function of the electro-mechanical model in MCL case

SELF-RECURRENT WAVELET NEURAL NETWORKS

w_{ji}	Weight parameter of the neuron coded ij
η	Learning rate of the gradient descent algorithm
ξ	Cost function
Δ	Change operator
∂	Difference operator (partial case)
α	Momentum factor used during weight updates
$\psi(u)$	A wavelet function
$\Psi(f)$	Fourier transform of $\psi(u)$
λ	Dilation of a wavelet
t	Translation of a wavelet
x_k	k^{th} element of the input vector of SRWNN
m_{jk}	translation of the wavelon jk
d_{jk}	dilation of the wavelon jk
θ_{jk}	Feedback gain of the wavelon jk
$\Phi_j(x)$	j^{th} wavelon group activation
w_j	Weight of the j^{th} wavelon group
a_k	Weight of the k^{th} input vector element
\vec{W}	Weight (row) vector of an SRWNN
\vec{a}	(row) vector of input gains of an SRWNN
\vec{m}	(row) vector of translations of an SRWNN
\vec{d}	(row) vector of dilations of an SRWNN
$\vec{\theta}$	(row) vector of feedback gains of an SRWNN
\vec{w}	(row) vector of output layer gains of an SRWNN
J	Cost function defined for SRWNN
$\bar{\eta}$	Diagonal matrix of learning rates of SRWNN
$\vec{\nabla}_{W} J$	Gradient of the cost function J with respect to the weights vector \vec{W} .

BACKLASH & FRICTION

$\theta_1(t)$	Angle of the motor
---------------	--------------------

$\theta_2(t)$	Angle of the load
$\theta_3(t)$	Angle of the driving axis at the backlash
$\theta_d(t) = \theta_1(t) - \theta_2(t)$	Displacement
$\theta_s(t) = \theta_1(t) - \theta_3(t)$	Shaft twist
$\theta_b(t) = \theta_3(t) - \theta_2(t)$	Backlash angle
J_m	Motor inertia
ω_m	Motor speed
k_s	Shaft stiffness coefficient
c_s	Shaft damping coefficient
J_l	Load inertia
ω_l	Load speed
T_d	Load disturbance torque input
T_m	Motor torque input
T_s	Shaft torque developed
$D_\alpha(\cdot)$	Dead-zone function
T_a	Applied torque
T_s	Pre-specified constant friction torque
T_f	Friction torque
α	Angular acceleration

CHAPTER 1

INTRODUCTION

1.1 Motion Platforms

Motion platforms with payloads are widely used in modern defense systems. While the payloads may vary according to application (see Fig.1.1, Fig. 1.2, Fig. 1.3, Fig. 1.4 for some examples), the models, and hence techniques used for motion control are usually the same. In most of the motion platforms actuation is achieved by driving brushless electric motors via power electronic components (widely Metal-Oxide Semiconductor Field Effect Transistors (MOSFETs) or Insulated Gate Bipolar Transistors (IGBTs) and their driver circuits). These components are controlled by processors which are capable of performing real-time calculations which use sensory information from gyroscopes, encoders, resolvers, inclinometers, force/torque sensors etc. The aim of control during these calculations is generating "the correct motor current" which will move the platform with desired speed with respect to Earth reference frame, which will in turn carry the platform to a desired position. Hence, the calculations try to suppress the disturbances (hull motion, windage , sea waves etc.) while trying to obtain a closed loop transfer function from reference command to load speed equal to or at least very close to unity.

1.2 Typical Motion Control Architecture for Motion Platforms

A typical motion control architecture for a Main Battle Tank's (MBT) gun is given in Fig. 1.5. All the motion platforms have more or less the same structure for motion



Figure 1.1: A typical example of a motion platform: Leopard-2A4[®] Main Battle Tank from Krauss Maffei Wegman. In this system optics and gun motion control are performed independently.(Photo Courtesy of KMW Inc.)



Figure 1.2: Another example of a motion platform: Pedestal Mount Stinger Launching System - PMS ATILGAN[®].(In this system the payload is eight land-to-air missiles and optics to detect and track possible threats.(Photo Courtesy of Aselsan Inc.)



Figure 1.3: Another example of a motion platform: Stabilized Machine Gun Platform - STAMP[®]. In this system the payload is a machine gun and optics to detect and track possible threats. (Photo Courtesy of Aselsan Inc.)



Figure 1.4: In the KORKUT air defense system developed by Aselsan Inc. there are independent motion platforms on the same system (one for optics / RADARs and other for the gun) (Photo Courtesy of Aselsan Inc.)

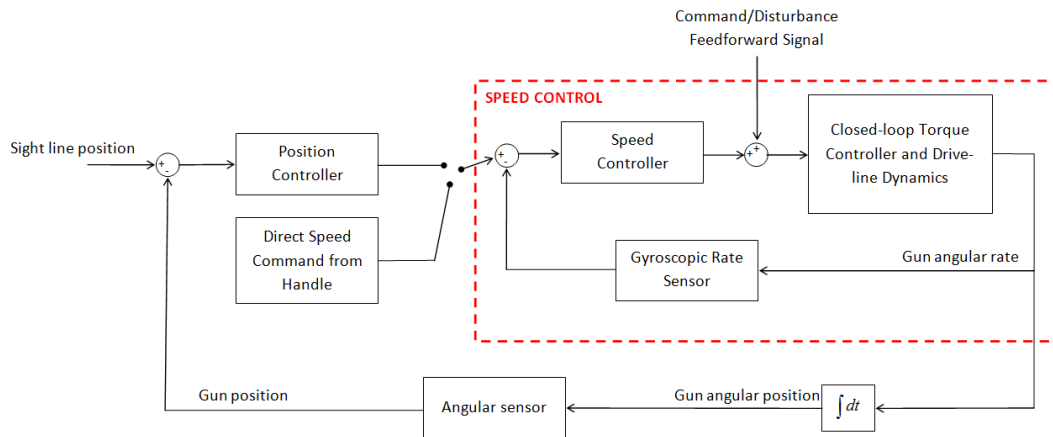


Figure 1.5: General structure of a director type gun control system - Case of a Main Battle Tank (MBT) [35]

control: A reference speed command either originating from sighting (target tracking) system's position error command or from directly user input (usually in the form of a command handle signal). Performing the "speed control" with high performance is one of the most critical problems in successful operation of these systems. In this study, we will be mainly dealing with this problem, i.e. "speed control".

As given in the block diagram of Fig. 1.6, for a typical motion platform speed control "the plant" consists of mainly three parts: The motion generation part, the motion transmission part, and the load (gun and turret for the MBT example of Fig. 1.6).

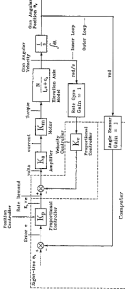
In the past, hydraulic actuation was usually employed as the motion generation part, whereas in today's technology permanent magnet synchronous motors (PMSM) and a Digital Signal Processor (DSP) based motor controller, in order to generate the motor controlling signals, are usually used. The dynamics of PMSMs are inherently non-linear and several techniques are developed to perform seamless torque control of these motors under various operating conditions. These techniques usually rely on field-orientation and vector control. The required voltages for the motor commutation are generated using special Pulse Width Modulation (PWM) patterns, which injects further high-frequency components and torque ripples to the motor response.

The motion transmission part consists of gearboxes for matching the load's speed and torque requirements, and mechanisms to shape the motion in a desired fashion. This part introduces backlash, friction, stiffness and inertial effects, usually hindering the

control design. Backlash and friction are frequently modelled on the contact points as non-linear connection elements. Stiffness and inertia are modelled as bodies connected with flexible joints. If we continue our example with the MBT case: The turret is usually driven via a gear stage connected to the output shaft of the motor. The output of this gear stage is connected to a ring gear which is fixed to the hull and the turret is connected to the hull with a ring bearing which is free to rotate about its center. The gun is driven by either using rack-pinion mechanisms or a lead-screw drive, mimicking the behavior of the hydraulic pistons.

The load is the mechanical component whose speed is to be controlled. It usually corresponds to parts with distributed inertia connected with finite stiffness. Both the inertia and stiffness of these parts effect the control design. Moreover, the inertia, friction and unbalance of the load are key factors in sizing the components of the speed control system, some of which are given in Table 1.1. For the MBT example, load consists of the turret in traverse axis and the gun in elevation axis.

Table 1.1: Components of a Typical Motion Platform's Speed Control System

Component	Duty	Example
Controller and Driver	Running the motion control algorithms and controlling the electric motors	
Electric Motors	Converting the electrical energy provided by the controller to the mechanical energy utilized by the payload	
Gearboxes and Transmission Equipment	Converting electric motor output into suitable torque & speed for the load	
Sensors	Supplying state information to the motion control algorithms. Usually gyroscopes, encoders and resolvers are employed in motion platforms.	
Motion Control Algorithms	Generating torque commands for the motors by utilizing the motion command and the sensor readings. These algorithms are usually run on the controller in real-time	

It is also worth mentioning that -despite the three parts mentioned in above paragraphs- in modelling motion platforms for speed control purpose, the system is usually divided into two parts as "electrical" and "mechanical" subsystems. The electrical subsystem does usually have a wider bandwidth and under certain conditions it can simply be modelled as unity or as a simple first-order low-pass filter [85]. The mechanical part of the motion platform is usually modelled as a multi-body system with elastic connections in between. Mechanical models with three inertias are usually preferred for the purpose of control, while models with two inertias are also common.

As for the control technique used for speed control, we can very roughly divide the approaches into two branches, as usual: linear control and non-linear control.

Linear control theory is a mature subject and it has a serious number of methods that can be used for analysis and design including Nyquist, Bode, Root-Locus techniques. Moreover, it has a long history of successful applications in engineering world, especially in the form of proportional-integral-derivative (PID) controller and its variations. However, it cannot deal with model uncertainties, serious non-linear effects and operational constraints that must be imposed to the system such as actuator limitations. Nevertheless, PID control has been very frequently employed for speed control of motion platforms. This is just because of the fact that, for some of the applications, performance of PID controllers might be sufficient. For some others, even if it is not sufficient, additional precautions have been taken in order to compensate for the non-linear effects hindering PID controller's performance. The certain disadvantage of this design approach is long engineering hours wasted for identification and compensation of non-linear effects. Moreover, automatic tuning of PID controllers under several non-linearities is not a straightforward task to perform. In any case, a vast number of studies from the literature rely on PID control and/or its variations.

Due to severe non-linear effects hindering linear controllers' performance, several techniques from non-linear control have also been employed for speed control of motion platforms. Techniques ranging from H_∞ , sliding-mode control (SMC), model-predictive control (MPC), model-reference adaptive control (MRAC) to several forms of neural-networks, genetic algorithms and their variations have been used. The most

basic drawback of non-linear control is the fact that analysis and design of a non-linear controller are not as straightforward as those of a linear controller. Tools and techniques are usually limited and successful application in practical systems (for the case of speed control of motion platforms) is rare as compared to linear control. On the other hand, if practical difficulties can be overcome; it is obvious that non-linear control would be more effective than the linear control for the speed control of motion platforms.

Before giving a more detailed review of the current literature on the topic, it is worth introducing the basic terms and difficulties for the speed control of motion platforms. Since there is a vast variety of motion platforms with similar properties and control design goals, we will perform the introduction considering the MBT gun-turret speed control example of Fig. 1.6, without loss of generality.

A key feature of an MBT is its ability to engage targets while moving on rough terrain. Meanwhile, varying operational conditions pose significant challenges in maintaining a high level of accuracy which is an essential requirement for the operation of MBTs. An efficient control strategy must be employed to ensure precision pointing of the weapon according to the gunner's sighting system (see Fig. 1.5), and speed control is certainly the most crucial and challenging part of the control loop. Besides, it is essential that the control system implemented maintains its performance in the presence of large disturbances induced due to the movement of the vehicle along the rough terrain [75]. During operation of the gun-turret system, it is also critical that the gun maneuvered to avoid any obstacles existing on the vehicle's own platform (examples include antennas, open hatches and the vehicle chassis itself). This introduces several constraints for actuator limitations. Moreover, the gun speed control is subject to non-linearities such as backlash, Coulomb friction, and actuator saturation; unmodelled dynamics such as gun barrel flexible modes; parameter variations such as changes of load, torsional stiffness, and disc friction; and external disturbances such as base motion and firing effects. Accordingly, the design must be robust, adaptive, and -hopefully- intelligent in order to accommodate these uncertainties. In summary, the design objectives of speed control of a MBT gun include

- Rapid and precise pointing (command tracking) capability requiring a very stiff

speed control,

- Robustness against un-modeled flexible modes of the mechanical system,
- Disturbance rejection against base motion and (possible) firing,
- Accommodation of parameter variations and inherent non-linear effects,
- Integration with target tracking and gunner models when necessary.

To summarize, all reasons usually cited to justify the need for robust and adaptive control are to be found in "the speed control of a motion platform" problem:

- Moments of inertia, unbalance and friction disturbance torques change rapidly with the platform position.
- Friction and other non-linearities change over time because of uneven maintenance, and differ greatly between samples of the same system model because of production tolerances.
- There are uncertain disturbance due to platform movement over rough terrain.

Keeping these facts in mind, control engineers have developed several methods in order to deal with the speed control of a motion platform problem, a brief summary of these methods is the subject of the following section.

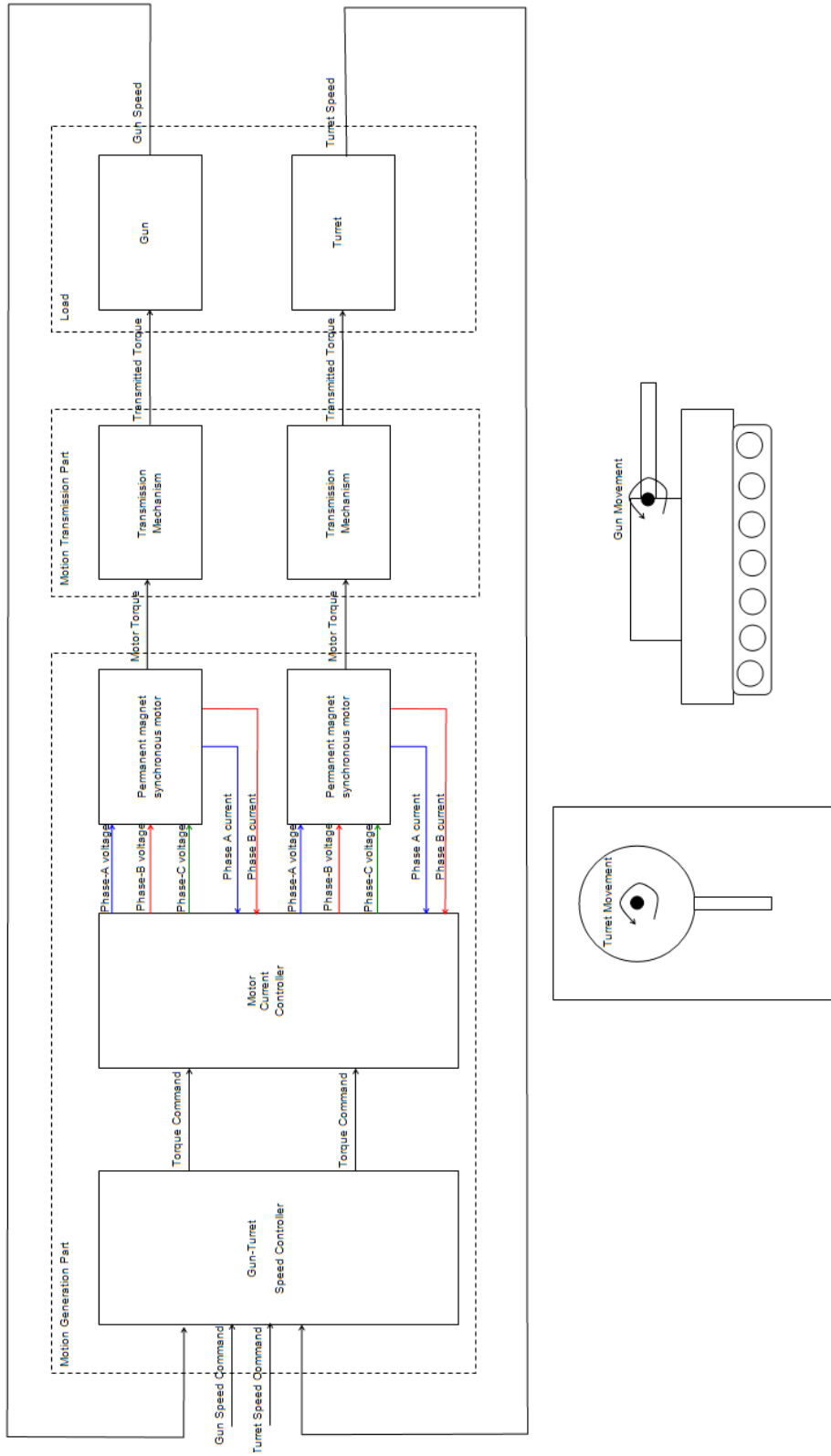


Figure 1.6: Schematics showing the components and their interfaces of a typical (electrically actuated) motion platform's speed control loop
 - Case of A Main Battle Tank (MBT)

1.3 Goal and Scope of The Study

Control system design for the speed control of motion platforms is a challenging task. In this study, the aim is to decrease the amount of design effort needed by utilizing modern techniques from the literature, and develop a novel method in order to achieve this. For this purpose literature survey was performed, system modeling and identification studies were conducted, and at the end a novel architecture by adding additional improvements to a state-of-the art Self-Recurrent Wavelet Neural Network based Indirect Adaptive Controller was proposed. The effectiveness of the proposed improvements was proven by analysis, simulations and experiments.

The next chapter is dedicated to the literature survey and description of the experimental setup employed during the study. Chapter 3 is reserved for the experimental and theoretical efforts on modeling and identification of the system under study. Moreover, in the same chapter, some controller designs for the system under study has been performed to address their performance as a reference. Chapter 4 is dedicated to the proposed control architecture and analysis of the improvement gained by this architecture by theory, simulations and experiments. The manuscript is finalized with the conclusions given in Chapter 5. There is one appendix for explaining the genetic algorithm method employed during the system identification procedure.

CHAPTER 2

LITERATURE SURVEY AND MODELING

2.1 A Summary of the Literature

The literature regarding the speed control of servo systems is very broad. On the other hand, due to confidentiality, most of the studies conducted for military motion platforms were either not published, or published without giving candid details regarding the real system under consideration. Hence, it is not possible to access all the relevant literature. In this section, a brief summary of the accessible literature is provided in a chronological order.

As stated in the previous sections, linear control techniques are widely used for motion platform speed control. In [3], "the gunner" is modelled as a variable gain element and authors propose a digital filter to be added to the command path taking the gunner's current "gain" into account. By this way decoupling between sight and gun controls is achieved, making the "driven-reticle" (sight following gun) and "gun director" (gun following sight) configurations realized with minimum loss of performance during "low gain" of the gunner. In [4], same authors give their experimental findings and report an improvement of 50% in gunner tracking error, weapon pointing accuracy and opportunity to fire.

In [8] authors apply Linear Quadratic Gaussian with Loop Transfer Recovery (LQG / LTR) method for the robust control of a helicopter gun-turret. They employ a 12th order linearized model from motor current to gun position and reduce it to 7th order for control design (see Fig. 2.1). They only provide simulation results where system matrix entries are perturbed by 5%, driving a standard controller to sustained oscilla-

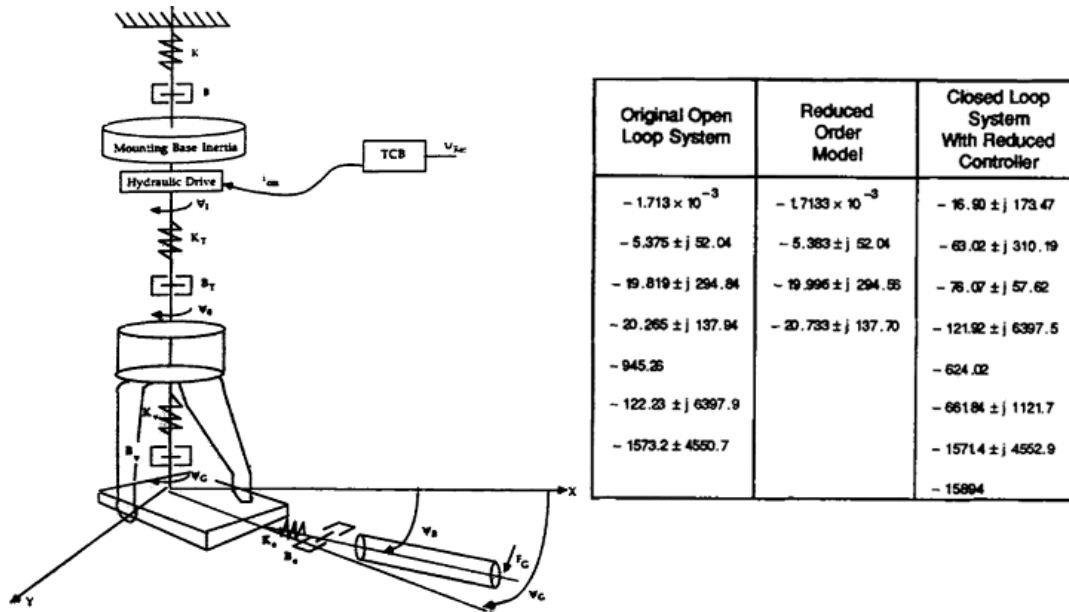


Figure 2.1: System model schematic used by [8] with linear model's original, dominant and closed-loop poles.

tions, while the oscillations are suppressed with their robust controller. For this case, we may state that the system is not adaptive, but only robust, i.e., the performance is reduced to achieve robustness.

In [10], the same helicopter gun system is modeled using non-linear effects as well. LQG/LTR approach is employed with a 40th order model. In addition to mechanical enhancements to reduce firing effects on control performance; a digital filter is also added to suppress firing shocks. Moreover, a feed-forward compensator is also added to the control loop in order to suppress the effects of residual offset during firing. Authors report that the system goes unstable after only a parameter variation of 50%.

In [15] authors reviewed different control schemes and methodologies used for gun-turret pointing control. During their study robust control (including LQG / LTR and H_∞), non-linear control and intelligent control (fuzzy combined with H_∞) are evaluated in simulation. Their claimed result is that fuzzy and H_∞ control together gives the best step response for tracking control under firing disturbance (see Fig. 2.2).

In [16] authors applied variable structure control (VSC) for a tank gun. They base the design on a 2nd order LTI system model. They claim that the designed system shows

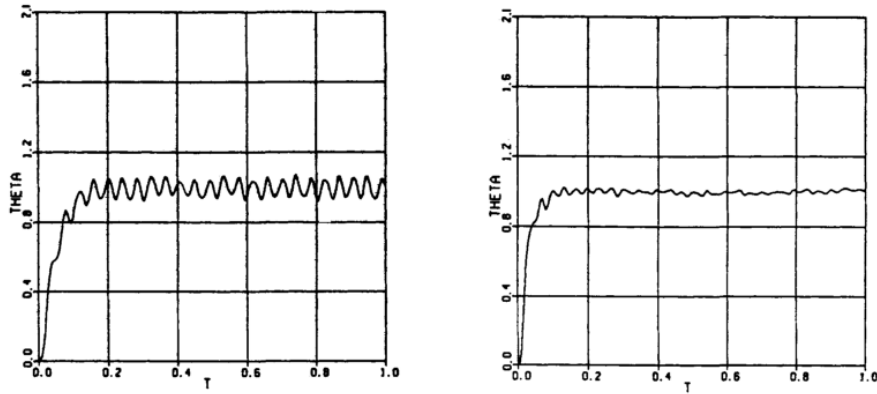


Figure 2.2: Step position responses for gun position control: LQG/LTR simulation (left), H^∞ simulation (right) [15] under firing disturbance.

perfect robustness. Moreover, they insist on that the simulation results obtained with a nonlinear model (not given in the study) is well-fitted with the test data collected on a real tank, the only disadvantage being the fact that the sliding mode caused chattering which resulted in power drain. However, as seen in Fig. 2.3, the chattering in the speed of the platform is unarguably not acceptable in practice.

In [13] authors followed the robotic formulation to derive system dynamical equations for both tank and helicopter turret-gun systems (including axis couplings, Coriolis terms etc.). They then propose a standard PD control for direct position control and provide simulation results on gun positioning. The main focus of the study is the robotic formulation of the modeling phase and control performance is not stressed.

In [11] torque sensors are situated on the harmonic drive gear-trains to feed the joint torques back for the use of controller (See Fig. 2.4). Utilization of the torque feedback is shown to be effective in suppressing the vibration due to joint flexibility and also Coulomb friction effects. Although this approach seems useful, it will decrease the mean-time between failures (MTBF) of the system and increase costs due to additional hardware requirements.

In [19] authors incorporate linearized models of backlash and friction in designing a non-linear controller. They use a 10^{th} order non-linear model and incorporate non-linear servo-mechanism controller as a remedy to non-linearities. In [21], same authors propose a fuzzy logic control (FLC) on top of alternative control designs (H^2 , H^∞ and non-linear servo), in order to inform the controller on the temporal

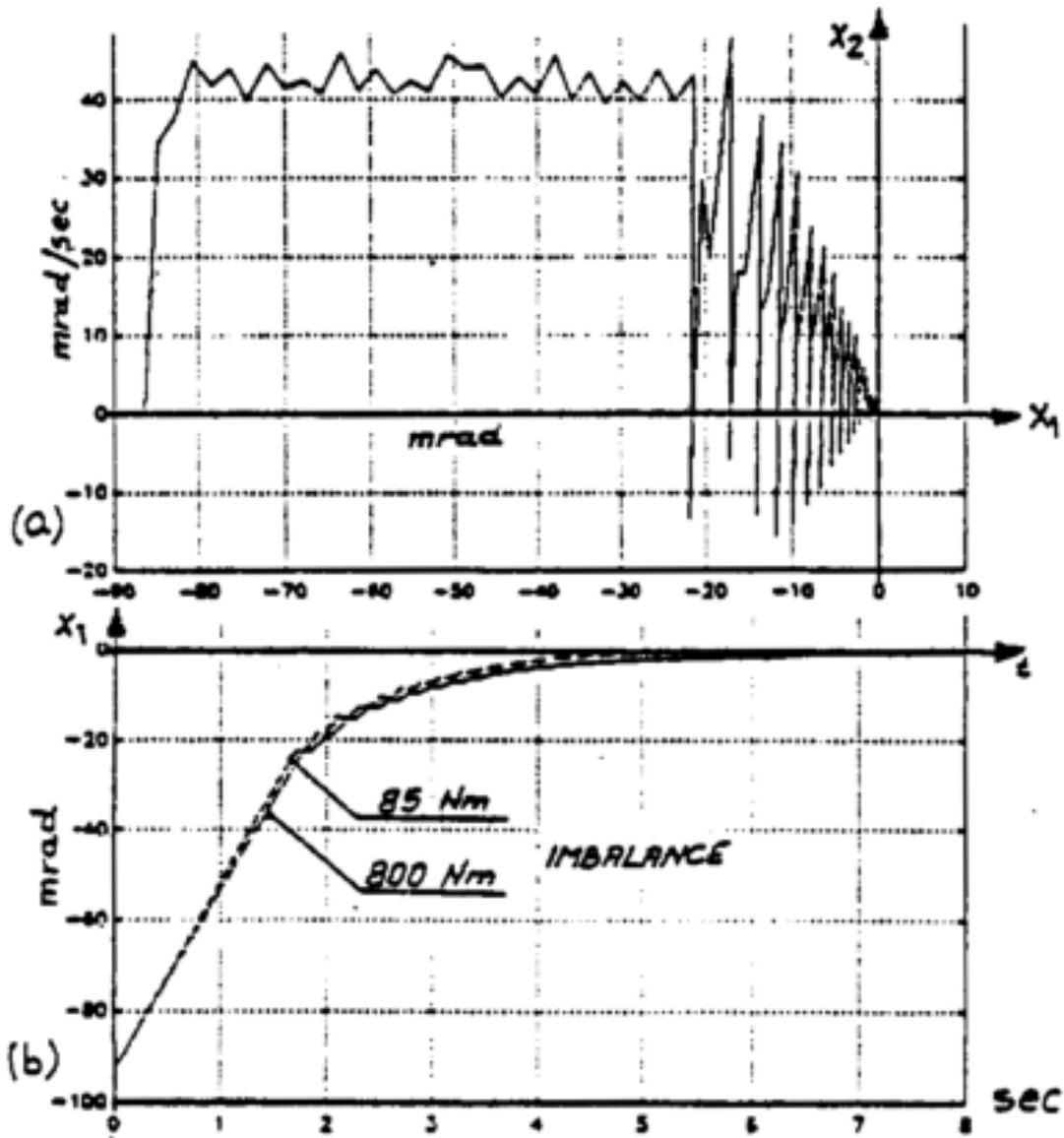


Figure 2.3: Experimental result with variable structure control (VSC) given in[16].(Note the chattering in gun speed)

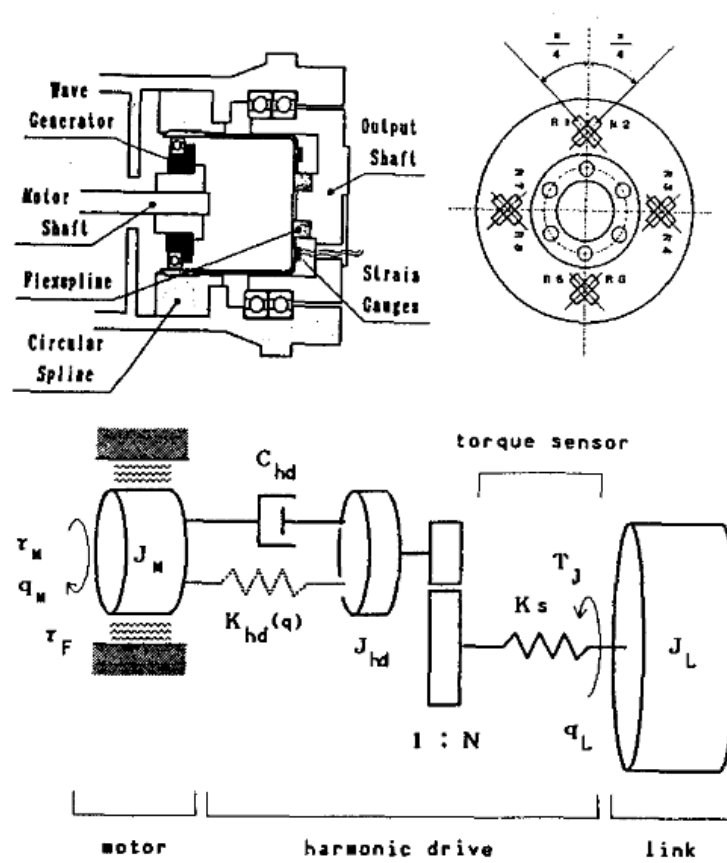


Figure 2.4: Torque sensor drawing and mechanical model employed in [11].

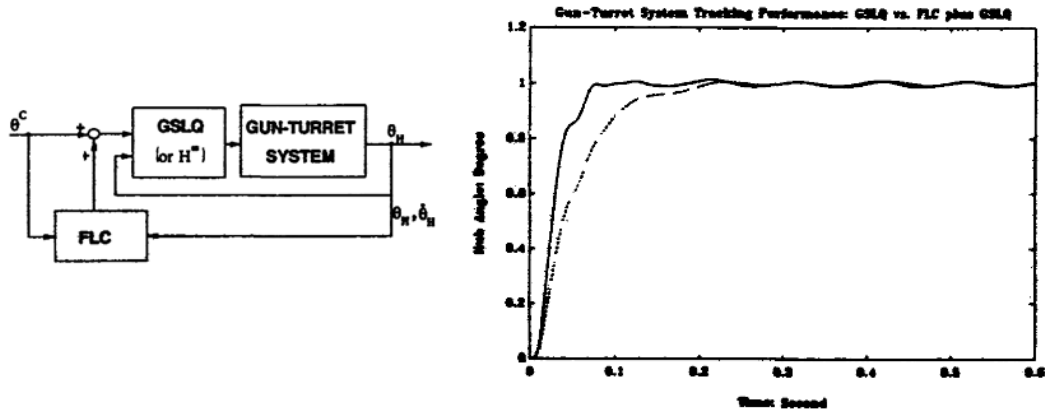


Figure 2.5: Control architecture with FLC compensation (left) and improvement of control performance after utilization of the FLC (right, with solid lines) as given in [20].

behaviour of the system, i.e. a kind of sensitivity. They introduce an adaptation mechanism to the control, using this sensitivity information. This approach seems very suitable for our problem as well. However, one should note that, in order to be able to perform the design given in this approach all the system parameters must be known precisely.

In [17] authors compare different order-reduction techniques being "Balanced Realization Method", "Routh Approximation Method", and "Litz's Method" for constructing reduced order models. They report that all three of the methods gave satisfactory results.

In [20] authors apply a Fuzzy Logic Control (FLC) in order to improve the tracking performance of a gun-turret system. They apply a Mamdani type FLC as an outer loop on top of a robust controller and achieve a significant improvement in position tracking response (see Fig. 2.5). However, they use 11 fuzzy sets during fuzzification, resulting in 121 fuzzy rules. Both design, and implementation of such a controller are impractical.

In [22] authors incorporate a full-state feedback controller for the speed control of a flexible mechanical system. They use a 3 inertia model connected with flexible links. They give simulation results comparing full state feedback and simple PI control approaches; showing that full-state feedback damps closed-loop oscillations very

effectively, while for standard PI the oscillations must be sensed at the first mass speed in order to be suppressed.

In [23], authors propose standard sinusoidal-input describing functions (SIDF) method for the control of electro-mechanical pointing systems. They show the effectiveness of their method by various simulations. However, they have no precautions for parameter variations and robustness.

In [29] authors incorporate a 10-dimensional state-space model for the gun-turret system of a helicopter. They develop an “advanced integrated controller” which consist of robust, non-linear and intelligent controllers. The authors emphasize the fact that better performance needs higher control power, which is limited by the drive performance of the motors. In their approach by employing a fuzzy controller as the higher level controller, maximum outcome has been obtained from the motor without altering the control power. They report that “It is well-known that a linear controller cannot effectively tolerate severe non-linearities which inherently exist in most of the real dynamical systems. This is especially true for the gun-turret system. With the half-width of the backlash increased by 0.2 degrees, the step response of the closed-loop system under the linear robust controller is greatly deteriorated. When the half-width of the backlash is increased to 0.5 degrees, the change of the operating condition of the backlash has literally destabilized the overall closed-loop system (i.e. shifting the closed-loop poles due to changes of operating conditions of the non-linear elements). This situation naturally demands a more robust non-linear adaptive controller which can intelligently compute the appropriate gain values based on the new operating conditions arising from non-linearity effects and/or environmental changes.” The main drawback of their approach is the fact that during the control design a very-well known system model is required. Moreover, the resultant controller is static, with a complicated structure and various parameters fixed via controller design (see Fig. 2.6).

In [27] the subject of the study is more general and it is vibration control of a two mass system (note that, motion platforms are very popular examples of such multi-mass systems). In the study, resonance ratio control (RRC) concept is introduced. In this concept, an observer is used in order to sense the reaction torque information

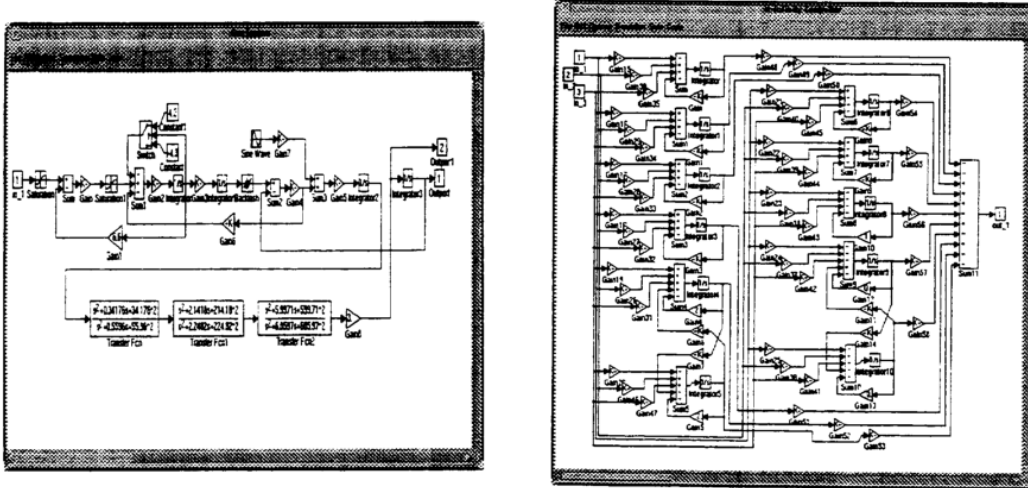


Figure 2.6: (Simulink models used for system dynamics (left) and H^∞ controller (right) in [29].

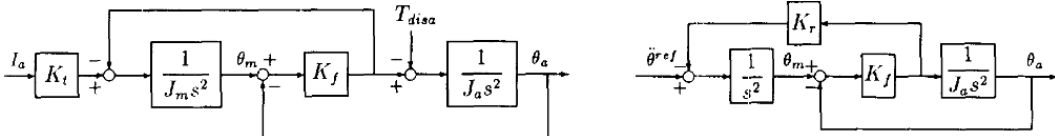


Figure 2.7: 2 mass system model (left) and Resonance-Ration Control (RRC) as employed in [27]. Here K_r term is to be adjusted to achieve desired inertia ratio of the two masses, corresponding to the resonance frequency

between the rigid bodies; and then, this information is employed in order to produce additional motor torque via observer feedback. This additional torque physically corresponds to controlling effective motor shaft inertia, in other words the “resonance ratio”, which is defined as a function of the ratio of load and motor shaft inertias (see Fig. 2.7). Authors succeed in suppressing second mass position oscillations by this way. However, no significant improvement in the agility (speed tracking response) of the system is seen. This is expected, as by increasing the net total inertia using RRC, achievable acceleration levels are also decreased. The need for a torque observer or sensor is the second drawback of the approach.

In [25] authors enhanced a cascaded internal model controller with a LQR controller to form a “Hybrid Optimal Controller” architecture. They perform the design in discrete-time. The design of controller needs a well-fitting model of the system (10th order for the specific case of the study) and there are 9 steps to design the controller, based on this well-known model. They provide only simulation results to demonstrate

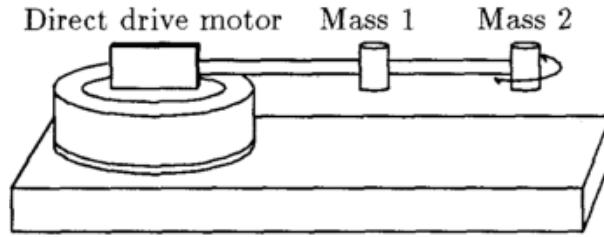


Figure 2.8: Schematic of the system under consideration in [34]. Such systems are usually equivalent to motion platforms subject to our study.

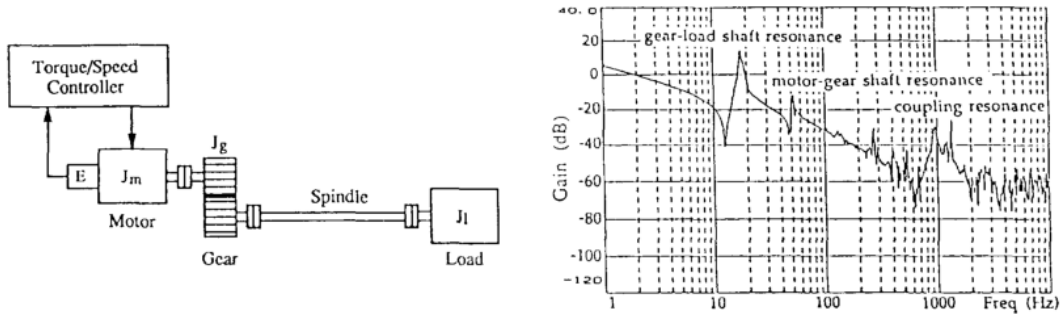


Figure 2.9: 3 mass system schematic (left) and Frequency Response Function (FRF) (right) for the test system used in [30].

the performance of their design approach. The lack of experimental results indicates that the practical implementation of such a design is not straightforward.

In [30], speed control of a three-mass system is studied (see Fig. 2.9). Backlash of the gears used in the system is also taken into account and modeled as a dead-zone non-linearity. Two observers are employed to measure the torque provided at the output of the gear stage and the disturbance torque (see Fig. 2.10). Authors focus on the performance of the observers used and report good results. A very similar study was reported in [32] with only two masses in the system rather than three, and usage of Kalman filters as state estimators, rather than Luenberger type observers employed in the previous study. Several similar studies (full-state feedback combined with linear control) may be cited in the literature (e.g. [34],[37],[39],[45], [46],[63]). Despite the popularity of “full state feedback via observers combined with linear control” approach, as stated before, there are some limitations. The performance achievable with such architectures has been analysed by Szabat and his colleagues in 2007, and they have shown the limitations of the approach analytically (this topic will be revisited later in this section).

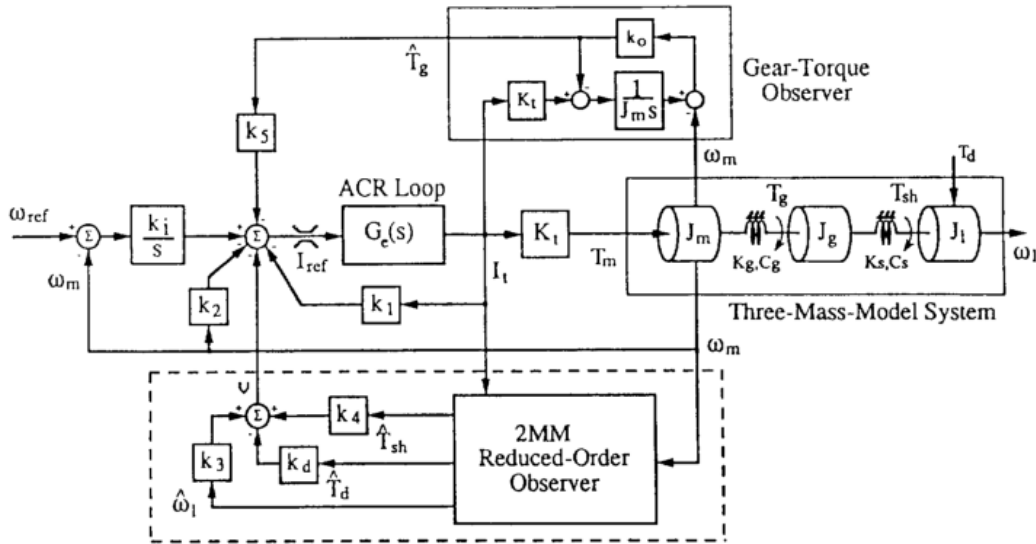


Figure 2.10: Control architecture for the speed control of a 3 mass system, as used in [30].

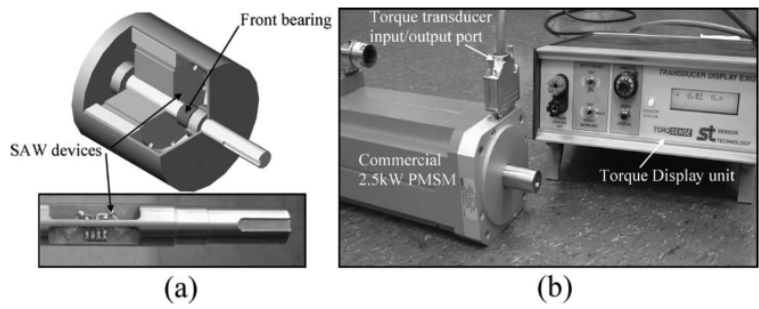


Figure 2.11: Surface Acoustic Wave (SAW) shaft torque transducers (left) and measurement infrastructure used by O’Sullivan and colleagues [66].

Despite the control approach is very similar with the studies just mentioned, it is worth mentioning O’Sullivan and his colleagues’ approach ([64],[66]): In systems with full-state feedback, observers are employed for providing information on immeasurable states or variables. Performance of these observers is very dominant in the overall system performance. If one could be able to use sensors for directly measuring shaft torque of the motor with high quality, at least one of these observers would be unnecessary. Keeping this fact in mind, these researchers studied the ways of implementing a rugged and simple way of torque measurement and developed Surface Acoustic Wave (SAW) transducers for this purpose (see Fig. 2.11).

In [31], authors describe the infrastructure used for control system development at the United States Army Research Laboratory: They use a mechanical test bed, connected

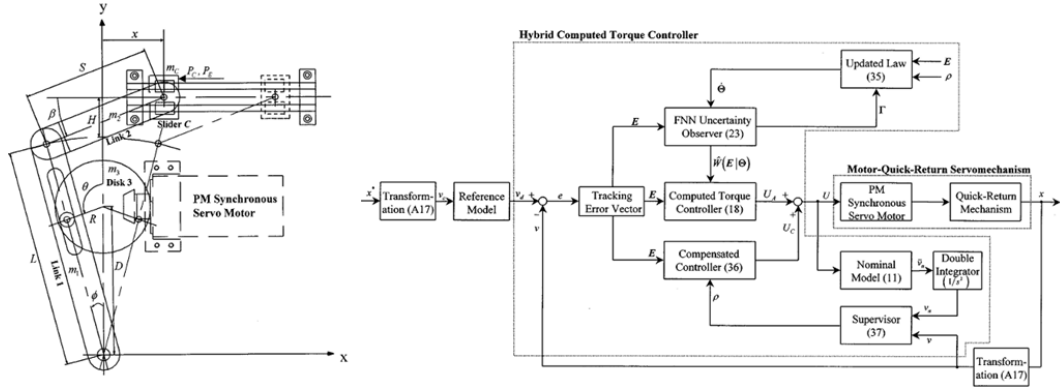


Figure 2.12: Schematic of the quick return mechanism (left) and proposed control architecture (right) in [50].

as hardware in the loop to the real-time computers in which controllers are implemented. The infrastructure used is very similar to the one used during this study. It is worth noting that after the conference in which this infrastructure was explained, there have been no papers published in American Control Conference (ACC) on gun-turret control systems. This implies that the studies conducted thereafter might have been published with non-explicit titles on industrial conferences etc. .

In [50] a Fuzzy Neural Network is employed as an uncertainty observer and it is combined with a computed torque controller to constitute a novel controller architecture used to control a Motor-Quick-Return Servo Mechanism (see Fig. 2.12). In this architecture, the non-linearities inherent to the mechanism are taken into account by employing feed-forward models for computed torque, while uncertainties are handled by the Fuzzy Neural Network (FNN) Uncertainty Observer. Despite, this architecture takes most of the non-linearities into account, the computed torque model must be well developed. Moreover, speed of convergence of the FNN with a feed-forward network implementation is a well-known drawback for the use of such structures in real-time control.

In [48] and [49] , authors investigate the two mass flexible system speed control problem in terms of resonance suppression. They use a standard PI controller cascaded with several different types of filters for resonance suppression used in practice. They compare performances of low-pass filtering, notch filtering, bi-quad filtering and acceleration feedback methods to suppress the oscillatory behavior of the closed-loop system due to open-loop resonance. Their findings can be summarized as: Low-pass

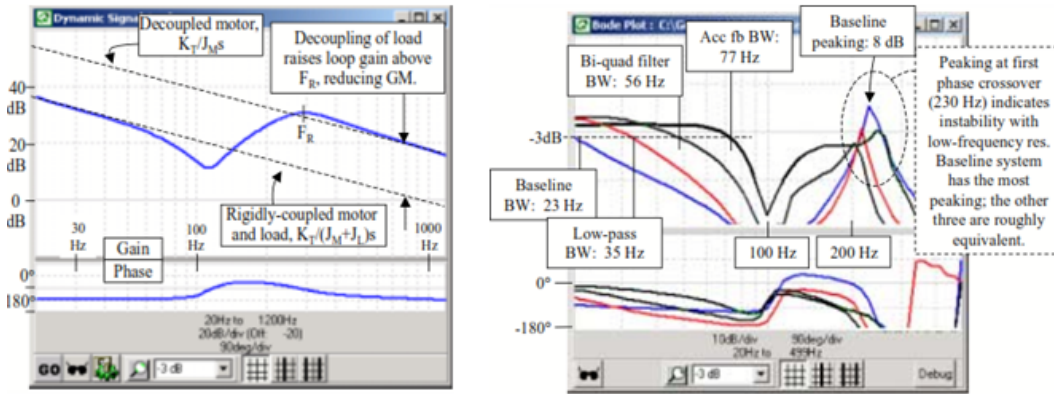


Figure 2.13: FRFs of the open-loop system (left) and closed-loop system (right) showing speed control performances achieved with PI control cascaded with different type of resonance suppression methods in [49].

filters are popular, but evidently they sacrifice performance to avoid instability; notch-filtering works better, however any shift in the resonance frequency during operation may cause instability (robustness is weak); bi-quad filtering works well in theory, but similar to notch filtering, it is not robust; acceleration feedback works best among other methods, as it may be used to separate resonance and anti-resonance frequencies efficiently; however, need and design of an acceleration observer is the critical issue. (see Fig. 2.13). In [48] step responses for the speed control are also given for comparison. The authors find that the bi-quad filter (simply, inverse of the mechanical system) gives the best result, however it cannot be used in practice since it is very prone to any shift in system behavior (see Fig. 2.14).

As stated earlier, Szabat and his colleagues from Wroclaw University of Technology, Poland have performed several studies on the speed control of multi-body systems (it is well known that, although the studies have been presented as "industrial", Poland is developing its MBT coded PL01 since the mid of 2000s, and these studies might be directly or indirectly part of the project). In their enlightening work of 2007, they analyse the limits of PI control for the speed control of a two-mass system. In their study, it is summarized that the two-mass lumped system state-feedbacks can be grouped in three different categories (see Fig.2.15). With only one type of feedback, a classical PI controller can only control one free parameter of the closed loop system dominant pole: either damping or natural frequency. In order to control both damping and resonant frequency at least two feedbacks from two different categories must be

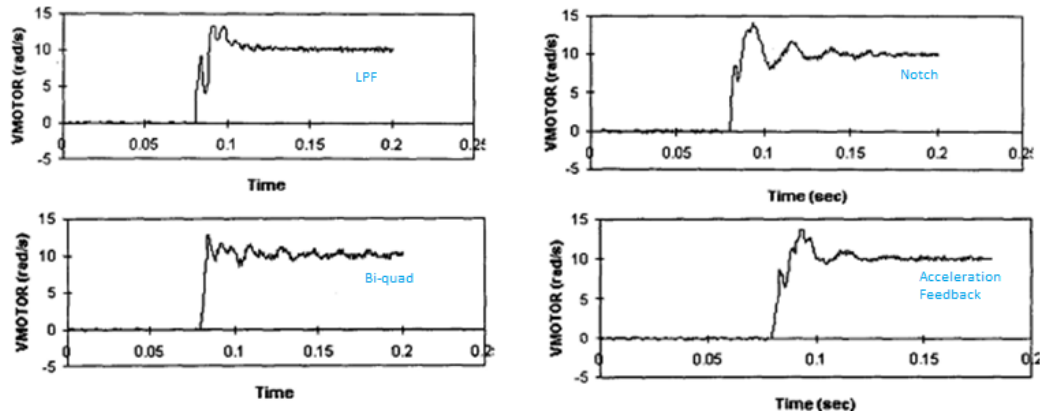


Figure 2.14: Step response of the first mass speed with different type of resonance suppression methods used in conjunction with PI control ([48]). Although bi-quad filtering seems to give the best result for the single experiment, its robustness is unacceptably poor.

employed. For a three-mass system, this analysis can also be extended as in Fig. 2.16, by modeling the effect of the third mass as a part of model uncertainty. The simplest feedbacks that can be employed are first mass and second mass angular velocities, which are already measured via sensors in most motion platforms. These feedbacks can be used as "Group B" feedbacks. "Group A" feedback is actually the shaft torque for the first shaft, whether it is derived from derivatives of the speeds or from a direct measurement. For motion platforms a reliable direct torque measurement is not available, some sort of observer structure must be employed in order to estimate the shaft torque. This approach leads to the architecture proposed in [46] with PI and PID controller implementations.

Having quantitatively evaluated the limits of PI speed control on two mass systems Szabat and his colleagues have had several attempts to apply non-linear control techniques to multi-mass system speed control to achieve better performance.

In [68], they propose a model-reference adaptive controller (MRAC) based on neuro-fuzzy implementation. They employ a standard second order linear system model as the reference to tune the neuro-fuzzy controller. This tuning aims at making the overall closed-loop system behave similar to the reference system model (see Fig. 2.17 for the general structure). The authors implement the adaptive fuzzy controller as a standard feed-forward neural network as shown in Fig. 2.18. The weight parameters

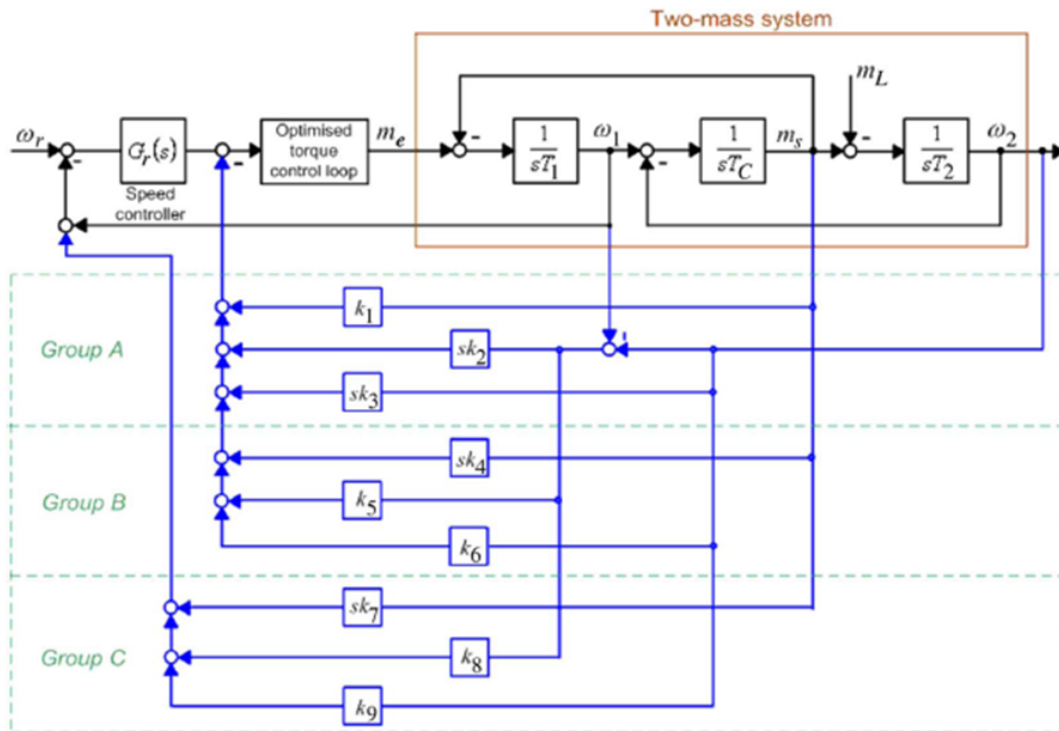


Figure 2.15: The state feedbacks grouped considering their effects on closed-loop pole locations for a two mass system [67]. Here m terms stand for torques; T terms stand for time constants (stiffness and inertias) and ω terms stand for angular speed

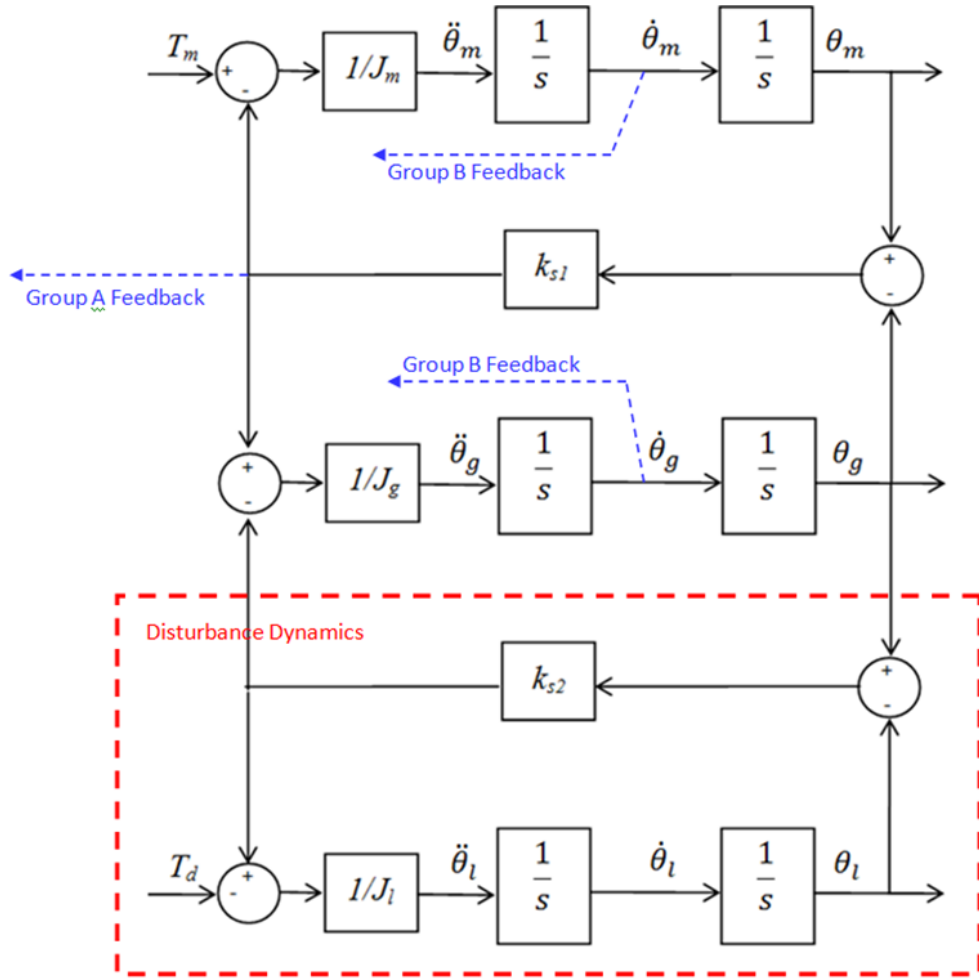


Figure 2.16: Block diagram representation of the three-mass mechanical system with simplified dynamics ignoring viscous damping terms.

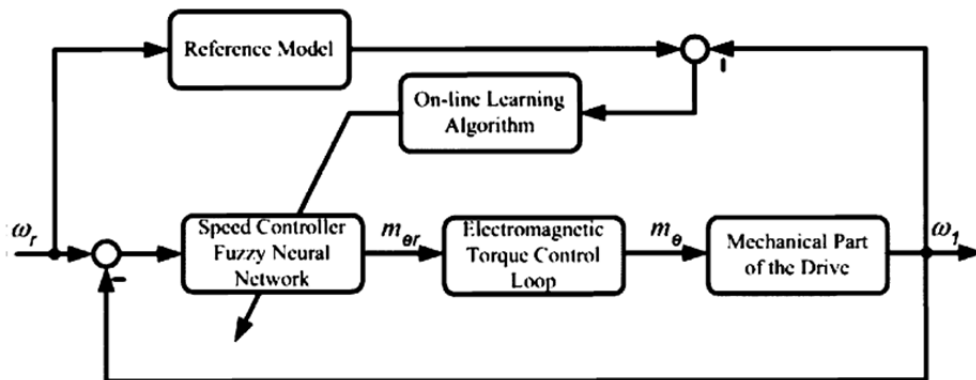


Figure 2.17: General control architecture used in [68], in which Model-Reference Adaptive Control is combined with Neuro-Fuzzy Controller.

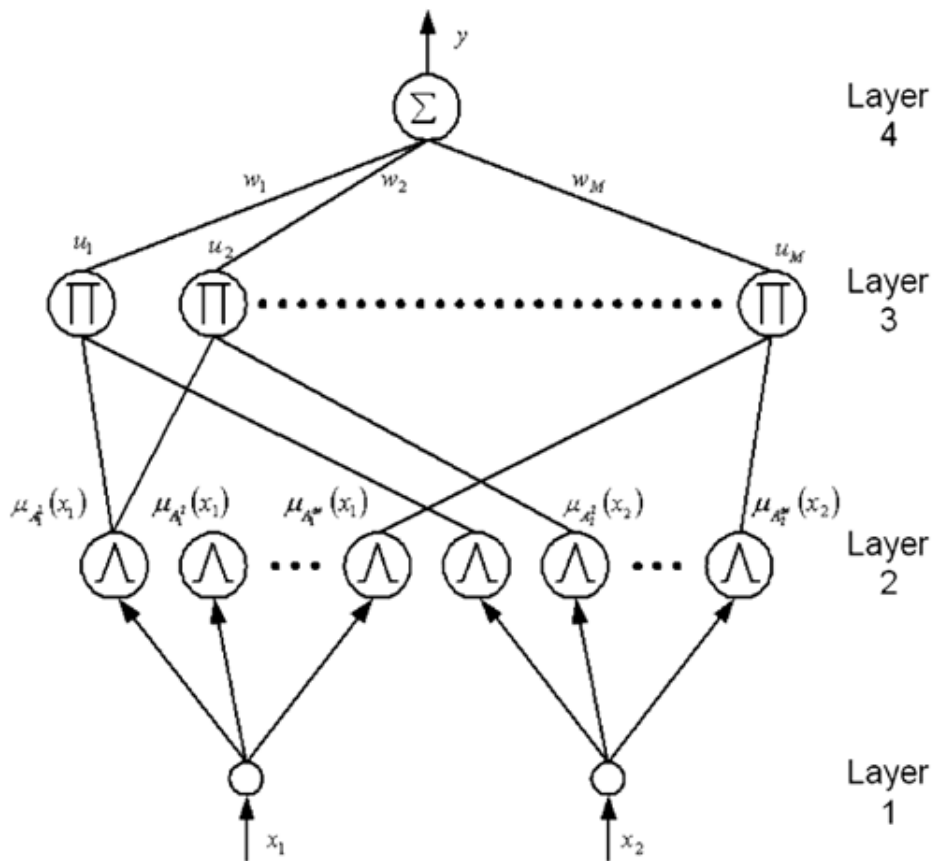


Figure 2.18: Internal structure of the "Speed Controller Fuzzy Neural Network" given in Fig. 2.17.

between layers 3 and 4 (i.e. w_i values) are adapted using the common gradient-descent algorithm.

The results presented in [68] are quite interesting, and a sample of these results are quoted in Fig. 2.19. As seen in the subplot "d" of this figure, the weights of Layer-3 of the neural network are updated in order to minimize the tracking error of the motor speed feedback, and in about 10 seconds they converge.

Since the findings in [68] are quite interesting for the purpose of controlling a motion control platform's speed in an adaptive and robust fashion, without any need of system parameters; simulations have been performed, using the same controller structure with a three mass system model. The results from our simulations are given in Fig. 2.20 and Fig. 2.21. As seen in Fig. 2.20, for our case, even during simulations, the step response does not converge to that of a linear system. Moreover, as given in Fig. 2.21, the weights continue to update significantly even after 500 s. Hence, the

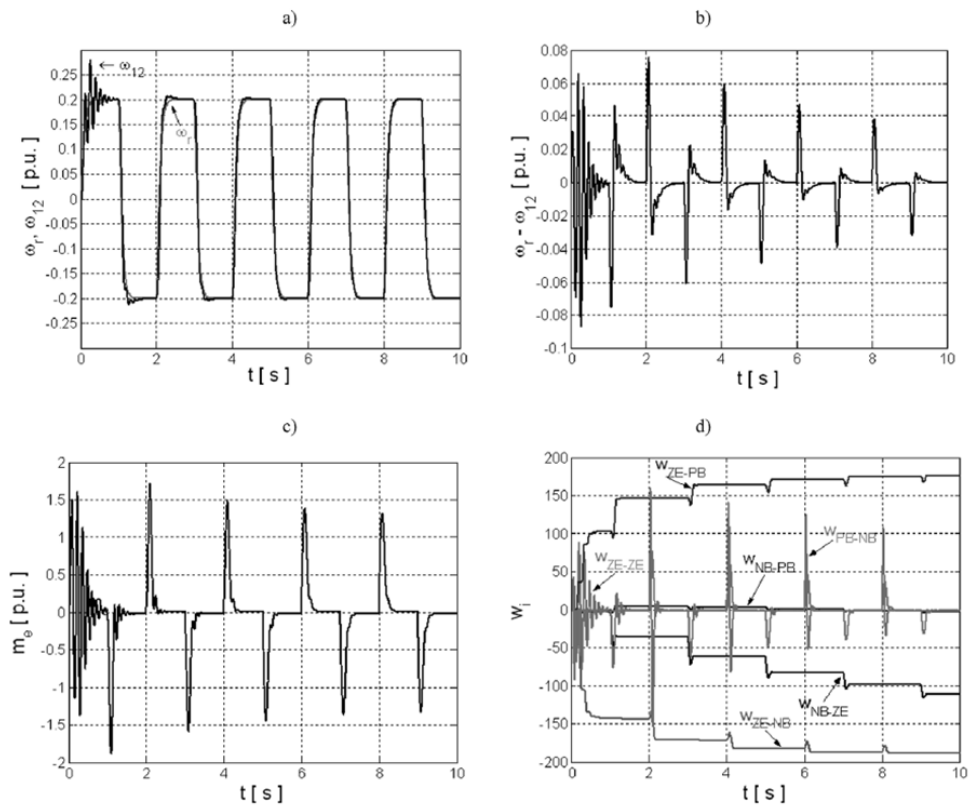


Figure 2.19: Speed output, speed error, motor torque and weight update plots from a sample speed controller operation obtained in [68].

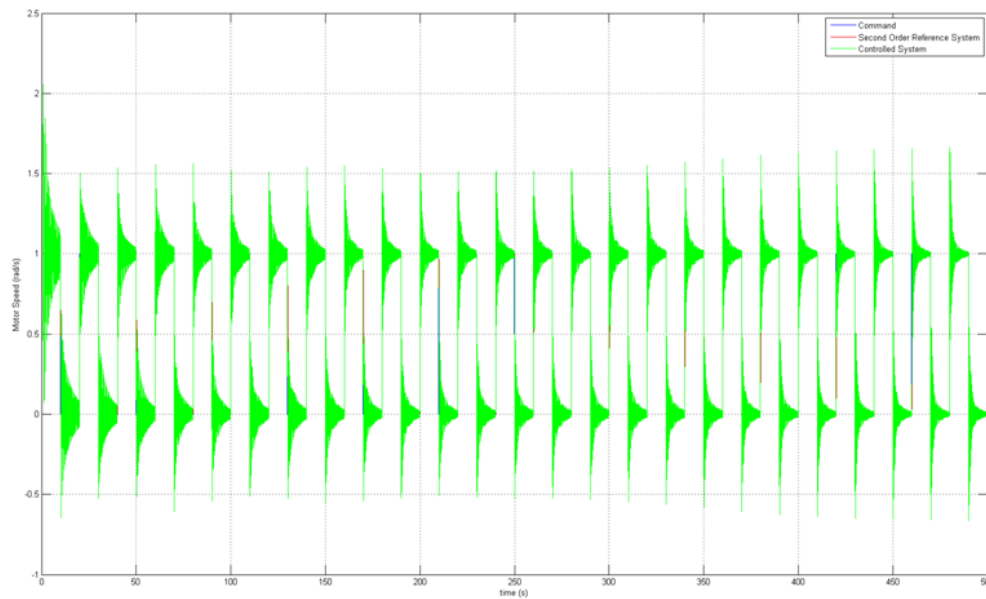


Figure 2.20: A time-domain comparison plot from our simulations with the same neuro-fuzzy controller in [68] used for a three-mass system; showing the poor convergence performance with under-damped step response at steady state.

following questions arise:

- Is a feed-forward neural network -originally designed for memorizing static mappings- enough for "learning" the dynamic behavior of a real-time controller?
- How can one evaluate the convergence performance of such a controller quantitatively?
- What is a "good reference system" to be used in MRAC? Is a second order linear reference system feasible for every case?

In [74], Szabat and his colleagues propose exactly the same control architecture, with the slight difference that the fuzzy rule-base is adjusted to have a sliding-surface type of mapping (see. Fig. 2.22). Then the adaptation algorithm alters the switching border of this mapping by updating the neural-network weights using gradient-descent. Authors show the good performance of the architecture on an experimental setup. However, same questions about the previous study are still valid for this case, enriched with the practical application difficulties of chattering caused by the sliding

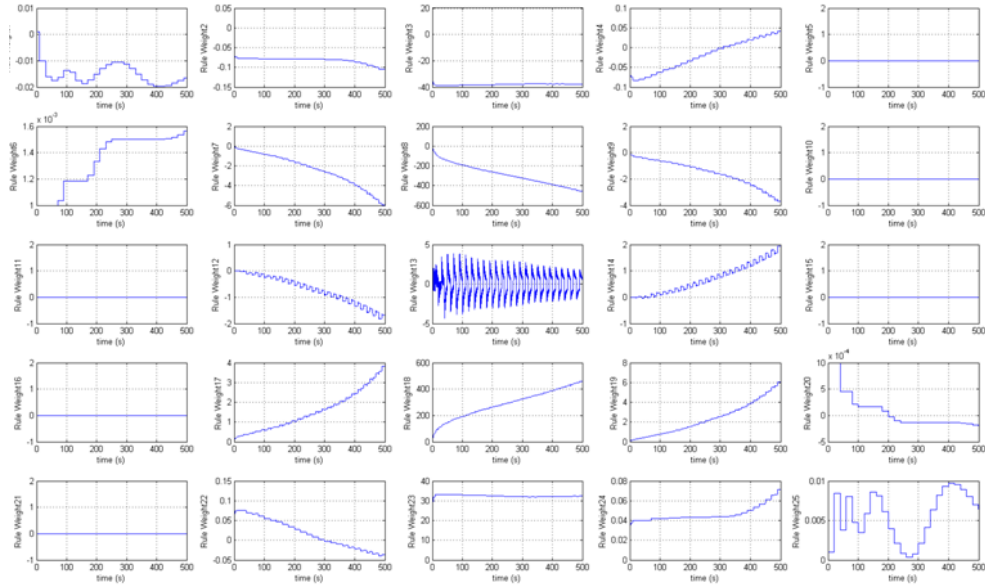


Figure 2.21: Typical weight updates from a simulation conducted by us, employing the neuro-fuzzy MRAC architecture proposed in [68]. This graph shows that the convergence of the architecture proposed by the authors is not guaranteed.

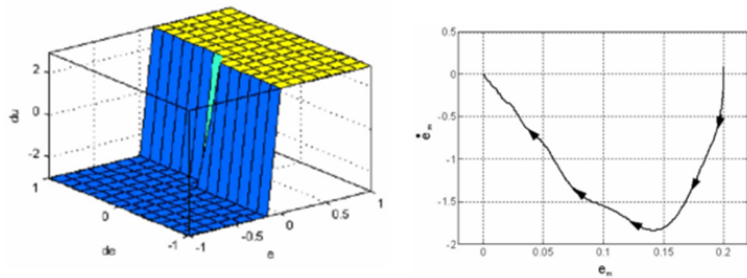


Figure 2.22: The sliding surface implemented in the adaptive neuro-fuzzy structure and a sample phase portrait as given in[74].

mode control. Actually, Sabanovic and his colleagues applied sliding mode control (SMC) to several motion control systems ([56]). Despite their encouragement in employing SMC in motion control, evaluation of a sliding surface for successful control requires an accurate system model, which is not practical for our case. Moreover, chattering caused by sliding modes is practically unacceptable and requires performance reduction to avoid.

In 2008, the same researchers propose a simpler adaptive control architecture based on variable gain PI control and Extended Kalman Filtering (EKF) (see Fig. 2.23). Actually, the architecture they use is very similar to those used in 1990s' PI com-

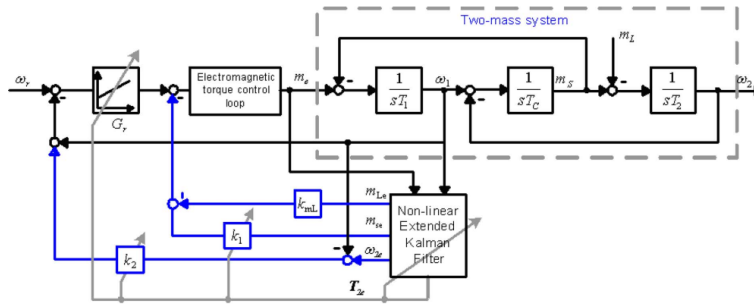


Figure 2.23: The non-linear adaptive control architecture proposed in [73].

bined with acceleration feedback. In the proposed architecture, PI control is replaced with variable gain (non-linear) version and the observer for estimating the acceleration torque is replaced with a (non-linear) EKF. These replacements are due to a need for a non-linear (or higher order) control for two-mass systems (since they showed the limitations of PI before, quantitatively); and performance drawbacks of the Luengerer type observers (for which they propose the EKF observer). On the other hand, the observer proposed by them is a Kalman filter whose performance relies on a good system model and known disturbance characteristics. In a 2012 dated study ([82]), the same authors propose an off-line non-linear Kalman filter to be used as an identifier. Then, a linear Extended Kalman Filter is used during operation, in order to estimate the system states to feed them back into a PI speed controller. The change in the approach of the same researchers may be considered as a clue for practical difficulties of application of a non-linear Kalman filter.

In [79] and [81] -again Szabat and his colleagues- propose Model-Predictive Control for speed control and vibration suppression for a three mass system. In this study output and controlling variable limitations were also embedded into the controller design and the control surface in Fig. 2.24 is obtained which uses first and third mass velocities as input. Looking at this figure, the controller seems like a "sliding-mode" one and tries to equate first mass velocity to third mass velocity; even if there are also other state variables used as inputs to the controller. The authors use off-line evaluation of the controller and embed it into a look-up table for on-line operation. The authors also claim that the resulting controller is robust to parameter changes. However, due to probable practical difficulties, only simulation results are provided.

Actually, a literature survey on the speed control of motion platforms could well be

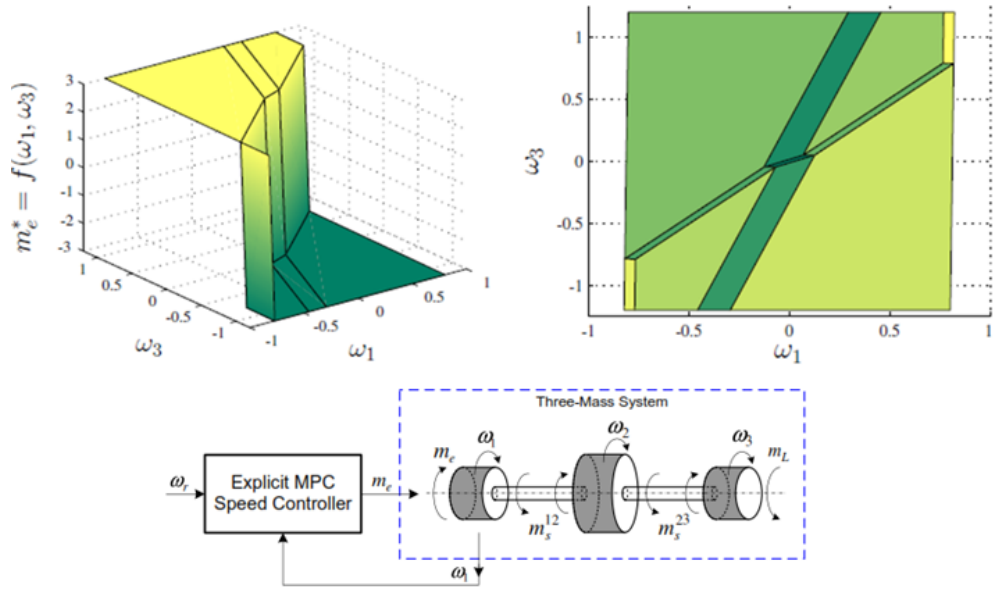


Figure 2.24: Simple architecture proposed with model-predictive control (top) and motor torque mapping from first and third mass speeds for the model predictive control design performed (top) in [79] and [81].

extended to include compensation of friction and backlash, which are inherent and effective non-linearities in such systems. Moreover, there is a vast number of papers on both modeling and compensating these phenomena. On the other hand, the focus of this study is not backlash or friction compensation, but the speed control comprehensively. Moreover, our colleague Yumrukcal had an MSc. thesis on backlash modeling ([87]) and Sincar had an MSc. thesis on friction compensation ([86]). The reader is kindly invited to investigate the literature surveys of these studies and discussions on friction and backlash are postponed until system modeling and identification section, at which simple models of these phenomena are described for utilization in simulations.

At this point, it is worth to summarize the evaluation of the literature on speed/position control of multi-body systems:

- Literature on gun-turret speed/position control is limited due to confidentiality issues.
- Several methods have been applied for the speed control of motion platforms ranging from standard PI to advanced techniques such as H^∞ , ad-hoc tech-

niques similar to neural-networks and fuzzy logic.

- As analyzed by Szabat and his colleagues in 2007 ([67]) even if with full-state feedback, a PI controller can achieve limited performance for even a two-mass system.

The proposed methods can be classified in terms of their drawbacks, as below:

- Methods that need a well-developed and accurate system model:
 H^∞ , LQG/LTR, SMC, EKF
- Methods not adaptive: H^∞ , LQG/LTR, SMC, EKF
- Methods with convergence difficulties: MRAC with NF implementation,
- Methods with practical issues: SMC including NF implementation.
- Methods with limited performance: PI and its variations.

In the light of these findings, one can state that a novel control architecture should possess the following properties:

- The architecture should not need a well-developed and accurate system model (black-box). If a model is needed, a simple linear model well describing the basic system behaviour (gray-box) should be enough.
- The architecture should be adaptive. As the system parameters drift in time, the performance loss of the controller should be kept minimum.
- The architecture should converge in a short time. Preferably, the convergence property should be quantitatively analysed.
- The architecture should be applicable to a practical system. For this property, it should be realizable with standard development tools (e.g. MATLAB / Simulink) and there should not be limitations similar to actuator bandwidth limits or excessive control efforts.

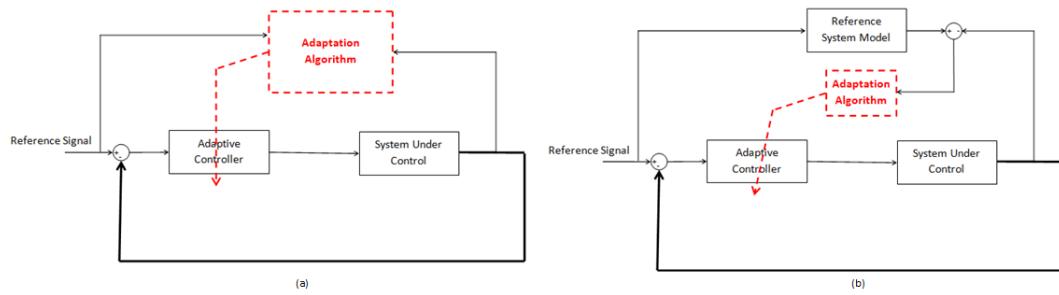


Figure 2.25: General adaptive control scheme (a), and Model-Reference Adaptive Control (MRAC) scheme (b).

- The architecture should be suitable for utilisation in optimizing a performance measure. The process of utilization should possess an acceptable level of design effort.

Keeping the above criteria in mind, adaptive structures that do not need a well-developed model of the system to be controlled might be good candidates as controllers. At this point, it would be worth visiting adaptive control and intelligent control techniques very briefly.

Adaptive control is a mature topic having its roots in the 1950s [1]. It is based on adaptation of controller parameters as the closed-loop system continues its function, as seen in Fig.2.25. It has basically two types: Indirect and Direct. In indirect adaptive control, a pre-tuned identifier is employed to update controller parameters. Whereas for the direct case, the reference system error is used to update controller parameters in a direct fashion. Since it is a wide area of research and it has several variations, the review will include the version utilised during this study: Model-Reference Adaptive Control (MRAC). Model Reference Adaptive Control is a variation of adaptive control, in which the output of a reference system model is used to determine the error measure in updating the controller parameters as given in Fig. 2.25.

In their classical paper [1], Narendra et. al. investigates the stability issue for adaptive observers and controllers. They start with identification of an algebraic equation and extend their analysis to continuous-time linear systems. They utilize linear control theory tools in order to evaluate stability conditions (convergence of both the output error and parameter estimation error to zero). In [6], the author uses Narendra's approach and increases the transient performance by changing the feedback error

definition. The faster convergence rate has been proven by using the "comparison of gradient of a Lyapunov function" approach.

In Åström's adaptive feedback control survey paper [5], a very comprehensive summary of the topic is introduced. In this paper, it is stated that the robustness of the adaptive controllers subject to unmodeled dynamics would be an area of active research. Moreover, it was stated that although the global asymptotic stability of adaptive controllers under certain assumptions could be proven; their transient performance would be much more difficult to analyze and it was an active area of research.

In [7] it was stated that "Despite global stability, the mechanism and the convergence properties of existing adaptive algorithms may be easily affected when exposed to uncertainties from a practical point of view". In the same study, it was proposed that one should work on the convergence of the adaptive behavior while synthesizing the controller. With this idea in mind, they offer a modification to the error model and show that the rate of convergence may be improved by this way. They -as expected- use comparison of the gradient of a Lyapunov function in order to prove the improvement in the rate of convergence.

In [12] it is referenced that "under exact matching conditions direct adaptive control algorithms can be used to control a stably invertible system". It is also stated that, usually it is easy to show that error goes to 0 as time goes to ∞ ; however, establishing rules for rate of adaptation is not an easy task. Moreover, it was proposed that fast adaptation should be used initially to minimize the transient error and achieve good l_∞ (error norm) performance

Miller and Mansouri propose a linear periodic controller to be employed in a MRAC structure and they improve its (mostly noise immunity) performance by performing probing, estimation and control operations in parallel [78]. Their controller is specifically designed for linear time varying systems.

As stated in a recent survey conducted on MRAC [84], the state of the art in MRAC has been converging towards utilization of soft computing techniques, such as neural-networks, fuzzy logic and genetic algorithms in constituting different parts of the MRAC architecture. This stems from the fact that, even if it is easy to perform math-

emathical analysis (as in [2]) and prove several performance criteria (such as stability) for linear systems; a practical system under consideration cannot be modeled at a complexity which is both simple enough to analyze overall system's behaviour mathematically and complex enough to catch all the dynamics of the system. Soft computing techniques have been recently used as a remedy to this challenge.

Soft computing techniques range from neural networks to fuzzy logic, genetic algorithms and reinforcement learning. In order to be able to use such structures in practical real-time control systems, fast convergence of such structures is a key issue. Recent studies on soft computing has developed new forms of neural networks which can both represent dynamic systems and converge faster than its predecessors (including the adaptive structures similar to ART-2 [28]). These type of neural networks will be reviewed later in the manuscript. Here, a brief summary of convergence issues in neural networks will be given.

ANNs are structures which can update their parameters so as to approximate a non-linear mapping. There are usually two methods to update parameters of a feed-forward ANN [61]:

Simple gradient descent:

$$w_{ji}(n+1) = w_{ji}(n) - \eta \frac{\partial \xi}{\partial w_{ji}} \quad (2.1)$$

Batch mode:

$$\Delta w_{ji}(n) = -\eta^* \frac{\partial \xi}{\partial w_{ji}} + \alpha^* \Delta w_{ji}(n-1) \quad (2.2)$$

in the equations (2.1) and (2.2), ξ represents the cost function to be minimized, w_{ji} represents any weight parameter being updated, η represents the learning rate and α represents the momentum factor. The update of the learning rate itself is an issue highly studied in the literature. There are basically two approaches: Local and Global Adaptation.

Local adaptive techniques are based on the weight specific information. Some of these techniques are:

- Sign Changes: Increase the learning rate as long as the sign of the specific gradient of cost function with respect to specific weight remains unchanged. Otherwise, decrease the learning rate.
- Delta Bar Delta: Control the learning rates by observing the sign changes of an exponential averaged gradient. Moreover, increase the learning rates by adding a constant at each iteration, rather than multiplication.
- SuperSAB: Same as delta-bar-delta except the increase in the learning rate is exponential. Moreover an upper limit η_{max} is employed.
- Quickprop: An optimization of the back propagation based on Newton's method. If between two iterations gradient decreases in magnitude and changes sign, then use a parabolic estimate of the MSE to determine an estimation of exact learning rate to find the minimum of ξ .
- Rprop: Similar to Quickprop, but uses a "Manhattan Learning Rule" for weight updates. Only the sign of the derivative is employed to find the learning rate update.
- Dynamic Momentum Factor: Momentum factor α is updated at each iteration step depending on the current value of the momentum factor.
- Dynamic Learning Rate: In this method, the learning rate has its own dynamics, which is determined by the current value of the specific gradient.

Global Adaptive Techniques, in which the overall state of the network is employed for weight updates. Some of these techniques are cited below:

- In [47], authors proposed a modification for Quickprop in order to have better convergence characteristics to converge to global minimum, rather than local minimum.
- In [26], authors propose an approach for the Radial-Basis Neural Networks (RBNNs). In this modified gradient-descent (GD) approach, a dead-zone around the origin of the error coordinates is incorporated in the training rule. They prove their convergence improvement by the comparison of gradient of the cost function magnitude with the standard method.

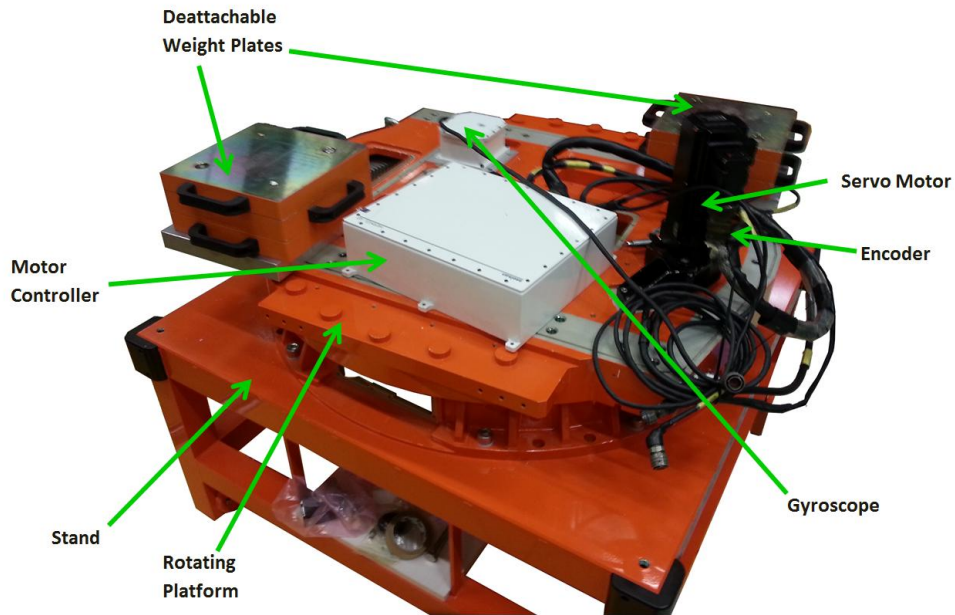


Figure 2.26: Test setup on which experiments have been conducted.

- In [53], authors proposed a method called "magnified gradient function". They start magnifying the learning rate as the local activation functions stuck at saturation points. They prove that their approach is faster than back propagation by comparing the gradient of the same Lyapunov function with the standard back-propagation method.

In summary, for the ANNs, the methods to improve convergence are usually based on heuristic updates of learning rates and momentum factors. The performance of the approaches are evaluated by comparing the magnitudes of a Lyapunov function for different cases.

2.2 The Setup Utilized for Experiments

The setup used during the experiments is given in Fig. 2.26. This is basically a rotating platform mounted on a stand. It is utilized with a servo motor with 1.4 kW rated power, an Aselsan Herkul[®] series servo controller capable of delivering up to 14 kW of instantaneous electrical power to the motor, a gyroscope for inertial speed measurement, an auxiliary encoder for position measurement. Moreover, there are two mechanical interfaces for additional weight plates in order to simulate the

load of the motion platform. A PC utilized with MATLAB-RTWT[®] and capable of communicating with Herkul servo controller is employed for implementation of the controller by hardware in the loop approach.

2.3 Chapter Summary

This chapter has been dedicated to a detailed literature on the problem of interest and the experimental setup employed has been introduced at the end of the chapter.

The literature survey shows that the speed control of motion platforms is a well-studied subject. It has been under interest of the control engineering community for more than 50 years. Several different approaches have been proposed ranging from classical PI control to advanced model-predictive control structures. The limits of the linear control theory has been recently (in 2007) analysed quantitatively, showing that even with a two-mass model a PI controller alone is not able to set the performance parameters as desired. As for the non-linear control approaches, either they are extremely complicated to implement or rely on well-known system models.

In the next chapter the problem will be first divided into its sub-problems, and then these "sub-problems" will be analysed, simulated and experimented on , in order to gain more insight on the practical aspects of the problem which is specific to the type of the system under consideration.

CHAPTER 3

SYSTEM IDENTIFICATION AND MODELING

As explained in Chapter 1, motion platforms consist of various parts. The aim of this study is to obtain a better performance for the overall structure. Hence, the modeling techniques used for different parts of the system are investigated as the initial step. The aim is performing system identification whenever necessary and developing models which will be employed during design of the speed controller. This chapter is dedicated to efforts on investigating models for the control of brushless electric motors, non-linear effects in mechanical systems and finally distributed-inertia mechanical systems in three separate sections.

3.1 Control of Brushless Electric Motors

Getting more popular every day, permanent magnet synchronous motors (PMSMs) are now widely used in industrial and military applications. These motors have a rotor on which permanent magnets are attached to form a sinusoidal or trapezoidal magnetic field distribution in space. The armature windings are on the stator, and they are used to produce an MMF which is electrically perpendicular to the field created by the rotor magnets (see Fig. 3.1). The basic advantage of these kind of motors is that they do not require any physical commutator which is very open to create electrical noise and suffer from ageing. On the other hand, absence of a physical commutator forces a requirement to achieve commutation electronically. Electronic commutation is achieved via motor controllers incorporating processing power and power electronics in the same unit. The way commutation and control of MMF in a

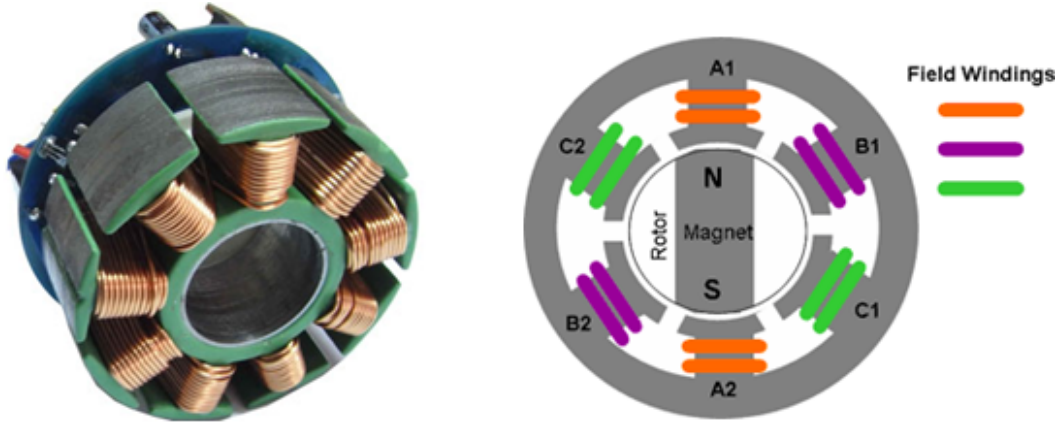


Figure 3.1: Structure of a typical brushless motor (left) and its cross-sectional schematic (right). Rotating magnetic field created by appropriate excitation of the field windings (electronic commutation) is necessary for successful operation of such a motor.

PMSM is a wide research area in power electronics. The synchronous frame PI control (see Fig. 3.2) has become the standard for current regulation of poly-phase AC machines [44], in which permanent magnet synchronous motors is a subclass. However, Multi-Input Multi-Output (MIMO) nature of this class of motors makes their performance evaluation a difficult task. Different approaches are employed in order to analyze these motors, evaluate their performance and design controllers. These approaches include, modeling of the motor electromagnetic dynamics using matrix notation (scalar notation) or equivalent Single-Input Single-Output (SISO) complex vector notation.

For a three-phase, two-pole machine the motor output torque is given by the following equation

$$t_e = \frac{3L_m}{2L_r} i_{qds}^e \times \lambda_{qdr}^e \quad (3.1)$$

where t_e represents electrical torque; L_m represents equivalent magnetizing inductance, L_r , represents equivalent rotor inductance; i_{qds}^e represents the equivalent stator current vector in electrical frame; λ_{qdr}^e represents the equivalent magnetic flux vector created by the rotor magnets in electrical frame.

For the speed control of multi-body systems, during modeling and control phases,

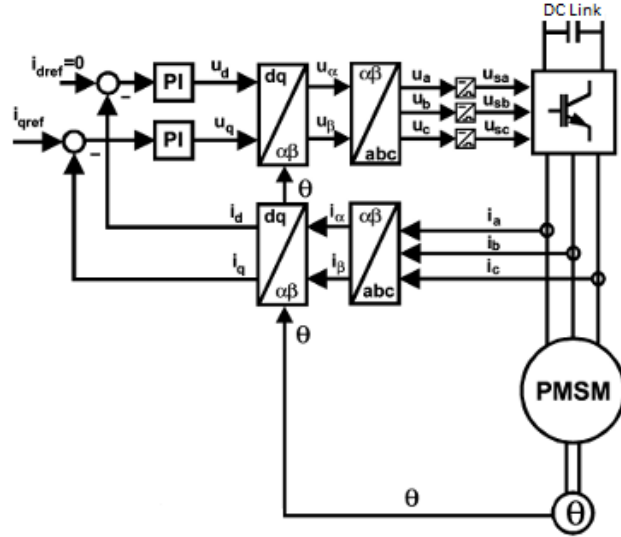


Figure 3.2: Typical field orientation architecture for the current control of a PMSM.

most of the studies (see the comparative study of Szabat et. al., [67]) assume that the motor current applied to the equivalent constant flux generalized machine's armature is proportional to the torque applied to the load as

$$t_e(t) = k_t I_{eq}(t) \quad (3.2)$$

Here k_t is the torque constant and I_{eq} is the armature current of a permanent magnet DC machine equivalent of the PMSM under consideration. Moreover, some studies assume that the dynamics governing the motor current is much faster than the dynamics of the mechanical system [45],[27], allowing the use of a simple low-pass filter as a model of the electrical motor. However, for the speed control of motion platforms, the current loop might also be under consideration. Moreover, the interactions between mechanical and electrical components of the system might be an important factor and one should have an insight of these interactions while dealing with the controller design problem. Hence, before employing the simplification of "high current bandwidth assumption", it is worth to investigate the validity of this assumption in more detail.

In this part of the study, the effects of the mechanical system components on the control of motor current, the interactions between electrical motor and mechanical system dynamics, is investigated ([85]).

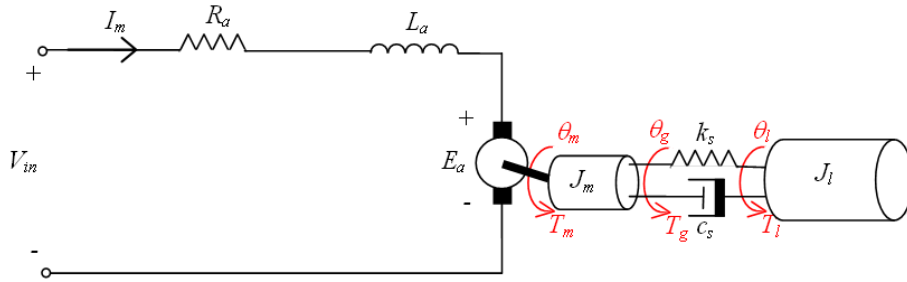


Figure 3.3: Schematic representing the system model used for analysis.

3.1.1 Simplified Electro-mechanical Model

In the control of motion platforms usually flexible lumped mass mechanical models are employed. These models usually include two [45] or three [46],[80] lumped masses connected with flexible elements. For the control of flexible robot arms even four or more lumped mass models are employed [63]. For the purpose of investigating the interactions between mechanical and electrical components of such a flexible system, the model given in Fig. 3.3 is employed. The following assumptions are made in using this model:

- The dynamics of the drive electronics are neglected.
- The motor has been modeled as an equivalent permanent magnet DC motor with constant field flux. (generalized electrical machine model).
- The mechanical system is modeled as J_m representing motor and gearbox inertia; J_l representing load inertia; k_s and c_s representing stiffness and damping coefficients, respectively, of the connections between motor and load.
- Static frictions in the system are not modeled, and the only loss in the mechanical system is considered to be due to the c_s term.

Table 3.1: Parameters of the System Model Given in Fig. 3.3 and Sample Values Used During Simulations

PARAM.	UNIT	REMARKS	SAMPLE VALUE
V_{in}	V	Terminal voltage of the equivalent permanent magnet DC motor.(applied by the motor driver)	Controlled
I_m	A	Armature current developed in the equivalent DC motor armature circuit.	Controlled
R_a	Ω	Armature resistance of the equivalent permanent magnet DC motor.	3 m Ω
L_a	H	Armature inductance of the equivalent permanent magnet DC motor.	17 mH
E_a	V	Back-emf voltage of the equivalent permanent magnet DC motor.	Controlled
T_m	Nm	Mechanical torque developed on motor shaft.	Controlled
θ_m	rad	Motor shaft position reflected to the load side.	Controlled
J_m	kgm ²	Equivalent load-side inertia of the motor shaft and gear box.	326 kgm ²
θ_g	rad	Gearbox output angular position.	Controlled
T_g	Nm	Torque at the gearbox output.	Controlled
θ_l	rad	Angular position of the Load	Controlled
c_s	Nm.s/rad	Equivalent damping coefficient for connections between motor and the load.	10 kNm.s/rad
k_s	Nm/rad	Equivalent stiffness coefficient for connections between the motor and the load.	3.675 Mnm/rad
J_l	kgm ²	Equivalent load inertia.	4400 kgm ²
k_e	V.s/rad	Back-emf constant of the equivalent DC motor.	0.125 V.s/rad
k_t	Nm/A	Torque constant of the equivalent DC motor.	0.125 Nm/A
I_m	A	Motor Armature Current	Controlled
n_g	—	Gear ratio of the gearbox (1:ng)	220

3.1.1.1 Analysis

The model shown in Fig. 3.3 consists of both electrical and mechanical components which are coupled via back-emf of the electrical motor. The parameters used in the model are summarized in Table 3.1. One can write the voltage loop equation for the electrical part as follows:

$$V_{in} = R_a I_m + L_a \dot{I}_m + E_a \quad (3.3)$$

The following equality can be used instead of E_a in (3.3)

$$E_a = k_e \dot{\theta}_m n_g \quad (3.4)$$

by using standard motor model. Even if (3.4) seems to be a rather simple equation, it is the equation describing the physical phenomenon that interconnects the mechanical system with the electrical one. Since the model representing the motor inertia is free of stiffness and damping we can simply write

$$\theta_m = \theta_g \quad (3.5)$$

Using this assumption and Newton's 2nd law of motion for the motor gives:

$$\ddot{\theta}_m = \frac{T_m + T_g}{J_m} \quad (3.6)$$

For the linearised torque of the equivalent DC motor, one has

$$T_m = n_g k_t I_m \quad (3.7)$$

For the connection part, since it is inertia free one can write $-T_g = T_l$, which in turn yields

$$-T_g = T_l = k_s(\theta_m - \theta_l) + c_s(\dot{\theta}_m - \dot{\theta}_l) \quad (3.8)$$

Finally, applying Newton's 2nd law of motion for the load inertia gives:

$$\ddot{\theta}_l = -\frac{T_g}{J_l} \quad (3.9)$$

The transfer function from input V_{in} to the output I_m can be obtained using Laplace transforms of the previous time-domain equations:

Taking Laplace transforms of (3.3) and (3.4), one gets

$$V_{in}(s) - (R_a + L_a s)I_m(s) - k_e n_g s \theta_m(s) = 0 \quad (3.10)$$

similarly, using (3.6) and (3.7), one gets

$$J_m s^2 \theta_m = n_g k_t I_m(s) - (k_s + c_s s)(\theta_m(s) - \theta_l(s)) \quad (3.11)$$

and lastly, using (3.8) and (3.9), one obtains

$$J_l s^2 \theta_l = (k_s + c_s s)(\theta_m(s) - \theta_l(s)) \quad (3.12)$$

Next, one can use (3.10), (3.11) and (3.12) to eliminate $\theta_l(s)$ and $\theta_m(s)$ and obtain

$$\frac{I_m(s)}{V_{in}(s)} = \frac{s}{L_a s^2 + R_a s + k_e k_t n_g^2 \frac{J_l s^2 + c_s s + k_s}{J_l J_m s^2 + c_s (J_m + J_l) s + k_s (J_m + J_l)}} \quad (3.13)$$

Notice that equation (3.13) obtained above can be used to find the transfer function from V_{in} to I_m for the case in which motor is decoupled from the load (i.e. "Motor Only - MO" case) by setting $c_s = 0$, $J_l = 0$ and $k_s = 0$, yielding

$$\frac{I_m(s)}{V_{in}(s)} = \frac{s}{L_a s^2 + R_a s + k_e k_t n_g^2 \frac{1}{J_m}} \quad (3.14)$$

3.1.2 Investigation of the Frequency Domain Behaviour

The SISO system models for both "Motor Coupled to Load" (MCL) and "Motor Only" (MO) cases are given in equations (3.13) and (3.14) as transfer functions. In order to investigate the interactions between electrical and mechanical components, one may compare these transfer functions and extend this comparison into frequency domain in order to have a means of observing the results on a real system, by means of frequency response tests.

In comparing these two transfer functions one must first note that they have very similar forms except the fact that the constant motor inertia term in equation (3.14) becomes a two-mass lumped mechanical system dynamics in (3.13) as expected. Another point which can be seen from the transfer functions is that the terms in denominators starting with $k_e k_t n_g^2$ couples the mechanical system to the electrical one, which

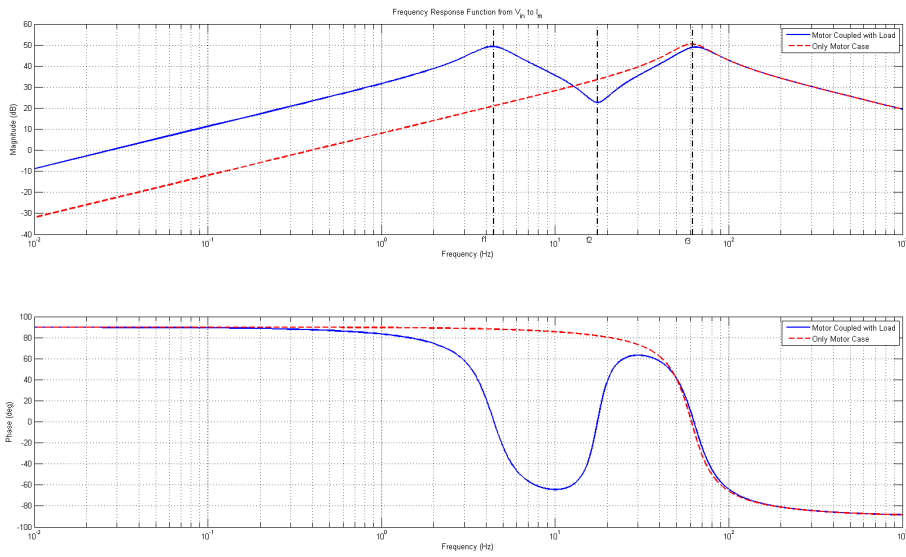


Figure 3.4: Frequency response function plot of the SISO system models given in equations (3.13) and (3.14).

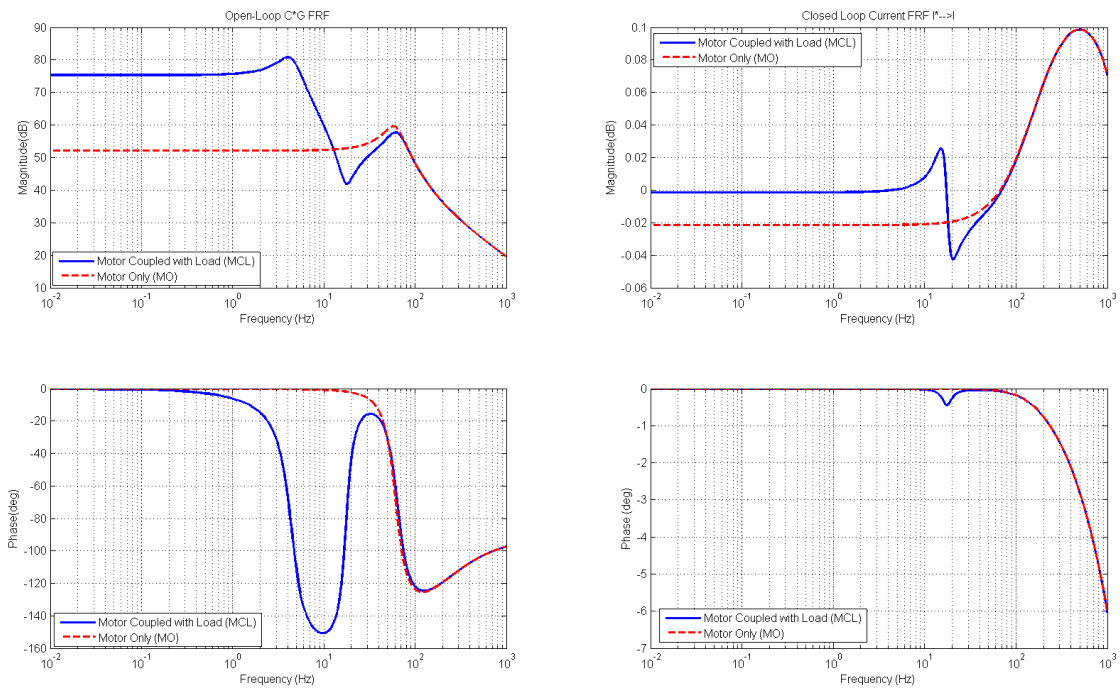


Figure 3.5: Open- (left) Closed-loop (right) frequency response function plot of the SISO system models given in equations (3.13) and (3.14) obtained with PI control with parameters $K_P = 1$ and $K_I = 1000$.

is purely an $R-L$ circuit in the absence of this term. Hence this term is the one which transform the $R-L$ circuit into an electrical motor.

The frequency response functions (FRFs) corresponding to these transfer functions, obtained with the parameter values given in Table 3.1 are plotted in Fig. 3.4. As it can be seen in this figure, the two FRFs are quite different especially at low frequencies, for which motor "sees" both inertias for the MCL case. However at higher frequencies the two FRFs become very similar, as for the MCL case the motor and load inertias are decoupled due to slow mechanical dynamics of the mechanical interconnection and motor does not "see" the load inertia any more.

One of the most important information which can be obtained from FRFs are the resonance and anti-resonance frequencies, which also usually determine the performance of the closed-loop system since open-loop gain at the anti-resonance frequency is attenuated and the amount of gain at the resonance frequency usually determines the gain margin. The resonance frequency -minimizing the magnitude of the transfer function denominator magnitude after inserting $s = j\omega$ - seen at the FRF of the MO case can be approximately found by setting $R_a = 0$ in (3.14) and finding the denominator roots, which in turn yields:

$$f_3 = \frac{n_g}{2\pi} \sqrt{\frac{k_e k_t}{L_a J_m}} \quad (3.15)$$

This term is evidently a resonance arising from energy transfer between armature inductance and motor shaft inertia. Numerical value for f_3 for our system is found as 60.9 Hz which is also observed in the frequency response plot given in Fig. 3.4. In order to increase the resonance frequency for better control either the motor inertia and/or the motor winding inductance values should be decreased.

The anti-resonance frequency seen for the MCL case can be approximately found by setting $c_s = 0$ and finding the numerator roots of (3.13), the result is obtained as:

$$f_2 = \frac{1}{2\pi} \sqrt{\frac{k_s (J_m + J_l)}{J_m J_l}} \quad (3.16)$$

This value is exactly the same as the anti-resonance of the mechanical part of the

system (starting with the motor shaft). As can be deduced from the form of the mechanical system, this anti-resonance is due to energy transfer between the combined inertia of the system and the stiffness of the connections, which is modelled as the spring k_s . f_2 is calculated as 17.5 Hz using (3.16) and this can be observed in Fig. 3.4.

The resonance frequencies observed in the MCL case can be approximately found by setting $c_s = 0$, $R_a = 0$ and solving for the roots of the denominator of (3.13) after setting $s = j\omega$, which yields the equation:

$$L_a J_l J_m \omega^4 - [k_s(j_m + J_l)L_a + J_l k_e k_t n_g^2] \omega^2 + k_s k_e k_t n_g^2 = 0 \quad (3.17)$$

the roots are then found as:

$$f_1, f_3 = \frac{1}{2\pi} \sqrt{\frac{1}{2} \left[\frac{k_s(J_m + J_l)}{J_m J_l} + \frac{k_e k_t n_g^2}{L_a J_m} \pm \frac{1}{L_a J_m J_l} \sqrt{J_l^2 (k_s^2 L_a^2 + k_e^2 k_t^2 n_g^2 + 2k_s k_e k_t n_g^2 L_a) + J_m^2 k_s^2 L_a^2 + 2J_m J_l (k_s^2 L_a^2 - k_s k_e k_t n_g^2 L_a)} \right]} \quad (3.18)$$

This result gives the first and second resonance frequencies for the MCL case as 4.43 Hz and 63.2 Hz which are also compatible with Fig. 3.4. Note that for the second resonance the energy transfer is mainly between the inductance and the motor inertia, while for the first resonance the effect would be more mechanical, as it is a rather low frequency resonance.

3.1.3 Closed-Loop System Performance

In the previous sub-section we have compared open-loop system characteristics for MCL and MO cases, and found out that they are significantly different. Despite the open-loop responses of the MO and MCL plants are quite different at low frequencies, while performing closed-loop control, controller transfer functions and feedback effects also come into account. In this sub-section the closed-loop performances will be compared to discover if the open-loop discrepancies can be compensated during the closed-loop operation. For this purpose, the closed-loop performances are observed and compared for a certain type of controller.

In this study, a classical PI controller is employed for both MO and MCL cases. In determining the controller parameters one can note that the transfer functions given in (3.13) and (3.14) both possess an open-loop zero at $s = 0$, hence both systems are natural "differentiators" up to a certain frequency. This can also be observed in the FRF given in Fig. 3.4. Hence, the integral part of the controller will effectively become a proportional controller. With high-enough K_I one can obtain the closed-loop frequency response performance shown in Fig. 3.5. In this figure, both the open-loop (including the controller) and closed-loop FRFs are given. In the open-loop FRFs it is seen that there are ∞ gain and phase margins for both systems although there is a collapse (due to resonance followed by an anti-resonance) in the phase for the MCL case. In the closed-loop FRFs it is seen that, although the open-loop responses seem quite different, high open-loop gain suppresses this difference and makes the closed loop FRFs close to 1. Therefore, as a conclusion of the analysis one may state that with high-enough integral gain the current control performance for MCL and MO cases are indeed very similar.

3.1.4 Performance Obtained with a Real System

In the previous sub-section of the thesis, a simplified model is utilised to show that although open-loop system FRFs for MCL and MO cases are quite different, one can make both systems behave as unity gain closed loop systems for a high-enough frequency range by using a high K_I value in the controller. In this sub-section, the practical issues will be investigated to see if there are any differences between the theoretical findings and actual system.

Open-loop frequency response tests have been performed with the experimental motion control test bed platform. The parameters of this platform are given in Table 3.1. The experimental open-loop response for the MO case is given in Fig. 3.6. If one compares the FRF given in this figure, with the one obtained from analysis (see Fig. 3.4) the following differences can be observed:

- Although the magnitude of the FRF follows a similar pattern with respect to frequency, the resonance is smoother, meaning that there exists further damping

in the real system, which is possibly due to unmodeled rotor bearing friction.

- Phase of the FRF behaves differently than expected, and it is tending to be zero at very low frequencies. This means that the system actually has more damping terms than modeled making phase not equal to 90° as frequency is lowered. Moreover, due to fact that the resonance is smoother, the phase starts to decrease at a lower frequency, before the resonance peak.
- Phase of the FRF at high frequencies does not converge to the expected theoretical value. This fact indicates that there should be a transport delay term (with a transfer function $e^{-T_d s}$) causing more phase lag as the frequency is increased.

The experimental open-loop response for the MCL case is given in Fig. 3.7. If one compares the FRF given in this figure, with the one obtained from theoretical analysis (see Fig. 3.5) the following differences can be observed:

- Although the magnitude of the FRF follows a similar pattern with respect to frequency, both resonance peaks are smoother, meaning that there exists further damping in the real system, which is possibly due to unmodeled load and rotor bearing frictions.
- Phase of the FRF at high frequencies does not converge to a final value as expected from the analysis. This fact indicates that there is a transport delay term (with a transfer function $e^{-T_d s}$) injecting more phase lag as the frequency is increased.

The experimental closed loop responses for MO and MCL cases are given in Fig. 3.8 and Fig. 3.9, respectively. If one compares the magnitude plots given in these figures, it is seen that high integral gain suppresses the differences in the open-loop responses (though the resonances and anti-resonance of MCL case are still seen in the response, their magnitudes are quite small and phase jumps are eliminated). However, there is significant difference between expected and measured phase responses. As seen in Fig. 3.5 expected closed-loop phase lags are about 6° even at a frequency of 1 kHz; however in the experiments it is seen that phase lag becomes about 80° even at 200 Hz for the MCL case. In order to find the reason for this difference a linear phase graph

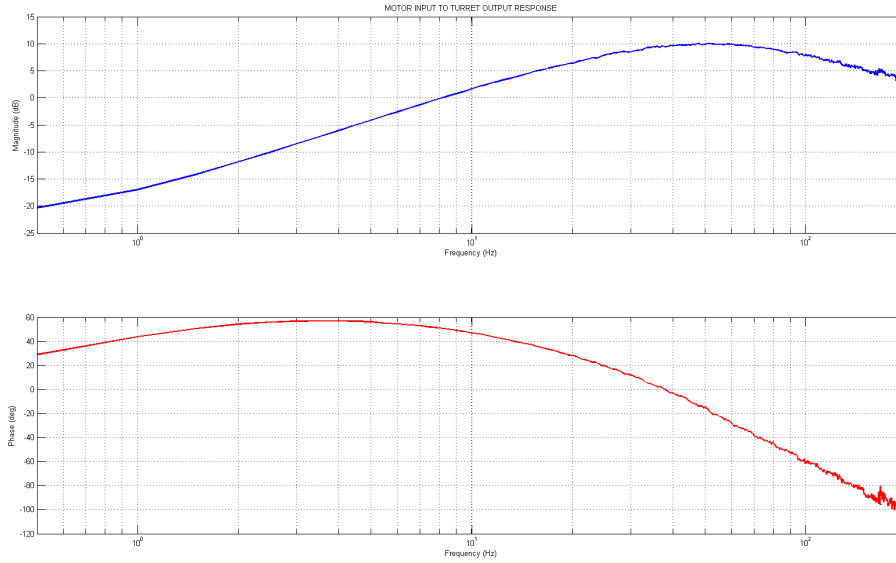


Figure 3.6: Experimentally Obtained Open Loop System FRF for MO case.

for the open loop motor only case is given in Fig. 9. in which the trend of phase difference between measured and expected phases is plotted. This phase scheme is very similar to the phase scheme of a transport delay which has a phase of

$$\theta = -T_d 2\pi f \quad (3.19)$$

where T_d represents the time delay in seconds. If one uses origin and a point from Fig. 3.10 ($f = 66.5 Hz$ and $\theta = -35.2^\circ = -0.614 rad$), we can find the delay amount as

$$T_d = -\frac{-0.614}{2\pi 66.5} = 1.5ms \quad (3.20)$$

This very little amount of delay causes the closed loop current bandwidth of the system to degrade significantly. Hence, it is an important point to find the causes of this delay and try to compensate them whenever possible (via optimizing the hardware and/or software design -e.g. employing a higher sampling rate, or using a faster communication means between the sensor and the controller hardware).

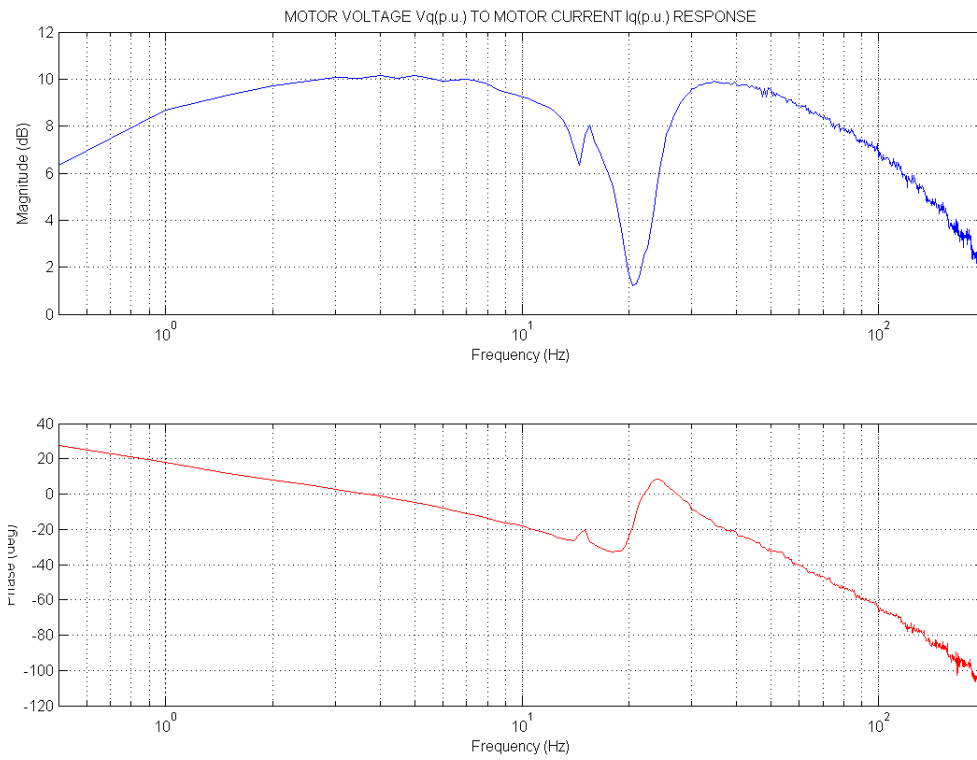


Figure 3.7: Experimentally Obtained Open Loop System FRF for MCL case.

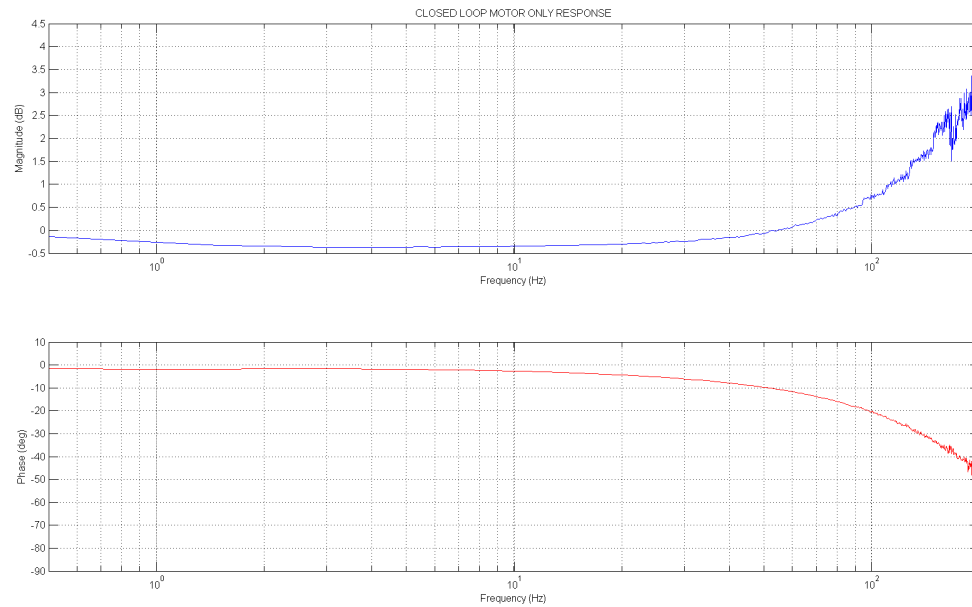


Figure 3.8: Experimentally Obtained Closed Loop System FRF for MO case.

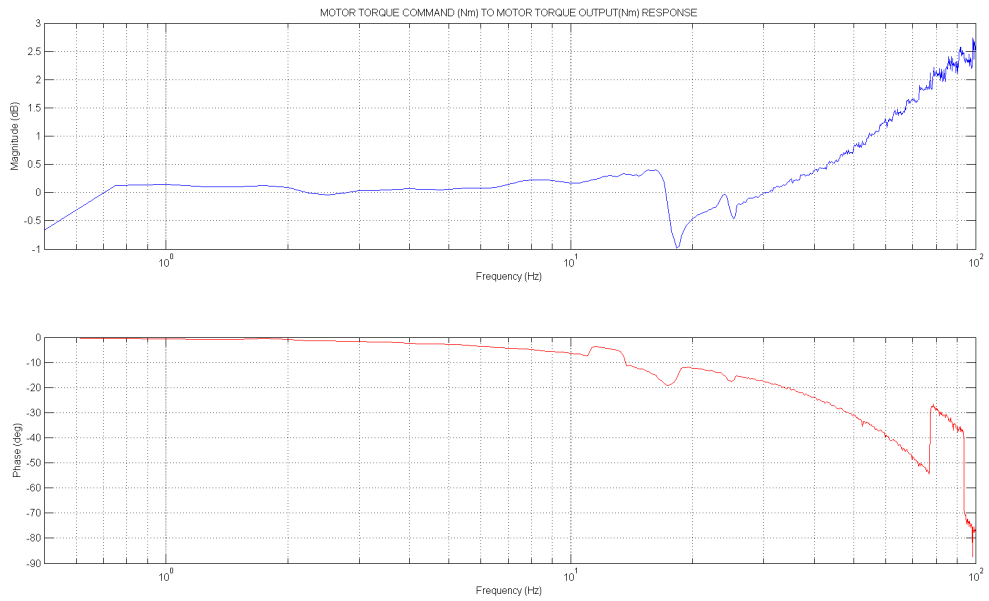


Figure 3.9: Experimentally Obtained Closed Loop System FRF for MCL case.

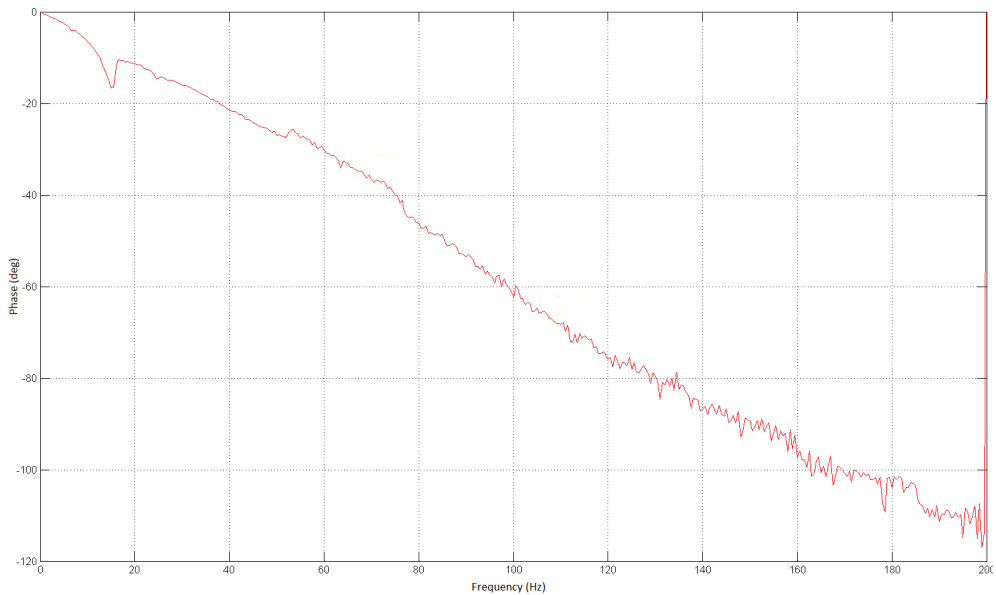


Figure 3.10: Phase difference between theoretical and experimental MO FRF findings.(Note the linear trend indicating transport delay).

3.1.5 Section Summary - Contributions

The aim of this part of the study was to explore the interactions between mechanical and electrical components of a motion platform. During the study both theoretical and experimental results are obtained and compared with each other. During theoretical calculations it was seen that when the motor is coupled to a load its open-loop transfer function from motor voltage to motor current is affected and FRF changes significantly. On the other hand, it was also shown that for a practical system (with high enough damping terms, i.e. electrical resistance and mechanical viscosity) this change can be suppressed via high enough integral control term while applying terminal voltage using motor current feedback during close-loop control. In this condition, the closed-loop motor current performance practically does not depend on whether the motor shaft is free to rotate or it is coupled to a mechanical load. This theoretical findings were observed during the experimental phase of the study as well. However, it was also observed that transport delays (mostly due to discrete-time control and digital communications) affect the phase of the FRFs significantly, causing small gain margins and preventing an increase in integral gain and degrading the closed-loop performance of the current controller significantly. This transport delay is usually the dominant factor in determining the bandwidth of the closed-loop current control and should be minimized with careful hardware and/or software design.

To summarize this section: In motion platforms, the electrical motor dynamics and the mechanical system dynamics do interact. In the forward direction (i.e. from electric current to mechanical speed), the bandwidth of the electrical sub-system is much higher than that of the mechanical sub-system, hence its dynamics can be neglected. In the backward direction (i.e. from mechanical speed to electrical current), the effects of the mechanical sub-system on the electrical one can be compensated with high enough control gains, if one can keep the overall transport delay less than a reasonable value. Although studies performed until now have made this assumption, it was modeled and verified on the real system, before utilisation. It was confirmed that with a high enough integral gain and low enough transport delay, the current loop can be assumed to have a transfer function of 1, for the range of frequencies for which the mechanical part of the system can respond.

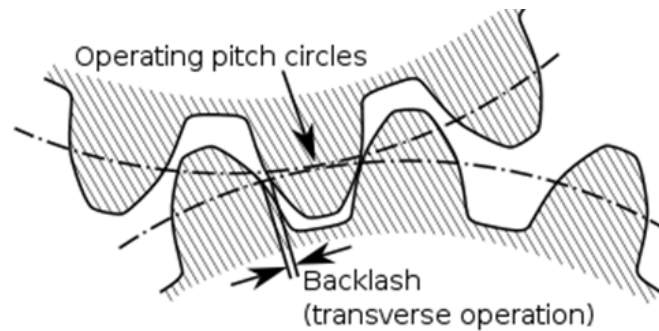


Figure 3.11: Backlash phenomenon between two paired gears schematized.

3.2 Non-linear Effects in The Motion Transmission Part

A frequent problem encountered in the speed control of motion platforms is the disturbance created by the components in relative motion. This problem is due to two physical phenomenons: Backlash (gear play) and friction. In this part of the thesis, the models of these phenomenons were briefly reviewed and the identification studies performed on the system regarding the friction and backlash parameters of the real system were reported.

3.2.1 BACKLASH

Backlash -also termed as "gear play"- is a common non-linear phenomenon in mechanical systems (see Fig. 3.11). It may be termed as the loss of motion caused by the clearance between pairing gears. Although backlash causes a non-linear behavior, undesirable for control design, it is unavoidable and even necessary for reliable operation of gear pairs. In high performance motion platforms, some sort of mechanical precautions are taken to reduce (practically prevent) backlash. As given in [87], the two most popular methods are utilization of an anti-backlash pinion and usage of a anti-backlash gear assembly.

In the anti-backlash pinion solution, two gears of the same type are placed on top of each other and pre-loaded against each other to provide direct contact even if the paired gear starts to move in either direction (see Fig. 3.12). This type of anti-backlash solution is usually practical for low-torque systems.

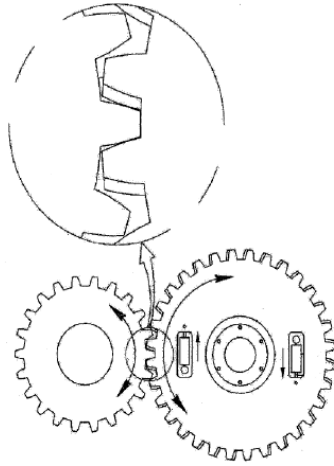


Figure 3.12: Utilization of anti-backlash pinion to avoid backlash. Note that, the drawing is two-dimensional and there are two different gears on top of each other on the right-hand side gear; pre-loaded with small springs. [87]

For systems with higher torque specifications the driving gear is directly pre-loaded against the driven gear. This may be achieved either by applying a direct pre-loading force or using extra idler gears to prevent backlash (see Fig. 3.13 for an illustration and example). In the experimental system utilized during this study, the second method is employed for preventing backlash.

3.2.1.1 Backlash Modeling

Depending on the mechanical surrounding of the backlash and operating conditions, different models must be utilized to model the behavior of the systems with backlash ([52]). There are several models ranging from the simple kinematic "dead-zone model" to "physical model" which deals with the stiffness and damping terms during the system is in backlash zone. There are even models with varying backlash for uneven structures similar to ring gears with hundreds of teeth [87]. The simplest model for the backlash behavior is the dead-zone model, which is a static, non-linear function used to represent backlash, as given below.

The Dead-Zone Model [40]: The schematic representing the model used for backlash is given in Fig. 3.14. If one neglects the shaft damping (i.e. assume $c_s = 0$), shaft torque is proportional to the shaft twist, θ_s and hence

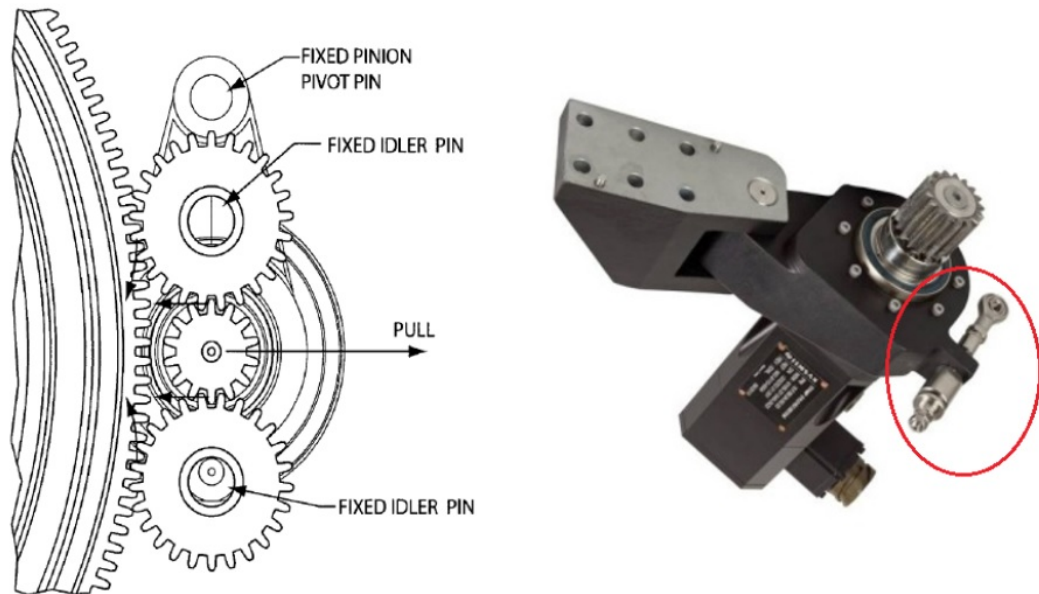


Figure 3.13: A typical example of a pre-loaded anti-backlash gear assembly with idler gears schematic (left), and an example of a direct pre-load mechanism (right - inside the red ellipse). [87]

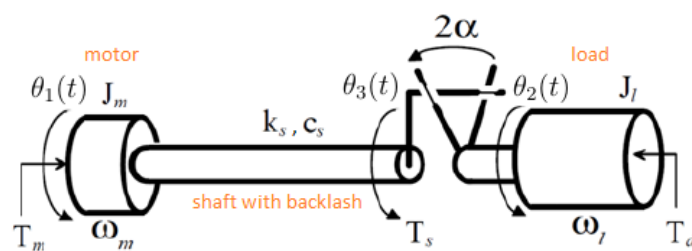


Figure 3.14: Schematic showing the backlash phenomenon in a two-mass system, where torque from a motor is transferred to a load via a shaft with a backlash angle of α . (refer to Table 3.2 for the list of parameters given in the figure)

Table 3.2: Parameter Definitions for the Backlash Model Schematic of Fig. 3.14

Parameter	Definition
$\theta_1(t)$	Angle of the motor
$\theta_2(t)$	Angle of the load
$\theta_3(t)$	Angle of the driving axis at the backlash
$\theta_d(t) = \theta_1(t) - \theta_2(t)$	Displacement
$\theta_s(t) = \theta_1(t) - \theta_3(t)$	Shaft twist
$\theta_b(t) = \theta_3(t) - \theta_2(t)$	Backlash angle
α	Backlash angle is $[-\alpha, \alpha]$
J_m	Motor inertia
ω_m	Motor speed
k_s	Shaft stiffness coefficient
c_s	Shaft damping coefficient
J_l	Load inertia
ω_l	Load speed
T_d	Load disturbance torque input
T_m	Motor torque input
T_s	Shaft torque developed

$$T_s = k_s \theta_s \quad (3.21)$$

When there is backlash and no shaft damping (i.e. $c_s = 0$), shaft twist θ_s is given by the following dead-zone function (see Fig. 3.15)

$$\theta_s = D_\alpha(\theta_d) = \begin{cases} \theta_d - \alpha, & \text{if } \theta_d > \alpha \\ 0, & \text{if } |\theta_d| \leq \alpha \\ \theta_d + \alpha, & \text{if } \theta_d < -\alpha \end{cases} \quad (3.22)$$

hence we get

$$T_s = k_s \theta_s = k_s D_\alpha(\theta_d) \quad (3.23)$$

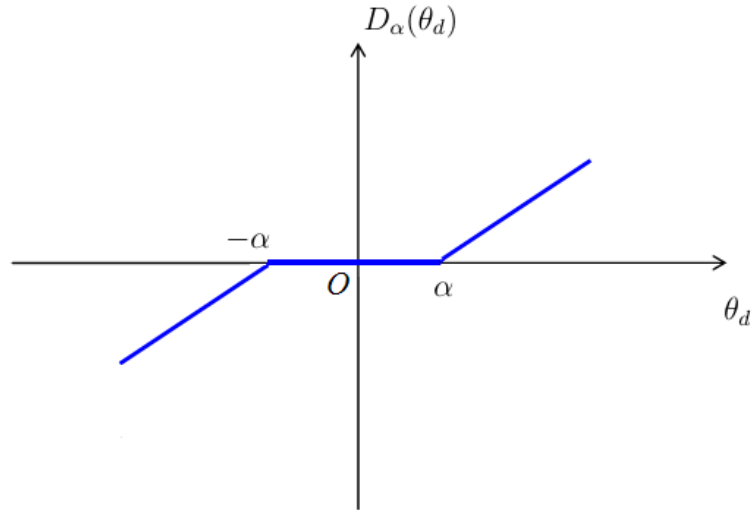


Figure 3.15: Non-linear dead-zone function used for modeling the backlash behavior.

In the literature, very precise models are proposed and tested for the identification and estimation of backlash behaviour. However, it was stated that explicitly estimating backlash behavior is usually non-robust and black-box models should be preferred if the main focus is the speed control of the load [87]. Moreover, in high performance military systems, gearboxes are very low-backlash (≤ 1 arcmin typically) and mechanical backlash compensation is utilized. In this study the concern is not the dynamics of the backlash, nor precisely modeling the system. The main purpose is to investigate the effect of backlash on the system behaviour, and if possible derive a suitable mathematical expression which can be used in our simulation models for the controller development. Hence only the dead-zone backlash model is provided here. Readers concerned with the detailed modeling of backlash and backlash compensation may refer to M.Sc. thesis of Yumrukcal ([87]), and the comprehensive survey of Nordin on backlash modeling and compensation ([52]).

3.2.1.2 Measuring Backlash Experimentally

There are several methods to measure the backlash amount in a system. “The indirect dynamic backlash identification” described in [41] is utilized in this study. The procedure and the idea of this technique is as follows:

- Move the motor shaft in one direction (which may be referred as the negative

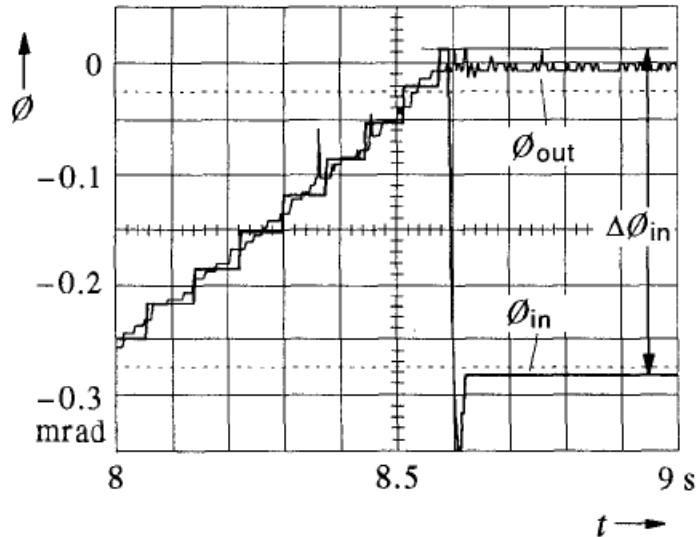


Figure 3.16: Figure illustrating the identification of backlash via indirect dynamic identification approach.

direction without loss of generality) to engage the gears and then stop the system,

- At the given position start applying small torque pulses to the motor shaft in the positive direction so that the motor shaft moves inside the backlash (of course duration and amplitude of the pulses should be tuned experimentally),
- When the motor shaft displacement in positive direction equals the backlash angle the load engages to the motor, increasing the total inertia "seen" by the motor dramatically,
- After the point of engagement, the displacements in the motor shaft with same torque pulses must be much more less than the displacements before,
- The total amount that the motor shaft displaced during the torque pulses applied in the positive direction gives -approximately- the amount of backlash in the system.

Illustration of the idea of "indirect dynamic backlash identification" is given in Fig. 3.16.

After utilising the hinge mechanism to reduce the overall backlash, the above identification procedure has been applied. The data obtained during these tests are given

in Fig. 3.17. Test results are summarized in Table 3.3, showing that one can obtain a backlash angle as low as 0.042° in the system, on the motor side, which makes around 0.00019° on the load side. Actually, this backlash amount can easily be neglected, however the identified value is employed during the simulations for the sake of completeness (despite no effect on the controller performance).

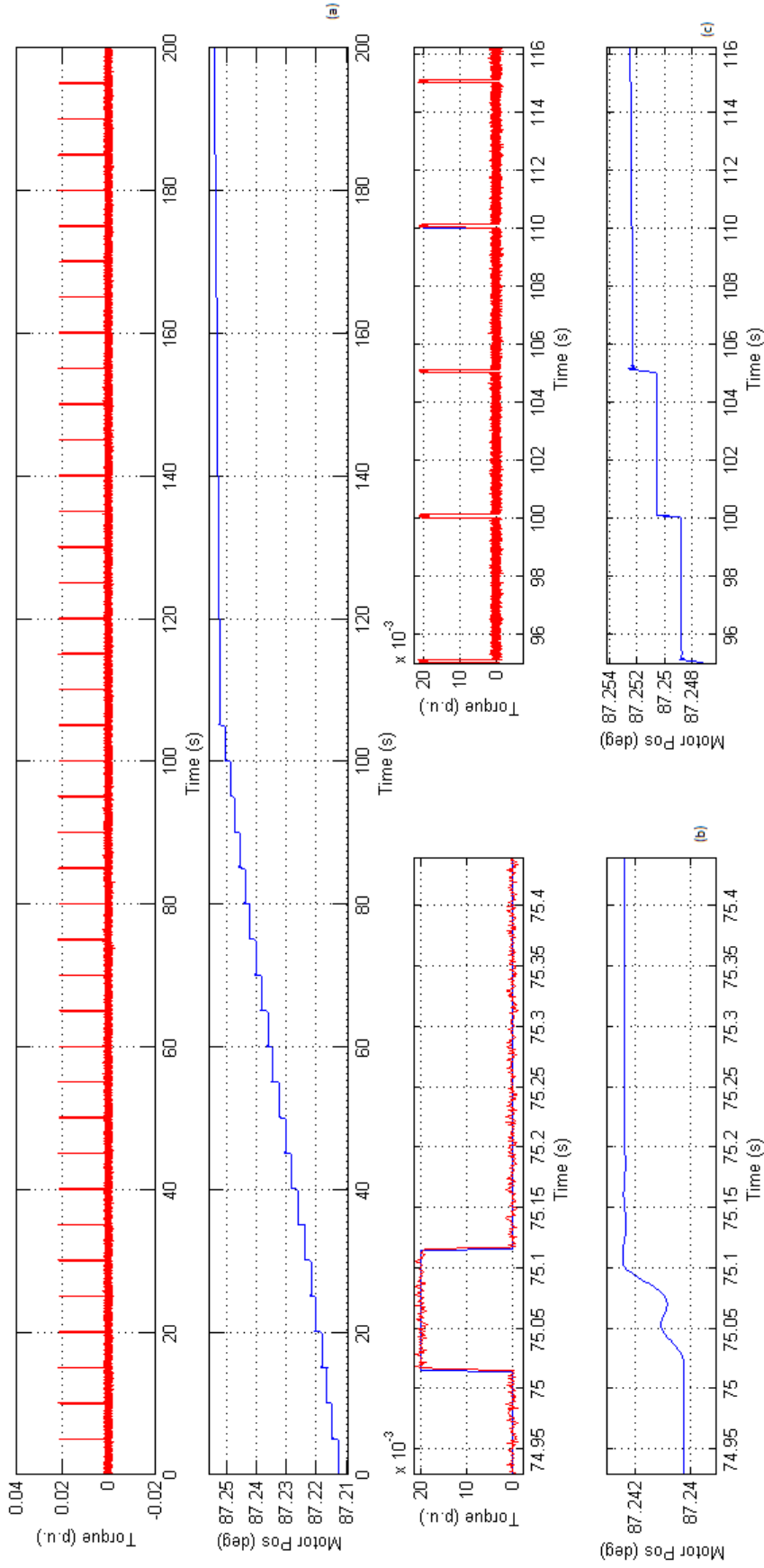


Figure 3.17: Sample backlash measurement experiment with the system under study. (a) Overall experiment data; (b) A typical motor position jump inside the backlash region, during a torque pulse; (c) Change in the behavior of the system at the end of backlash region.

3.2.2 FRICTION

Friction is present in every mechanical system in which the moving parts are in contact. There are several studies on friction including models of this physical phenomena. However, there exist no efficient analytic methods to describe friction and the introduced complex, non-linear friction models with un-measurable internal states and time-varying parameters can only be applied for practical friction compensation problems with difficulty. As a very complex physical phenomenon, friction is a sub-problem of tribology, as indicated in our colleague Sincar's M.Sc. thesis [86] "Besides the field of tribology, there are several other domains where friction plays a crucial role since most engineering mechanisms are composed of a certain number of interfaces between the machine parts. Some of these domains are control, geomechanics, structural dynamics and design and life-cycle engineering. Each of these fields approaches friction in a different manner since the required degree of complexity of friction models changes within these fields. In cases where frictional effects to the system performance are small, the friction models are considered in simple form". According to this statement, if possible, the simplest friction model (Coulomb friction model) should be utilised in modelling a system. Actually, since the aim of this study is developing a controller independent of the system uncertainties, the controller should have no explicit information regarding the friction model. Moreover, the friction would already change behaviour, since it depends on, [86]:

- Real contact area,
- Normal force on the body,
- Relative motion between contacting bodies,
- Local temperature at the contact points,
- Wear of material,
- Stiffness of the contacting surfaces,
- Adhesion of the contacting surfaces,
- Lubricant

Table 3.3: Experimentally obtained backlash angles for the system under study (motor side).

DIRECTION	BACKLASH
Negative-Exp.-1	0.041°
Negative-Exp.-2	0.044°
Negative-Exp.-3	0.047°
Negative-Exp.-4	0.038°
Negative-Average	0.043°
Positive-Exp.-1	0.038°
Positive-Exp.-2	0.042°
Positive-Exp.-3	0.044°
Positive-Exp.-4	0.041°
Positive-Average	0.041°

- Welding of the contacting points
- History of the friction contact
- Surface geometry,
- Elastic and plastic deformation
- Dynamic friction forces on the bodies

In summary, friction is a very complex physical phenomenon whose physics is beyond the scope of this thesis. In this study, the simplest friction model is utilized during simulations and modeling. This model is the very well known "Coulomb Friction Model".

3.2.2.1 Coulomb Friction Model

Coulomb friction model -assuming the body at rest- defines the friction force between contacting bodies as

$$T_f = \begin{cases} T_a, & \text{if } T_a < |T_s| \\ T_s \times \text{sgn}(T_a), & \text{if } T_a \geq T_s \end{cases} \quad (3.24)$$

Where T_s is the pre-specified friction torque and T_a is the externally applied torque. Due to its simplicity, Coulomb friction model is frequently used. It can be further improved by adding viscous friction, however this is not critical for the purposes of this study, as the main motivation is to keep the friction as a black-box behaviour. In the next sub-section the experimental results on friction measurement are provided.

3.2.2.2 Experimental Results on Friction

The method utilized for friction measurement is simply moving the system with constant speed at different directions and observe the required torque levels. Notice that

$$T_a = \alpha \times J_s + T_f \quad (3.25)$$

where T_a is the torque applied to the system; α is the angular acceleration of the system; J_s is the equivalent system inertia; and, T_f is the constant friction torque. During motion with constant speed, the angular acceleration is zero, i.e.:

$$\alpha = 0 \quad (3.26)$$

yielding

$$T_a = T_f \quad (3.27)$$

The torque data has been collected for a small speed (3 deg/s in each direction) of the system to see the level of static friction. Moreover the very same experiment was performed with a speed of 30 deg/s in order to see the viscosity effects.

As seen in Fig. 3.18 the friction at opposing directions has very similar characteristics and viscosity effects seem to be negligible (a 10–15% increase with a speed increased

10 times). The average static friction torque values evaluated for opposing directions are listed in Table 3.4. As seen in this table, they are very similar and around 4% of the maximum torque.

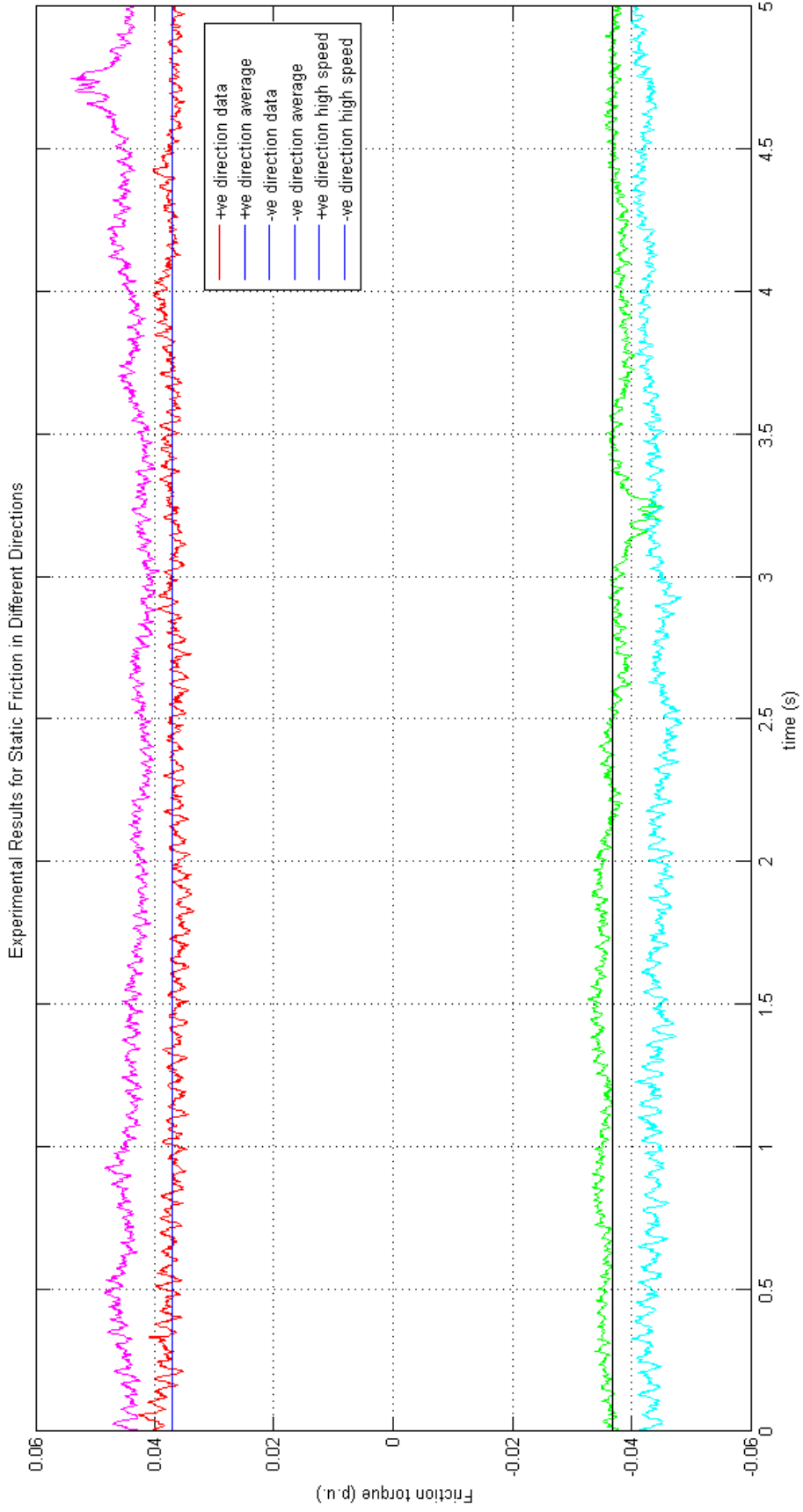


Figure 3.18: The experimentally measured static friction. Positive direction friction data (red), its average (blue). Negative direction friction data (green), its average (black). The high speed friction plots are given as a reference for modeling error by ignoring viscous behavior.

Table 3.4: Experimentally obtained static friction values.

DIRECTION	STATIC FRICTION
Negative	-0.0368 p.u.
Positive	0.0370 p.u.

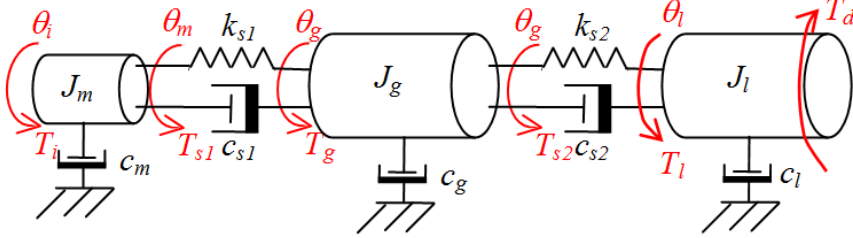


Figure 3.19: Schematic representation of the linear three-mass mechanical system model.

3.3 Distributed Inertia Model for The Mechanical Components

In the control of motion platforms, lumped-mass models are employed for describing the behavior of the mechanical part of the system. These models usually include two (e.g. [45],[68] [74]) or three (e.g.: [46],[79]) lumped masses connected with flexible elements. For a typical motion platform in a military system, usually the actuator is situated at "one end" and the load is located at "the other end" of the system; whereas the feedback sensor is usually situated in between. Hence, it is wise to employ a three-mass model to represent two "end" masses and one "in between" mass.

The schematic of a typical model for a three-mass system connected with flexible elements is shown in Fig. 3.19. The parameters used in this figure are summarized in Table 3.5.

3.3.1 Analysis in s-domain

One can easily derive a linear MIMO model for such a system by writing down the equations of motion for each body as:

$$J_m \dot{\omega}_m = T_m - T_{s1} - c_m \omega_m \quad (3.28)$$

Table 3.5: Parameters of the model given in Fig. 3.19

PARAMETER	UNIT	REMARKS	SAMPLE VALUE
T_m	Nm	Motor Torque (controlled input)	-
T_d	Nm	Equivalent Disturbance Torque (uncontrolled input)	-
θ_m	rad	Position of the Motor Shaft	-
θ_g	rad	Position of the Second Mass	-
θ_l	rad	Position of the Third Mass	-
c_m	Nm.s/rad	Viscosity of the Motor Shaft Bearing	100
c_g	Nm.s/rad	Viscosity of the Second Mass Bearing	100
c_l	Nm.s/rad	Viscosity of the Third Mass Bearing	100
c_{s1}	Nm.s/rad	Equivalent Viscosity of the First Joint	0
c_{s2}	Nm.s/rad	Equivalent Viscosity of the Second Joint	0
k_{s1}	Nm/rad	Equivalent Stiffness of the First Joint	1.8×10^5
k_{s2}	Nm/rad	Equivalent Stiffness of the Second Joint	1.8×10^5
J_m	kgm^2	Equivalent Inertia of the First Mass	30
J_g	kgm^2	Equivalent Inertia of the Second Mass	100
J_l	kgm^2	Equivalent Inertia of the Third Mass	300

$$J_g \dot{\omega}_g = T_{s1} - T_{s2} - c_g \omega_g \quad (3.29)$$

$$J_l \dot{\omega}_l = T_{s2} - T_d - c_l \omega_l \quad (3.30)$$

where

$$T_{s1} = k_{s1}(\theta_m - \theta_g) + c_{s1}(\omega_m - \omega_g) \quad (3.31)$$

$$T_{s2} = k_{s2}(\theta_g - \theta_l) + c_{s2}(\omega_g - \omega_l) \quad (3.32)$$

If one substitutes (3.31) and (3.32) into (3.28)-(3.30), takes the Laplace transforms of the resulting equations, and finally solves for inertia speeds in terms of input torques (being the motor and disturbance torques), one gets the following MIMO transfer function model:

$$\begin{bmatrix} \Omega_m(s) \\ \Omega_g(s) \\ \Omega_l(s) \end{bmatrix} = \frac{s}{\Delta} \begin{bmatrix} (D^2 - CE) & BD \\ -BE & AD \\ -BD & (AC - B^2) \end{bmatrix} \begin{bmatrix} T_m(s) \\ T_d(s) \end{bmatrix} \quad (3.33)$$

with

$$A = J_m s^2 + (c_m + c_{s1})s + k_{s1} \quad (3.34)$$

$$B = c_{s1}s + k_{s1} \quad (3.35)$$

$$C = J_g s^2 + (c_g + c_{s1} + c_{s2})s + k_{s1} + k_{s2} \quad (3.36)$$

$$D = c_{s2}s + k_{s2} \quad (3.37)$$

$$E = J_l s^2 + (c_l + c_{s2})s + k_{s2} \quad (3.38)$$

$$\Delta = B^2 E + AD^2 - ACE \quad (3.39)$$

in the above equations $\Omega_m(s)$, $\Omega_g(s)$ and $\Omega_l(s)$ represent the Laplace transforms of $\omega_m(t)$, $\omega_g(t)$ and $\omega_l(t)$, respectively.

3.3.2 An Investigation of Frequency-domain Behavior for Second Mass Speed Output

In most of the previous studies the main concern had been usually control of the motor speed ω_m ([27],[45] etc.) or the control of the load speed ω_l ([49],[67] etc.). However, in most of the military motion platforms the sensor used for the angular speed feedback to the controller is placed in between the motor (or actuator) and the

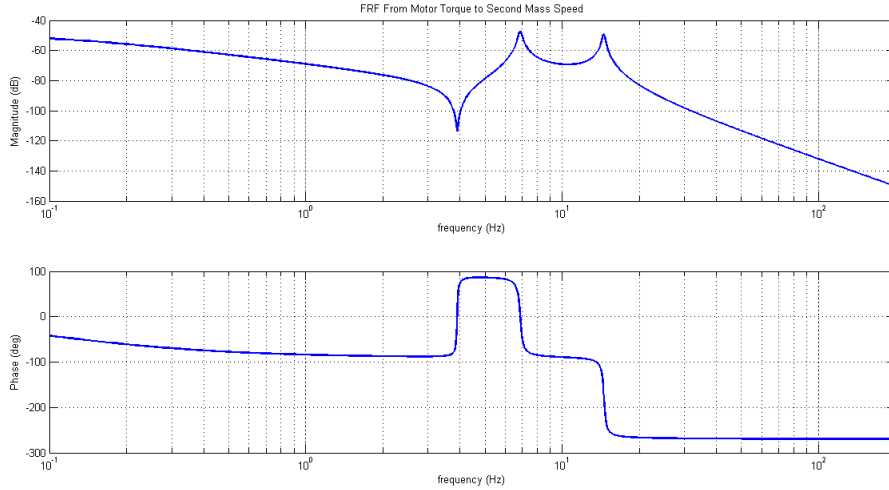


Figure 3.20: Typical Frequency Response Function (FRF) plot for the second mass speed output of a 3 mass system.

load; meaning the most appropriate feedback is the second mass speed, ω_g . One may argue that, the "load speed" should be critical; however during the mechanical design it is guaranteed that if one controls the "feedback sensor speed", the motion platform speed control requirement is satisfied. Hence, it is worth investigating the frequency domain characteristics of this additional speed element.

Taking the second mass speed as the output, if one investigates the frequency response function

$$G_{gm}(j\omega) = \frac{\Omega_g(j\omega)}{T_m(j\omega)} \quad (3.40)$$

it is obvious that the behaviour is dependent on the values of the system parameters given in Table 3.5. The mechanical modes of the system are functions of stiffness and inertia values, while mode damping values are highly dependent on viscosity terms. For a typical motion platform (i.e. with $J_l \gg J_m$ and $k_{s2} \approx k_{s1}$) the frequency response function defined in (3.40) is similar to the one given in Fig. 3.20. If one investigates this figure, it is easily seen that there is an anti-resonance at a lower frequency than resonances. In order to deal with this anti-resonance, the controller must have a very high gain at least in the close neighborhood of this frequency. On the other hand, in order to have a large enough gain margin, the open-loop FRF must be far less than 0 dB whenever the phase lag is -180° . Hence the controller

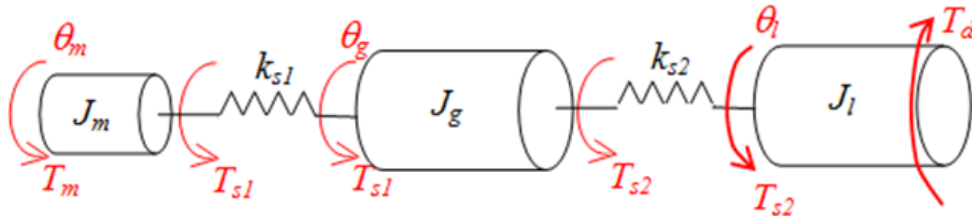


Figure 3.21: Simplified system model with all damping terms neglected.

must suppress the resonances shown in Fig. 3.20. Finally, in order not to have a spillover effect, which may be defined as the instability caused by higher frequency modes which are not modeled, the controller must suppress the high frequency content. In order to achieve such a performance several notch or bi-quad filter designs are proposed ([48]). Moreover the anti-resonance effect can simply be dealt with poles placement ([49],[62]) by employing the method of Truxal and Guillemin. However, it is very well known that, without using additional sensors (not practical for our case) and taking precautions for avoiding instability, these methods are simply not robust and pose un-damped oscillations in a practical system. Hence, one needs a control architecture that provides high gain in the vicinity of the anti-resonance frequency; suppresses the response about the resonance frequencies and adapts itself accordingly for the case these critical frequencies somehow shift during operation.

3.3.3 Effects of System Parameters on Dynamic Behaviour

In this sub-section, the mechanical model used for the system is investigated by performing a parametric analysis. This analysis is used to enlighten the effects of system parameters on the open-loop system behaviour, i.e. on the pole and zero locations of the plant.

For the sake of simplicity, the simplified system model given in Fig. 3.21 is utilised for mathematical analysis. In other words, the friction terms are neglected in the transfer function equation. For this model, the transfer function from motor torque to second inertia angular speed output can easily be evaluated as

$$\frac{\Omega_g}{T_m} = \frac{k_{s1}(J_l s^2 + k_{s2})}{s J_m [J_g J_l s^4 + J_g J_l k_{s1} s^3 + (k_{s2}(J_l + J_g) + k_{s1} J_l) s^2 + k_{s1} k_{s2} (J_l + J_g) s + k_{s1} k_{s2}]} \quad (3.41)$$

This open-loop transfer function has two zeros and four poles whose values depend on system parameters. There is an additional pole at the origin due to torque input to speed output transition.

The change of pole and zero locations as parameters change can be investigated using the following definitions

$$S_{Z_{ij}} \triangleq \frac{\partial z_i}{\partial a_j}, S_{P_{kj}} \triangleq \frac{\partial p_k}{\partial a_j} \quad (3.42)$$

Where z_i represents i^{th} zero, p_k represents k^{th} pole, a_j represents j^{th} parameter, $S_{Z_{ij}}$ represents "sensitivity measure of i^{th} zero to j^{th} parameter" and $S_{P_{kj}}$ represents "sensitivity measure of the k^{th} pole to j^{th} parameter". Although it is straightforward to evaluate pole and zero locations by finding numerator and denominator polynomial roots, performing these operations analytically on paper is very cumbersome. Hence, the sensitivity measure evaluation was performed using Symbolic Math Toolbox of MATLAB. With the parameter vector

$$a \triangleq [J_m \quad J_g \quad J_l \quad k_{s1} \quad k_{s2}] \quad (3.43)$$

One gets the following sensitivity measure values with the sample system parameters

$$S_Z = \begin{bmatrix} 0 & 0 & -j0.0408 & 0 & j6.8x10^{-5} \\ 0 & 0 & j0.0408 & 0 & -j6.8x10^{-5} \end{bmatrix} \quad (3.44)$$

$$S_P = \begin{bmatrix} 0 & 0 & 0 & 0 & 0 \\ 0 & -j1.71x10^{-1} & -1.78x10^{-15} - j9.16x10^{-4} & 1.26x10^{-8} + j2.31x10^{-4} & -1.34x10^{-8} + j2.15x10^{-5} \\ 0 & j1.71x10^{-1} & -1.78x10^{-15} + j9.16x10^{-4} & 1.26x10^{-8} - j2.31x10^{-4} & -1.34x10^{-8} - j2.15x10^{-5} \\ 0 & -j2.03x10^{-1} & -j2.12x10^{-2} & -1.26x10^{-8} + j9.72x10^{-6} & 1.34x10^{-8} + j1.09x10^{-4} \\ 0 & j2.03x10^{-1} & j2.12x10^{-2} & -1.26x10^{-8} - j9.72x10^{-6} & 1.34x10^{-8} - j1.09x10^{-4} \end{bmatrix} \quad (3.45)$$

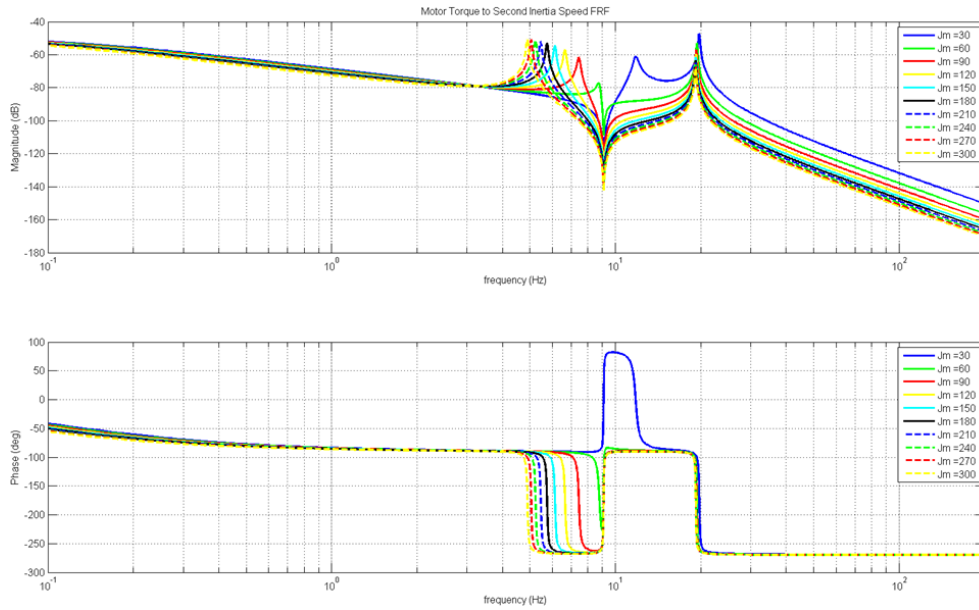


Figure 3.22: Torque input to second mass speed output FRF change w.r.t. first mass inertia, J_m .

As seen in (3.44), the anti-resonance frequency value, which corresponds to the system zeros is dependent on load inertia and second shaft stiffness values. In order to visualize the sensitivity of the open-loop plant behavior w.r.t. system parameters, the FRF plots for the open-loop plant as system parameters change are shown in Figs. 3.22,3.23,3.24,3.25,3.26. From these plots and above analysis it is straightforward to say that if the mechanical system had a higher k_{s2} or lower J_l value, then it would be possible to obtain a better performance for the speed control of the second mass without much design effort [83]. This is due to fact that the first anti-resonance frequency is shifted towards higher values with these parameter changes. Especially increasing k_{s2} shifts all critical frequencies (anti-resonance and resonance) to higher values.

3.3.4 Controllability and Observability Analysis

In this study, the aim is controlling the speed of the second mass. The feedbacks are the motor (first) mass and second mass speed signals, the only manipulating variable is the motor torque. In order to be able to comment on the extents of the linear control, one needs to analyse both controllability and observability of the system. This is because controllability is a measure relating control actions to desired states

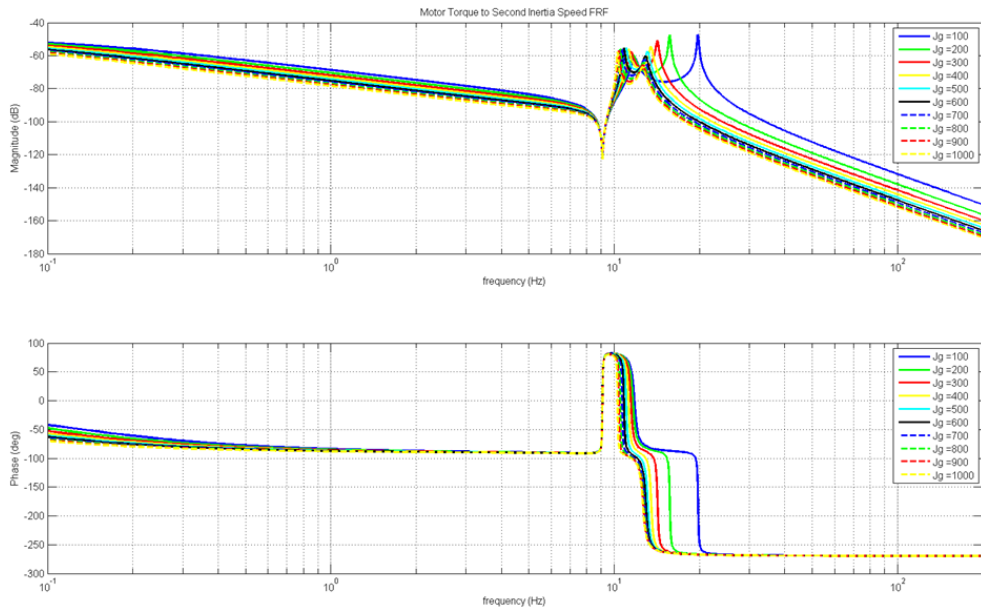


Figure 3.23: Torque input to second mass speed output FRF change w.r.t. second mass inertia, J_g .

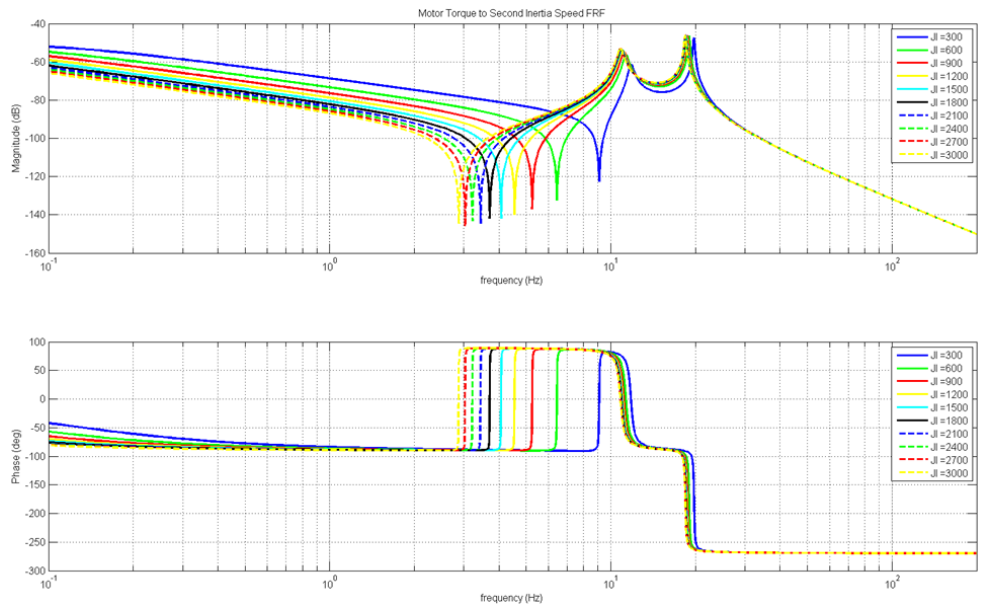


Figure 3.24: Torque input to second mass speed output FRF change w.r.t. third mass inertia, J_t .

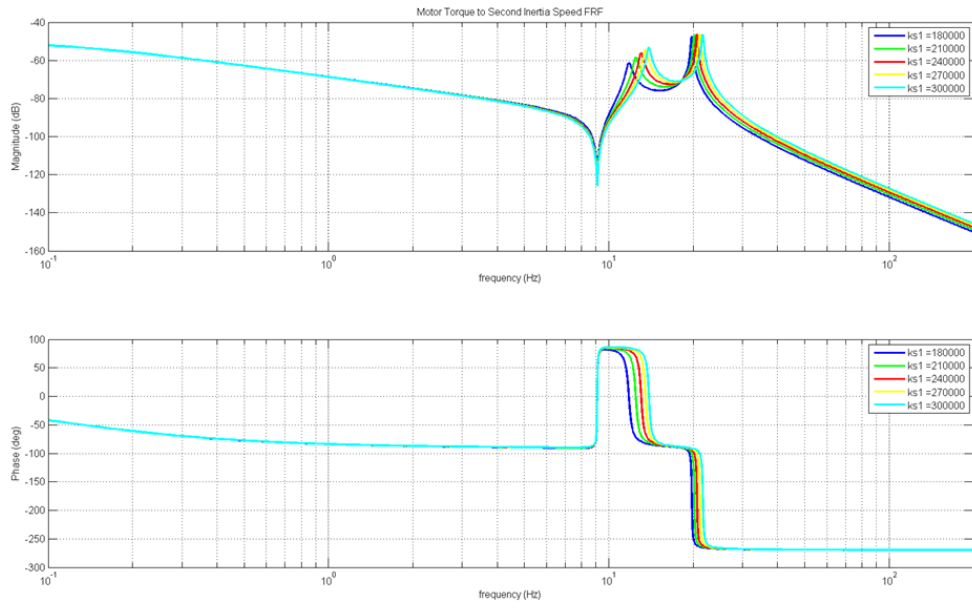


Figure 3.25: Torque input to second mass speed output FRF change w.r.t. first shaft stiffness, k_{s1} .

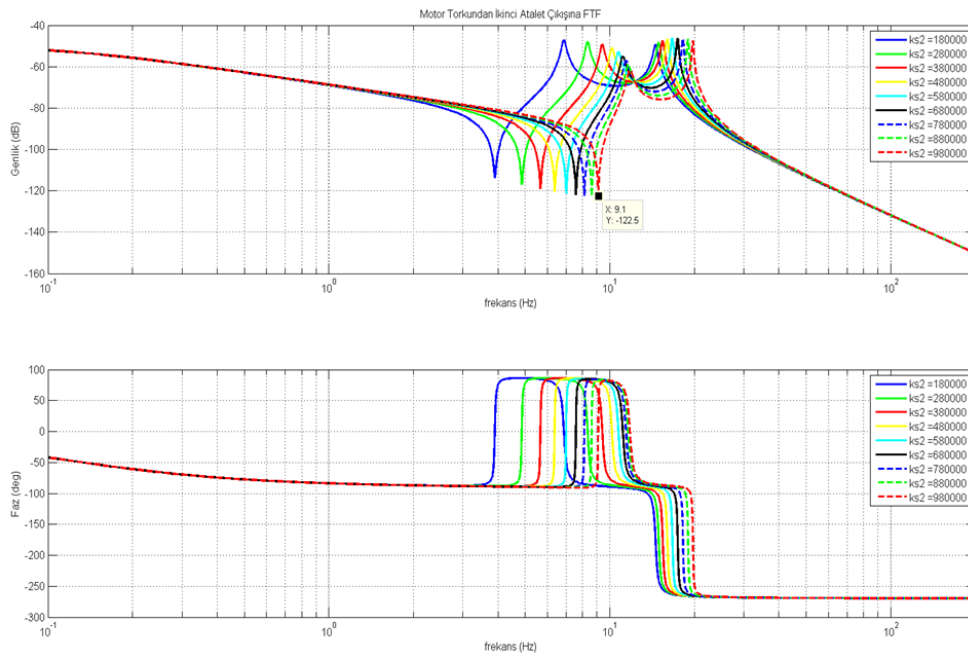


Figure 3.26: Torque input to second mass speed output FRF change w.r.t. second shaft stiffness, k_{s2} .

while observability is a measure relating measured outputs to internal states of the plant.

In order to analyse controllability and observability we should find the controllability and observability Grammians of our system, which are given by

$$Q_C = \begin{bmatrix} B & AB & A^2B & A^3B & \dots & A^{n-1}B \end{bmatrix} \quad (3.46)$$

$$Q_O = \begin{bmatrix} C \\ CA \\ CA^2 \\ CA^3 \\ \dots \\ CA^{n-1} \end{bmatrix} \quad (3.47)$$

for a linear system described by the following state-space model,

$$\dot{X} = AX + BU \quad (3.48)$$

$$Y = CX \quad (3.49)$$

the system model considered in this study can be described in state-space as

$$X = \begin{bmatrix} \theta_m \\ \dot{\theta}_m \\ \theta_g \\ \dot{\theta}_g \\ \theta_l \\ \dot{\theta}_l \end{bmatrix} \quad (3.50)$$

$$\dot{X} = \begin{bmatrix} 0 & 1 & 0 & 0 & 0 & 0 \\ -\frac{k_{s1}}{J_m} & -\frac{c_m+c_{s1}}{J_m} & \frac{k_{s1}}{J_m} & \frac{c_{s1}}{J_m} & 0 & 0 \\ 0 & 0 & 0 & 1 & 0 & 0 \\ \frac{k_{s1}}{J_g} & \frac{c_{s1}}{J_g} & -\frac{k_{s1}+k_{s2}}{J_g} & -\frac{c_{s1}+c_{s2}+c_g}{J_g} & \frac{k_{s2}}{J_g} & \frac{c_{s2}}{J_g} \\ 0 & 0 & 0 & 0 & 0 & 1 \\ 0 & 0 & \frac{k_{s2}}{J_l} & \frac{c_{s2}}{J_l} & -\frac{k_{s2}}{J_l} & -\frac{c_{s1}+c_{s2}}{J_l} \end{bmatrix} X + \begin{bmatrix} 0 \\ \frac{1}{J_m} \\ 0 \\ 0 \\ 0 \\ 0 \end{bmatrix} T_m \quad (3.51)$$

$$C = \begin{bmatrix} 0 & 1 & 0 & 0 & 0 & 0 \\ 0 & 0 & 0 & 1 & 0 & 0 \end{bmatrix} \quad (3.52)$$

As seen in above expressions, a parametric evaluation of the observability and controllability Grammians is impractical. Hence, both Grammians are evaluated numerically, for the sample system whose parameters are given in Table 3.5. This yields

$$Q_C = \begin{bmatrix} 0 & 3.3 \times 10^{-2} & -1.11 \times 10^{-1} & -2 \times 10^2 & 1.33 \times 10^2 & 1.55 \times 10^6 \\ 3.3 \times 10^{-2} & -1.11 \times 10^{-1} & -2 \times 10^2 & 1.33 \times 10^3 & 1.55 \times 10^6 & -1.47 \times 10^7 \\ 0 & 0 & 0 & 6 \times 10^1 & -2.6 \times 10^2 & -5.75 \times 10^5 \\ 0 & 0 & 6 \times 10^1 & -2.6 \times 10^2 & -5.75 \times 10^5 & 3.91 \times 10^6 \\ 0 & 0 & 0 & 0 & 0 & 3.6 \times 10^4 \\ 0 & 0 & 0 & 0 & 3.6 \times 10^4 & -1.68 \times 10^5 \end{bmatrix} \quad (3.53)$$

with $rank(Q_C) = 6$ and a 12×6 Q_O matrix with $rank(Q_O) = 5$. Hence the linear system model is theoretically completely controllable but not observable.

The Grammians calculated above show that even if the linear system is theoretically controllable, the control effort to control the "far states" (i.e. load mass speed) is much greater than the "close states" (i.e. motor mass speed) - note the difference in order of magnitudes of different column entries of the Q_C matrix. Moreover, our system is not observable with the current first and second mass velocity feedbacks and further feedbacks may be needed in order to be able to completely observe the states.

3.3.5 Some Studies on the Experimental Setup

Up until this point, several analysis on the linear plant model have been performed. The utilised linear plant model has a physical parameter set, which can be used to enlighten the relationship between the mechanical properties of the system and its dynamic behaviour. However, as it will be explored in this sub-section, the real system has more complicated dynamics, and even a linear model catching the rough behaviour of these dynamics has an order of 9. Hence, instead of trying to match the 3-mass model's parameters with the experimental setup, a more general transfer function fitting technique has been employed. Afterwards, the discrepancies between the real system and the fitted linear model behaviours have been investigated to gain more insight on the level of the non-linearity inherent to the system.

3.3.5.1 Transfer Function Identification

In order to fit a linear transfer function to the dynamic behaviour of the experimental system, the frequency sweep tests are employed. An example set of results from such a test is shown in Fig. 3.27. The frequency response function (FRF) of the system is measured using the motor quadrature current (corresponding to motor torque) as the input and the gyroscope feedback (corresponding to feedback speed measurement) as the output. With the assumption that the system is stable, the resultant magnitude plot (assuming a minimum phase system, one can claim that the phase response is unique) has a one-to-one mapping with the transfer function of the dynamic linear system. In this study the genetic algorithm search method is employed in order to fit the s-domain poles and zeros to the obtained FRF magnitude (see Appendix for details of the utilised method). At this point, it is worth to note that the speed control will be effective in the range of 0-20 Hz, hence it is satisfactory to perform the identification process in the range of frequencies between 0-40 Hz.

In order to evaluate the pole-zero arrangements of the linear system model the following reasoning is used: the input of the system is torque, and the output is speed, hence there should be a pole around zero. As seen in Fig. 3.28, there is a deep anti-resonance point around the frequency of $7Hz$, hence there should be a double zero

around this frequency. A similar discussion is also valid for the anti-resonance frequency point around $26Hz$. Considering the shape of the FRF, we should at least add a pole (to flatten the response after rise from anti-resonance frequency around $7Hz$), another pole (to roll the response down to the anti-resonance frequency at $26Hz$), a double zero (to rise the response up after the anti-resonance at $26Hz$) and another pole (to flatten the response after the anti-resonance.) to get this shape. The genetic algorithm fitting is performed (see Appendix for details) on the above collected data, the following result is obtained, using a transfer function with the properties given in Table 3.6, hence the overall system being fitted to a transfer function of order 9.

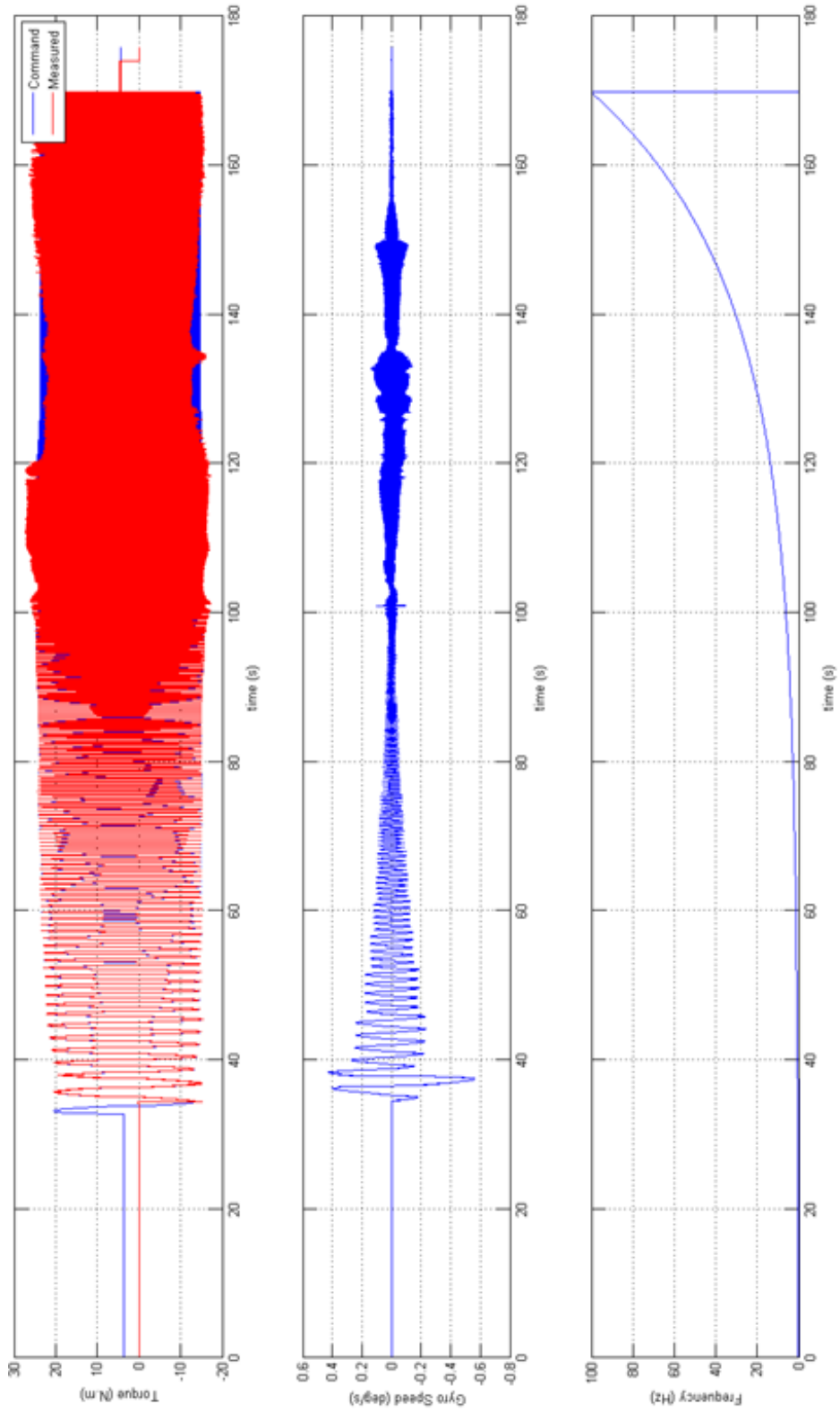


Figure 3.27: Plot of time domain data for torque, angular speed and current frequency for the frequency sweep experiment.

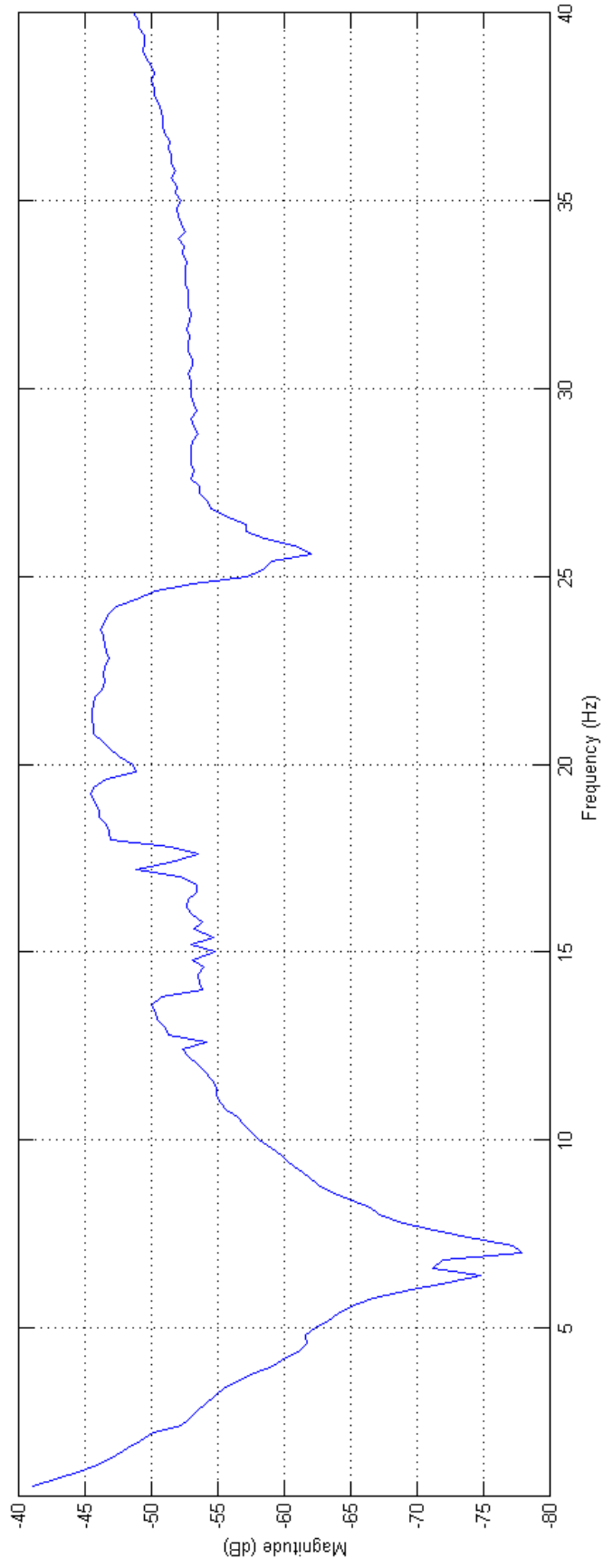


Figure 3.28: Magnitude of the Frequency Response Function of the system obtained using the measured sine-sweep data.

Table 3.6: Properties of the assumed transfer function employed during the genetic algorithm process.

PROPERTY	VALUE
Number of real zeros	2
Numer of complex zero pairs	3
Number of real poles	3
Number of complex pole pairs	3

The genetic algorithm process resulted in the following transfer function:

$$G(s) = \frac{4.876s^8 + 2.210 \times 10^3 s^7 + 6.869 \times 10^5 s^6 + 1.505 \times 10^8 s^5 + 1.862 \times 10^{10} s^4 + 2.525 \times 10^{12} s^3 + 1.089 \times 10^{14} s^2 + 4.465 \times 10^{15} s + 1.264 \times 10^{17}}{s^9 + 1.283 \times 10^3 s^8 + 7.316 \times 10^5 s^7 + 2.450 \times 10^8 s^6 + 5.425 \times 10^{10} s^5 + 8.561 \times 10^{12} s^4 + 9.932 \times 10^{14} s^3 + 7.837 \times 10^{16} s^2 + 3.077 \times 10^{18} s + 2.751 \times 10^{16}} \quad (3.54)$$

When one calculates the poles and zeros of $G(s)$ given in (3.54), the results shown in Table 3.7 are obtained. Observing in this table that $G(s)$ is both stable (all poles with negative real parts) and minimum phase (all zeros with negative real parts), one can justify to have a Bode plot for $G(j\omega)$.

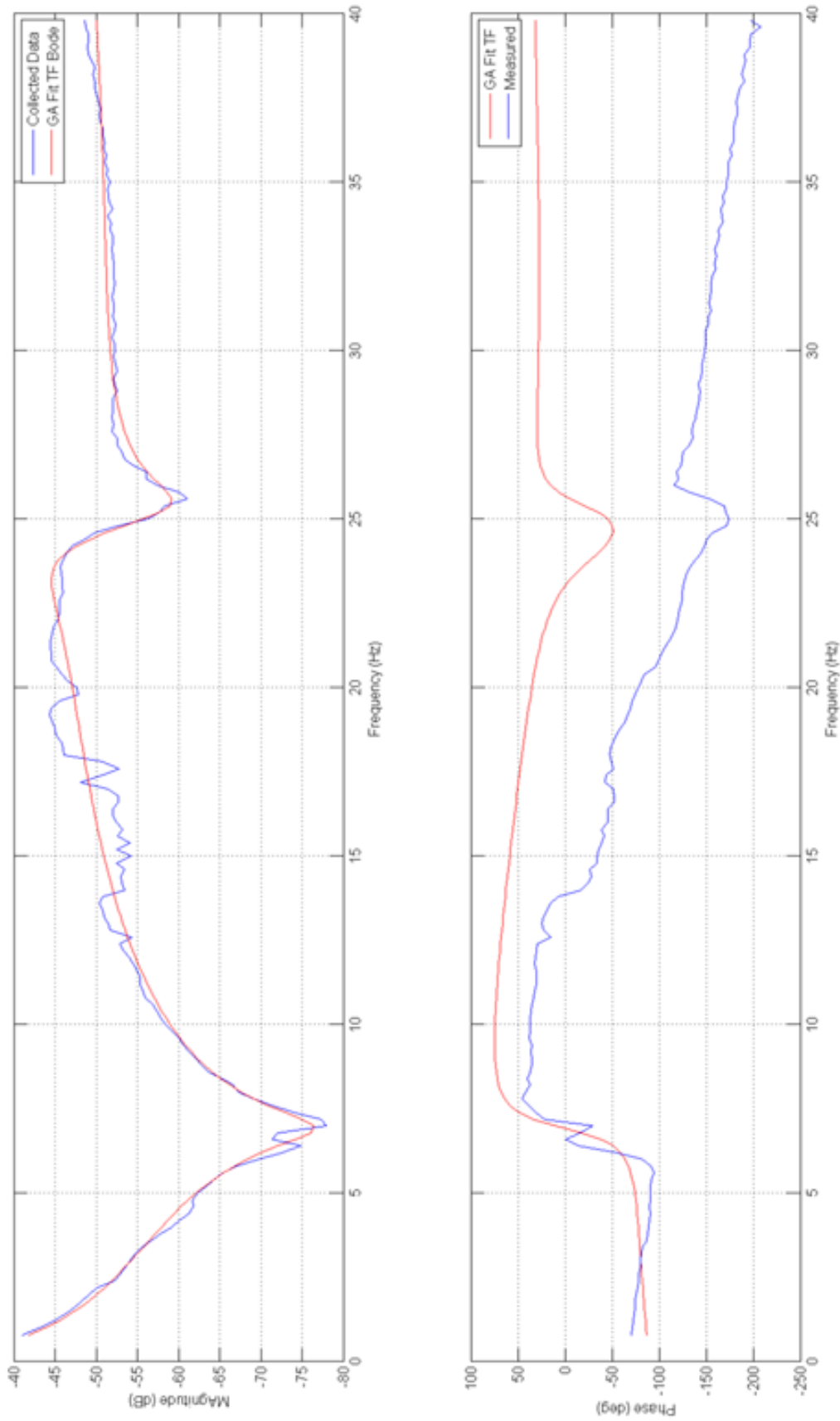


Figure 3.29: Magnitude and Phase of the Frequency Response Function of the system obtained using the measured sine-sweep data (blue) and $G(s)$ evaluated using the genetic algorithm search method (red).

Table 3.7: Zeros and Poles of the Transfer Function $G(s)$ Evaluated Using Genetic Algorithm Method.

ZEROS
-2.5133
-38.97
$-75.39 \pm j221.02$
$-3.57 \pm j159.59$
$-2.51 \pm j43.58$
POLES
-0.01
-208.55
-214.93
$-7.08 \pm j150.72$
$-206.79 \pm j117.10$
$-215.69 \pm j82.75$

The transfer function's Bode plot is shown in red in Fig. 3.29, along with the measured sine-swept frequency response function. As expected, the magnitude response shows a considerable degree of fit. One might argue that the phase response does not fit very correctly; however this may be overcome with incorporating the phase response in the genetic algorithm runs. Moreover, the tendency of the phase response is mostly similar between measured and fitted FRF data. When a proper delay term (transport delays in measurements and commands) and a constant phase offset are added for structural damping (originating from the test-bed's non-rigid connection with the ground), one gets the result shown in Fig. 3.30

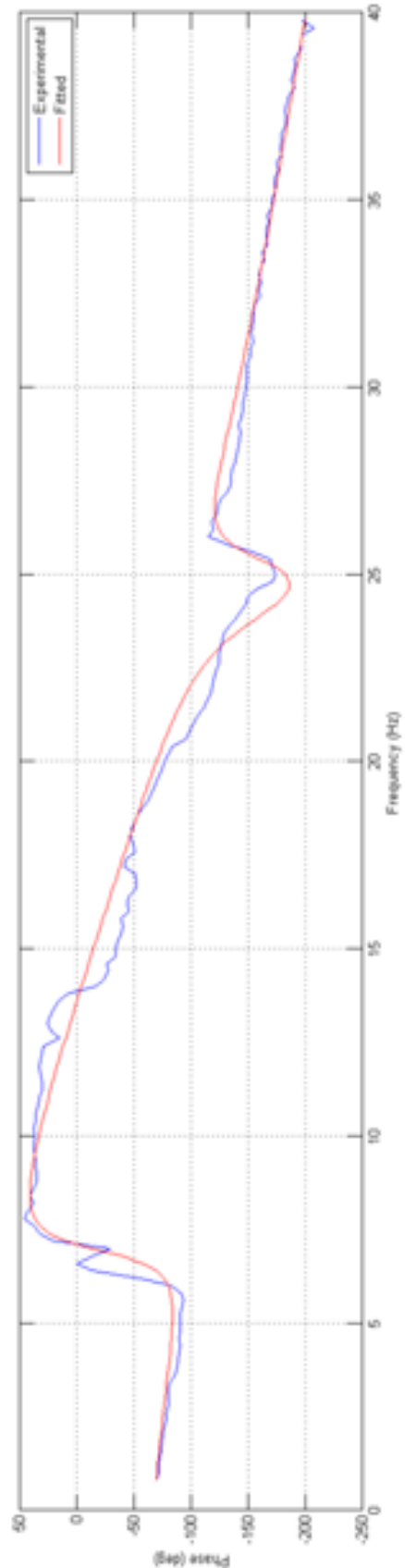
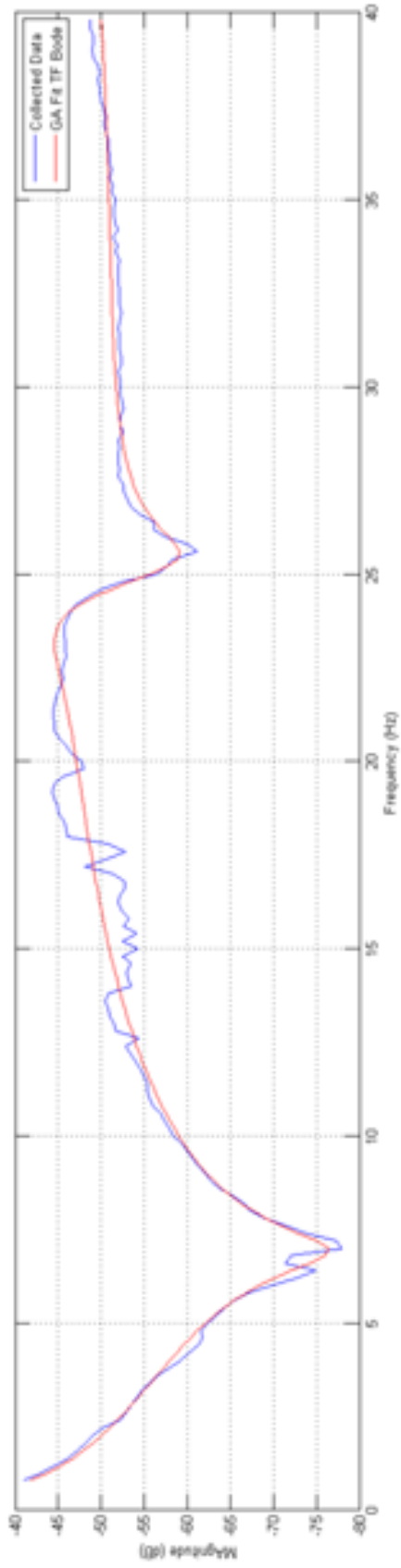


Figure 3.30: Experimentally obtained and transfer function fitted frequency response plots with a delay of 17ms and phase offset of 22° .

In summary, one can approximate the "linear behaviour" of the utilised system with a 9th order transfer function. On the other hand, a multi-body model with proper mechanical parameters is more useful to be able to comment on the system behaviour in terms of mechanical design parameters. That is the analysis is performed using approximate values given in Table 3.5. Nevertheless, employing a well-matching linear model for the plant is only useful to gain insight, rather than performing the control design using this linear model, as the real system behaves in a quite non-linear fashion, as it will be investigated in the next sub-section.

3.3.5.2 Discrepancies Between Experimental Results and Linear Behaviour

As one can deduce from the preceding sub-sections, it is possible to employ the experimental results to generate a linear model of the system to approximate the dynamic behaviour. In this sub-section, the validity of the linear model is investigated in more detail, in order to gain insight and be able to comment on the type and complexity of the controller that should be employed to control the system, even beyond the first open-loop anti-resonance frequency. For this purpose, two experimental methods are employed: First, the frequency sweep test is repeated with different torque (motor current) amplitudes. Second, the time-domain behaviour of the system was investigated in steady-state, when it is excited with a single-tone sine input torque at several different frequencies.

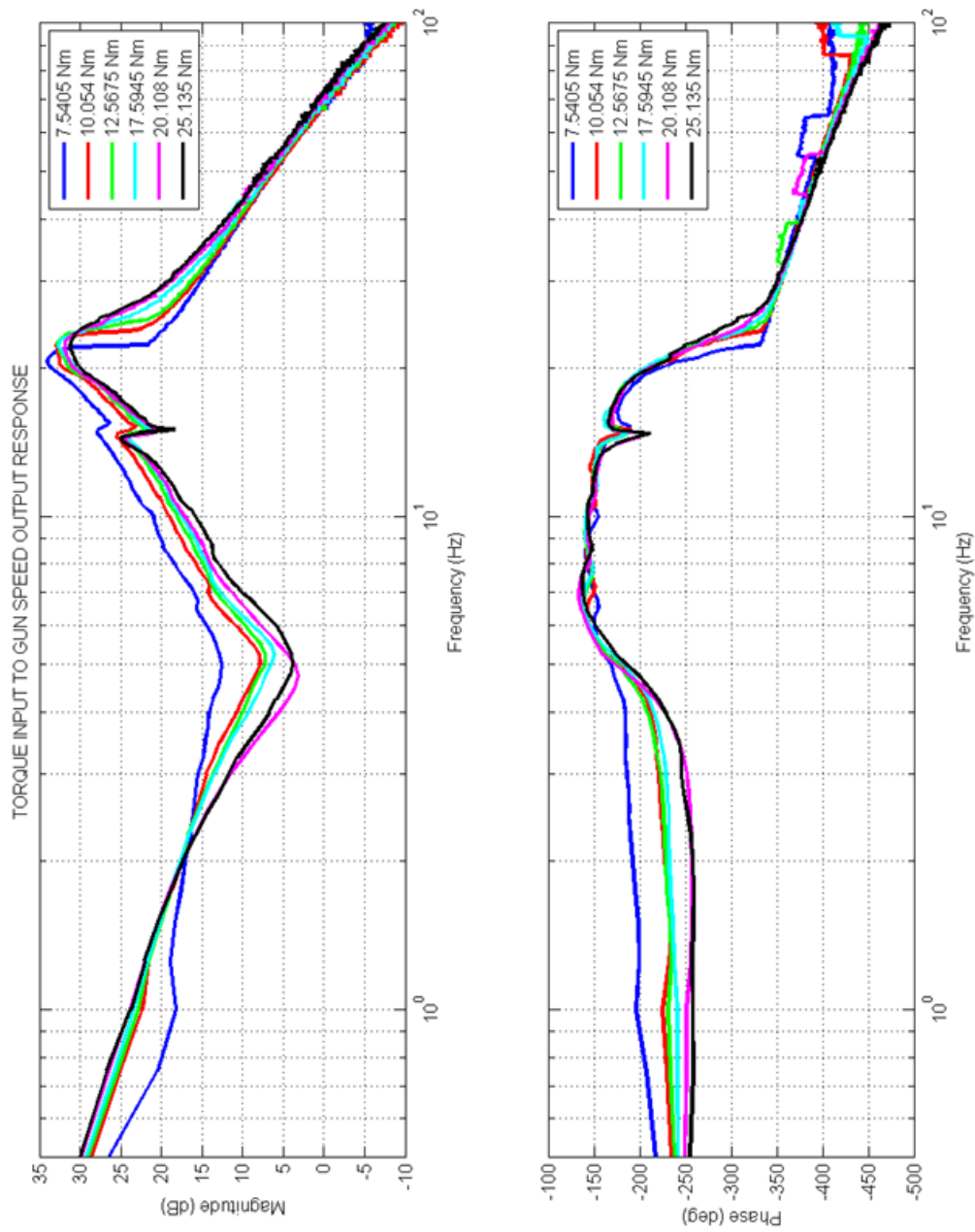


Figure 3.31: Frequency response of the plant for different motor current (torque) input amplitudes.

When the frequency sweep tests are performed with different torque amplitudes, the result given in Fig. 3.31 is obtained. This result shows that even if the system is dominated by a "linear transfer function model", this model (matching the FRF) changes with the input torque (excitation) amplitude. Moreover, one can make the following observations:

- For the smallest excitation amplitude, since the stiction is dominant, system cannot even move properly. Hence, at very low frequencies the gain is low.
- As the excitation torque amplitude is increased, low frequency system gain converges through the same value, which corresponds to (the inverse of) the equivalent inertia of the system, as at these frequencies the system may be approximated by $T = J\dot{\omega}$, yielding $\Omega(s)/T(s) = 1/J$.
- The anti-resonance and resonance frequencies slightly increase with increasing excitation amplitude, but overall change is on the order of 0.1 Hz
- The gain at the resonance frequency decreases as excitation amplitude increases. This corresponds to the fact that as the excitation torque amplitude increases the system starts moving faster resulting in higher effective damping

The above observations can be used to deduce the fact that a solely linear model is not satisfactory to completely represent the abstract system and perform the control design.

Besides the dynamics altering as the input excitation amplitude is increased, it is worth to investigate the time-domain behavior of the system to single-tone sinusoidal excitation at different frequencies. This would give insight on the level of non-linearity of the system.

From Fig. 3.33 to Fig. 3.38, time-domain data for a very low frequency (0.75 Hz), two moderate frequencies (2 Hz and 5 Hz), a frequency close to the anti-resonance (7 Hz), a frequency close to the resonance (18 Hz), and a high frequency (38 Hz) are represented. Fig. 3.32 is also given in order to show the gyro noise level, which is in the order of a few milli-degrees per second (i.e. measured speed levels are not mere gyro noise). From all these figures, one can state the following observations:

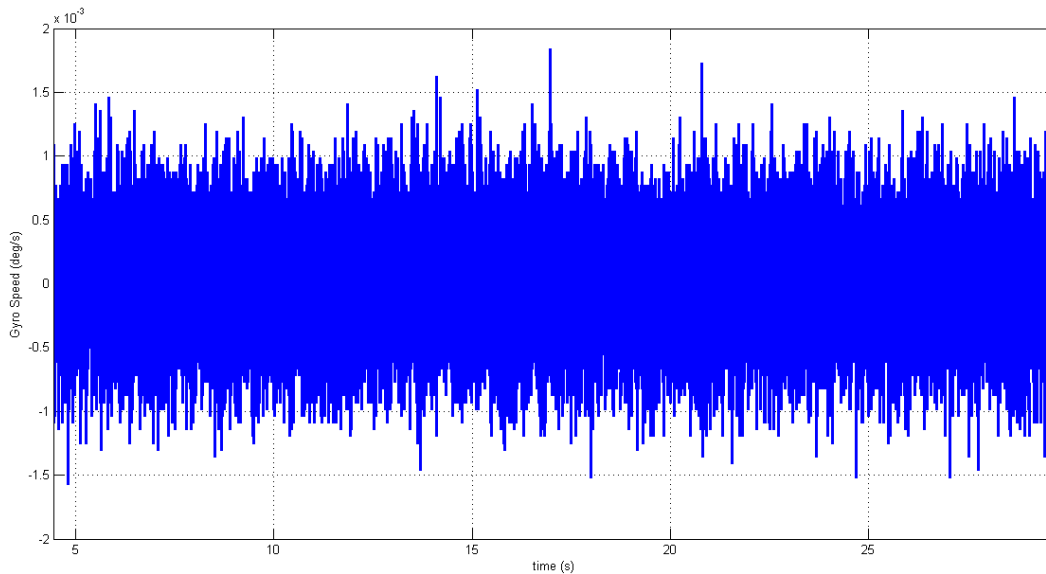


Figure 3.32: Gyro noise for the stationary system, whose level is in the order of 0.002 deg/s peak-peak.

- At low frequencies the system is mainly linear, giving mere sinusoidal output for a sinusoidal torque input (Fig. 3.33)
- As the frequency is increased to a few Hz (Fig. 3.34 and Fig. 3.35), output diverges from a pure sinusoidal one, meaning non-linear effects come into play
- At the anti-resonance frequency, the linear gain of the system is too low, and output is dominated by the harmonics, meaning that the behavior of the system is mostly non-linear at this frequency (Fig. 3.36).
- At around the resonance frequency (Fig. 3.37), the linear gain of the system is large and the system behaves mostly as a gain, i.e. linear.
- At a frequency higher than the resonance (Fig. 3.38), the gain of the system is low, on the other hand, as the load is 'decoupled' from the remaining part of the system linear behavior dominates.

Looking at the observations on the time-domain response of the system to single-tone sinusoidal excitations, one can state that by suppressing the system dynamics at and above anti-resonance, a linear controller would perform satisfactory performance. However, if the aim of the control is to increase the bandwidth beyond the

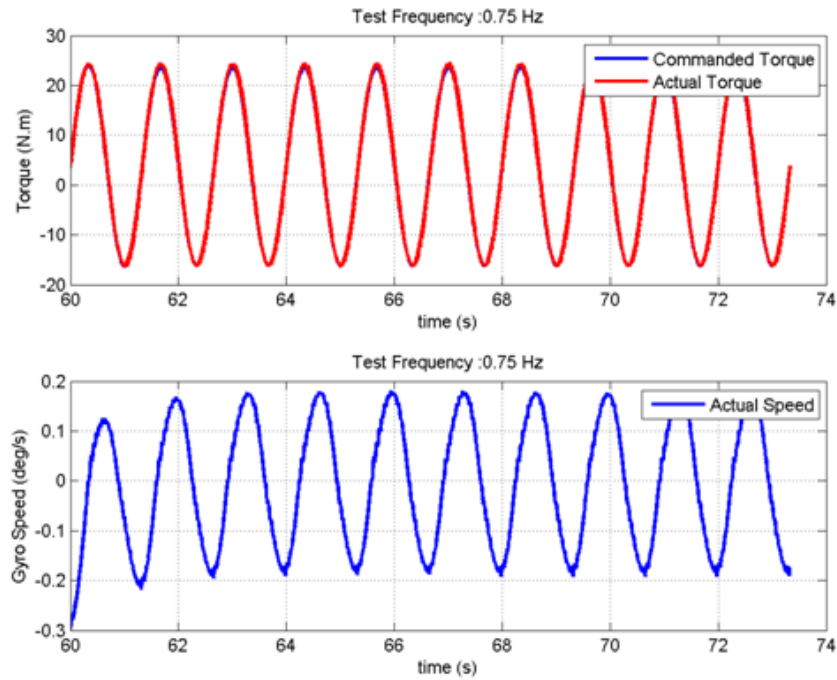


Figure 3.33: Time domain data from frequency sweep tests, at the frequency 0.75Hz .

anti-resonance frequency, then linear control is not enough to accomplish the speed control problem.

This subsection can be summarized as follows: In the given system, a linear system model may be employed to describe the FRF behaviour. However, one cannot directly employ a high performance linear controller, even a non-linear one without considering the non-linear effects, which are easily observed via changing excitation amplitude or investigating time-domain data. On the other hand, non-linear effects usually cannot be completely modeled. Hence most suitable methods for speed control of motion platforms should include some "adaptive" controllers with system behavior "predictors".

3.4 Reference Controller Designs

In this section, three different techniques are employed for designing speed controllers for the given system. The first controller is a PIDF controller, this type of controller is employed as it is the most popular controller form with practical importance. The second controller is a fuzzy logic controller and it is utilised as a popular

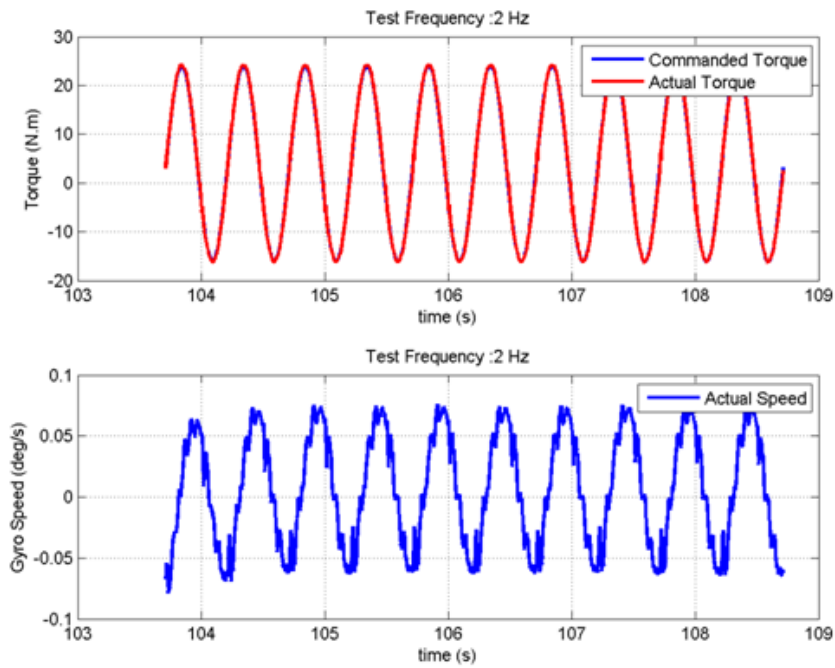


Figure 3.34: Time domain data from frequency sweep tests, at the frequency $2Hz$.

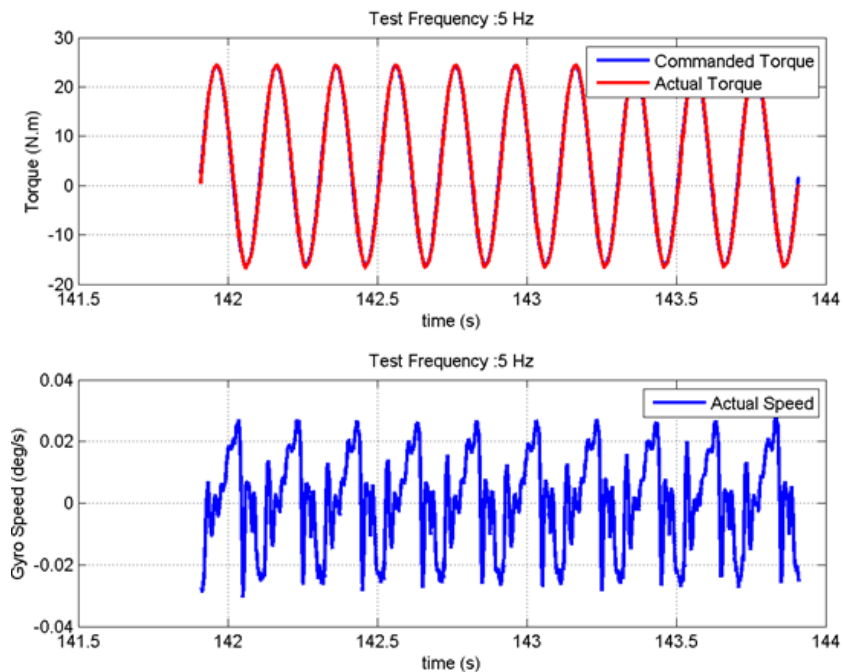


Figure 3.35: Time domain data from frequency sweep tests, at the frequency $5Hz$.

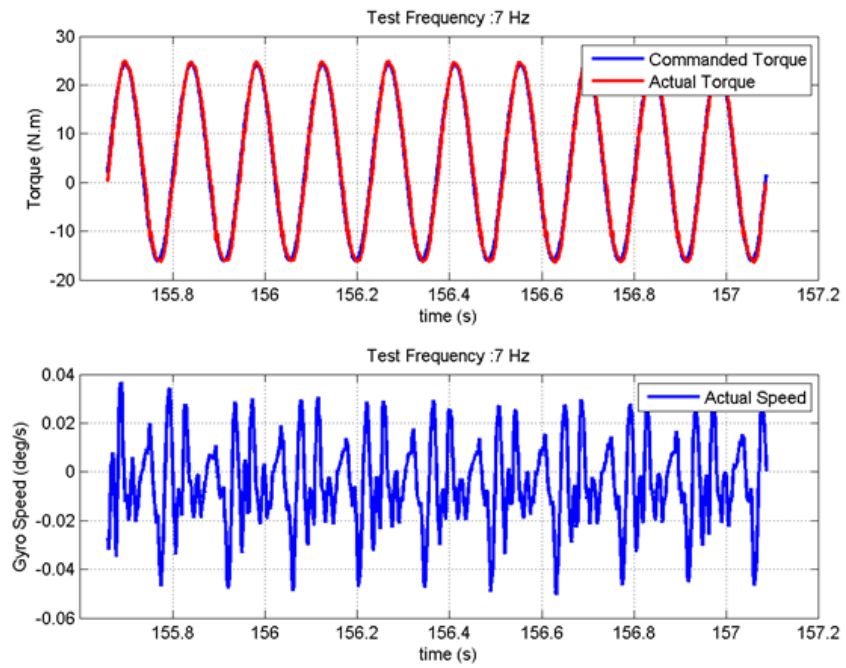


Figure 3.36: Time domain data from frequency sweep tests, at the frequency $7Hz$.

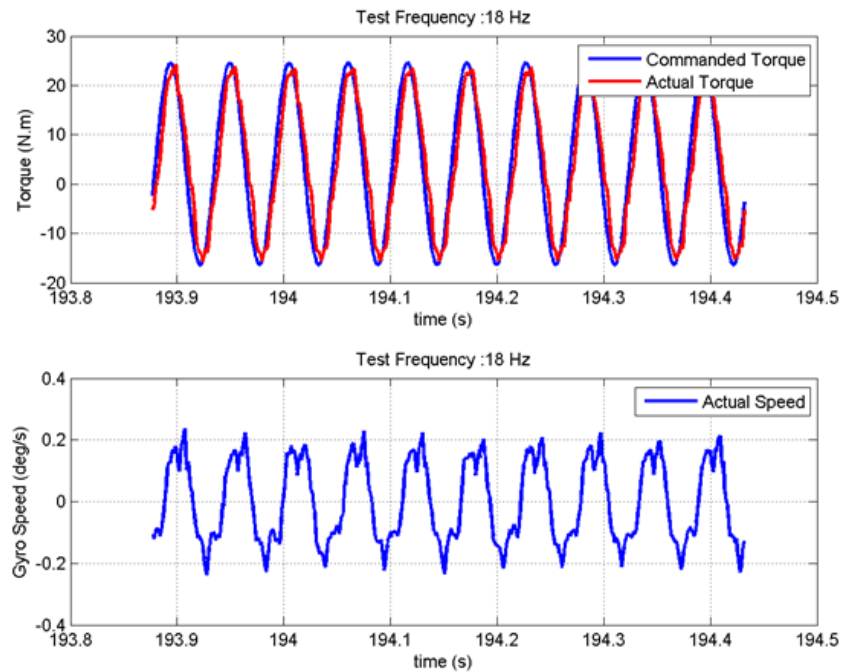


Figure 3.37: Time domain data from frequency sweep tests, at the frequency $18Hz$.

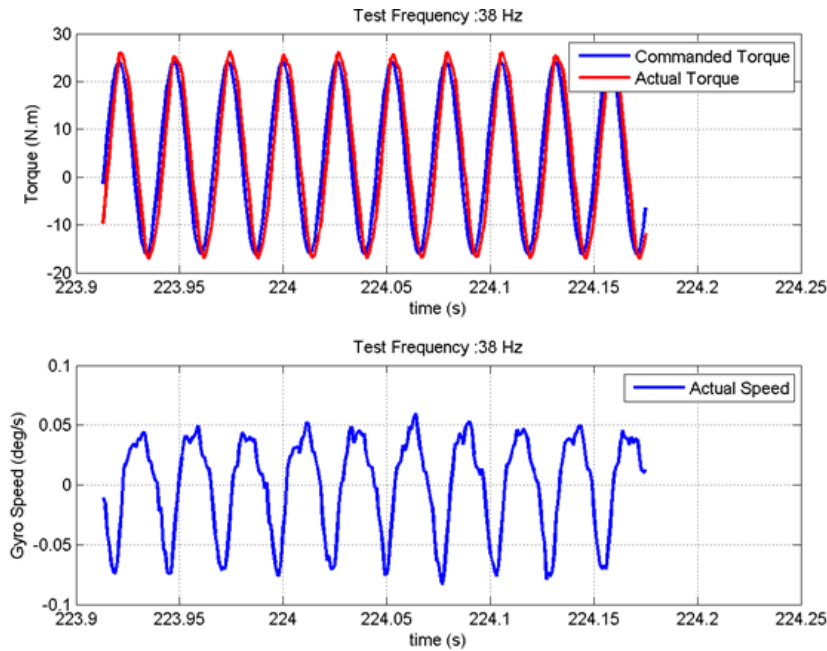


Figure 3.38: Time domain data from frequency sweep tests, at the frequency $38Hz$.

example of a non-linear intelligent controller. The third controller is a direct pole-placement design and it is utilised to show the limits of theoretical linear control and its fragility against system parameter variations.

3.4.1 Proportional-Integral-Derivative with Filter (PIDF) Design

Using the transfer function model obtained via the identification process, speed control of the system has been performed using the PIDF controller. The design is achieved using MATLAB's Control Design Toolbox, with optimum step response performance with maximum controller output of 120 Nm (which is the real limit of the motor utilised in the experimental setup).

The Simulink model used for simulation is shown in Fig. 3.39, whereas the step response is given in Fig. 3.40. The parameters and transient performance of the controlled system are summarized in Table 3.8.

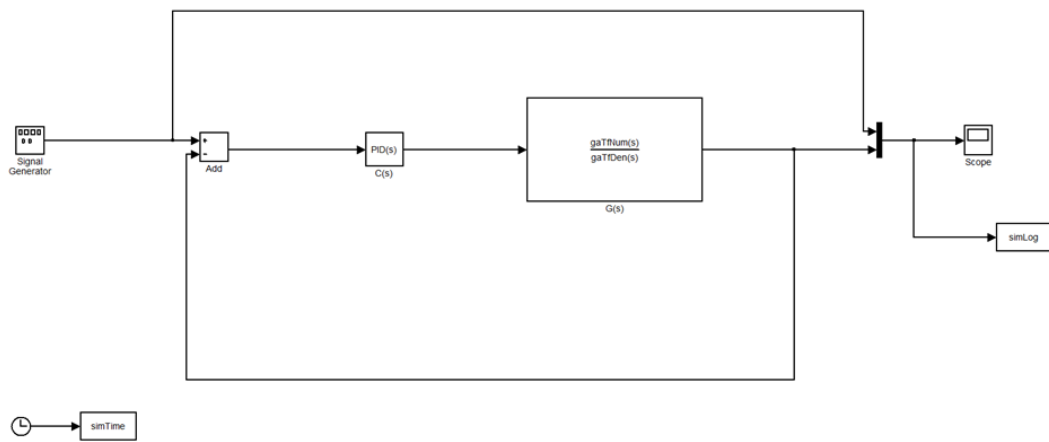


Figure 3.39: Simulink Model used to perform simulations for the response of $G(s)$ with a simple PIDF controller.

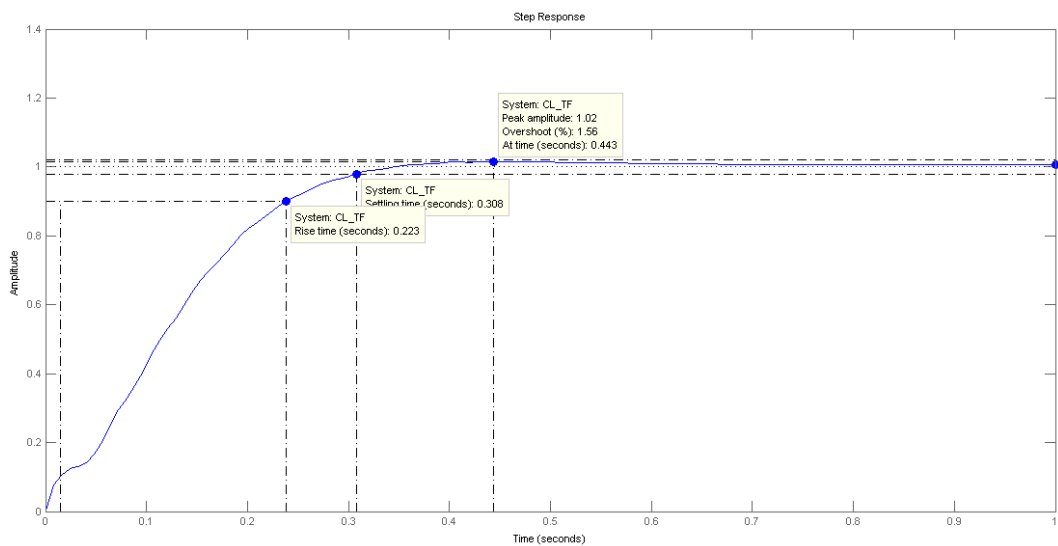


Figure 3.40: Step response of the closed loop system employing a PIDF controller.

Table 3.8: PIDF Controller Parameters and Performance Measures.

PARAMETER	VALUE
K_P	195.6
K_I	12.81
K_D	9.688
$T_F(\text{filter time constant})$	4.954×10^{-2}
Rise Time	223ms
Settling Time	308ms
Percent Overshoot	1.56%

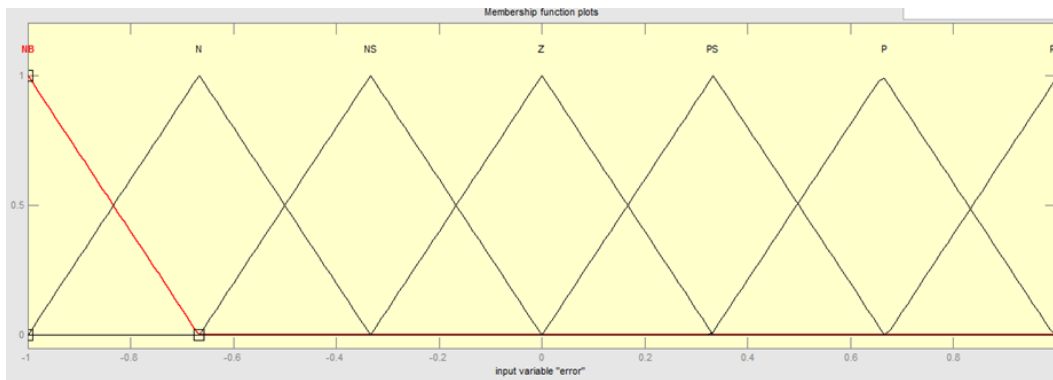


Figure 3.41: Membership functions of the 7 fuzzy sets used for both input and output variables.

3.4.2 Sample Fuzzy Controller Design

A fuzzy logic controller has been designed for the closed loop control of the identified plant. A 2 input - 1 output fuzzy logic controller has been employed, which is similar to a PI control structure. First input is the error and the second input is the integral of the error. Triangular membership functions given in Fig. 3.41 is used for all the variables, with normalized gains.

The rule base has been obtained by “AND”ing the two input variable sets in order to find the output fuzzy set, yielding a rule-base consisting of 49 rules. The resulting I/O mapping with this rule base and above membership functions is given in Fig. 3.42

In order to evaluate the performance of the fuzzy logic controller, a simulation has been performed in the Simulink environment, as shown in Fig. 3.43. The result obtained is shown in Fig. 3.44. It can be stated that fuzzy logic controller is a promising

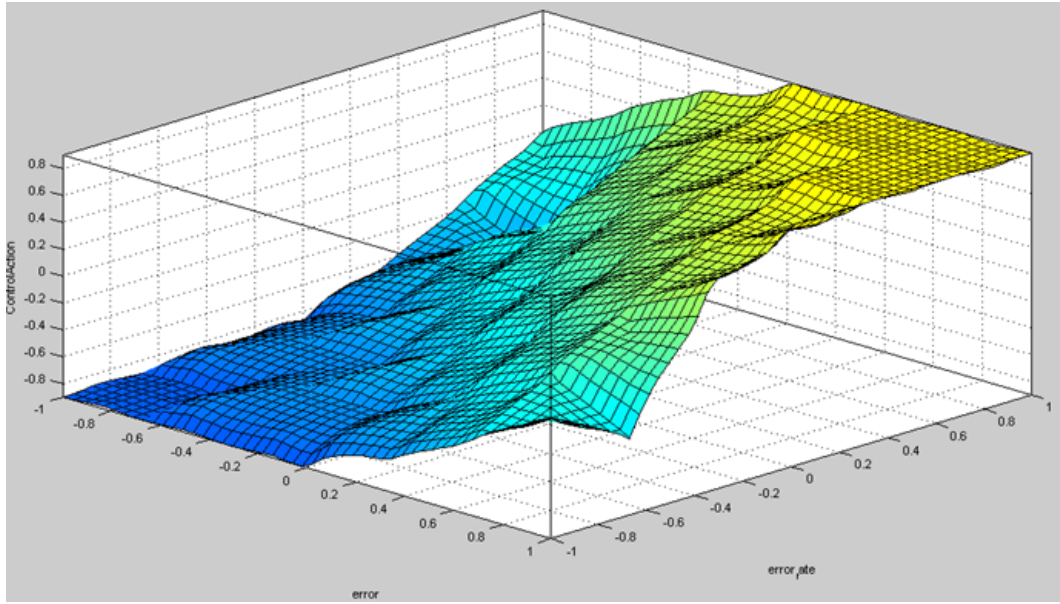


Figure 3.42: Fuzzy Logic Controller I/O mapping with the membership functions given in Fig. 3.41 and a 49-rule rule base.

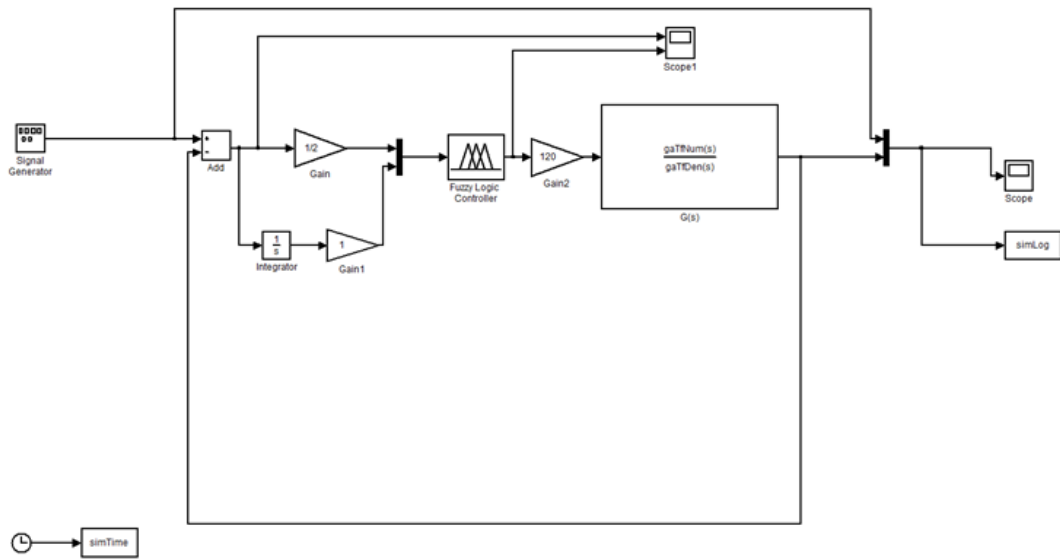


Figure 3.43: Simulink Implementation of the closed loop system with fuzzy logic controller.

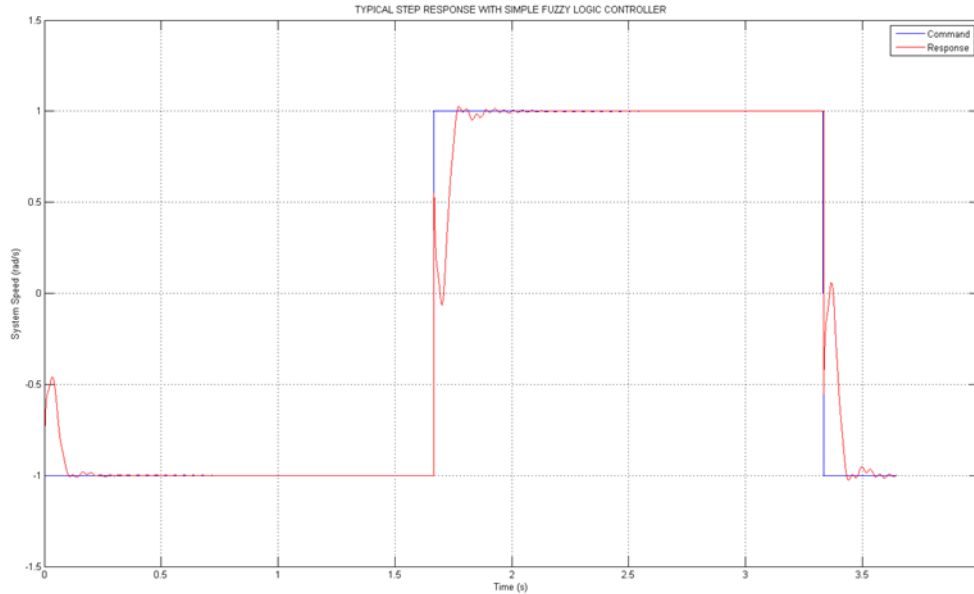


Figure 3.44: Step response of the closed-loop system given in Fig. 3.43.

method for closed loop speed control of a motion platform, however it needs some modifications and enhancements in order to obtain a satisfactory result: Note that, unlike PIDF controller, the fuzzy logic controller can demand full torque at the beginning of the step command. However, there occurs to be a "non-minimum phase"-like behaviour and error starts to increase for some time after the "full-demand". This is actually not a good performance for a speed control system due to high jerks caused.

Both of the above mentioned designs did not perform as expected on the real system during experiments. Actually, this is an expected result since both of the designs assumed that the system was completely defined by the transfer function, which corresponds to the linear behaviour. Hence, one can state that there occurs to be strong non-linear effects in our system (as observed in the last section), which might not be modeled or compensated directly.

3.4.3 The Method of Truxal and Guillemin (Direct Pole-Placement)

The method of Truxal and Guillemin is a realizable version of direct pole-placement. Consider the classical closed-loop system with controller $G_C(s)$ and plant $G_P(s)$ as given in Fig. 3.45.

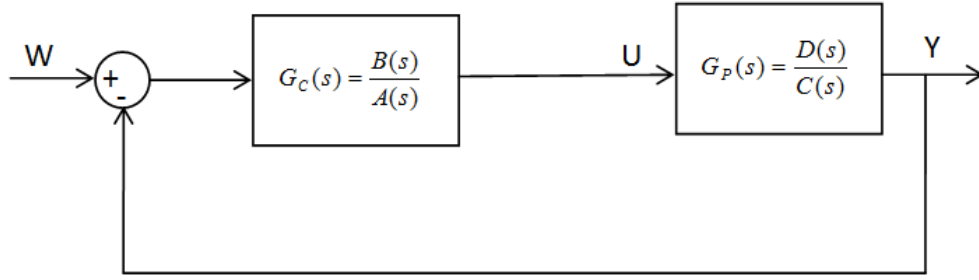


Figure 3.45: Typical closed loop control structure.

The general form of the plant transfer function is

$$G_P(s) = \frac{D(s)}{C(s)} = \frac{d_0 + d_1s + d_2s^2 + \dots + d_ms^m}{c_0 + c_1s + c_2s^2 + \dots + c_ns^n} \quad (3.55)$$

with $D(s)$ and $C(s)$ polynomials having no common roots, $c_n = 1$ and $m < n$. $G_P(s)$ is assumed to be stable and minimum phase (true for our case). Let the controller to be designed have the following form

$$G_C(s) = \frac{B(s)}{A(s)} = \frac{b_0 + b_1s + b_2s^2 + \dots + b_ws^w}{a_0 + a_1s + a_2s^2 + \dots + a_zs^z} \quad (3.56)$$

with $a_z = 1$ and $w < z$.

Let the controller be designed such that the closed-loop transfer function becomes

$$K_W(s) = \frac{\alpha(s)}{\beta(s)} = \frac{\alpha_0 + \alpha_1s + \alpha_2s^2 + \dots + \alpha_vs^v}{\beta_0 + \beta_1s + \beta_2s^2 + \dots + \beta_us^u} \quad (3.57)$$

which could be freely chosen, under the condition that the controller is realizable (i.e. $w < z$).

The closed-loop transfer function can be written in terms of plant and controller transfer functions as follows

$$K_W(s) = \frac{G_C(s)G_P(s)}{1 + G_C(s)G_P(s)} \quad (3.58)$$

Given the desired closed-loop transfer function $K_W(s)$, the controller $G_C(s)$ can be

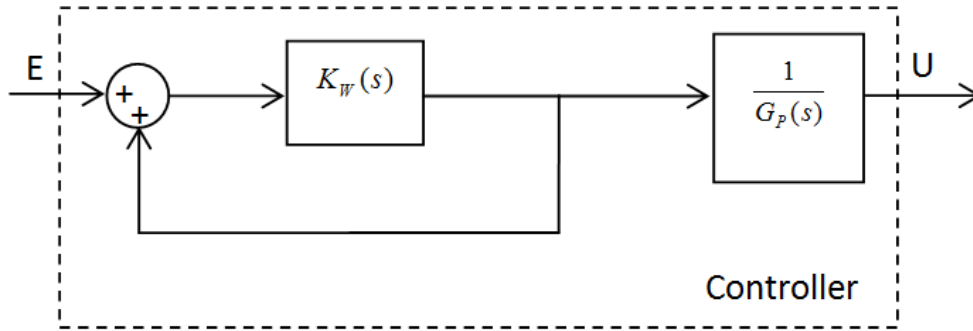


Figure 3.46: Structure of the controller in Truxal and Guillemin design.

evaluated using 3.58; which gives:

$$G_C(s) = \frac{1}{G_P(s)} \frac{K_W(s)}{1 - K_W(s)} \quad (3.59)$$

The condition of realizability of $G_C(s)$ becomes:

$$\deg(B(s)) \leq \deg(A(s)) \implies (n + v) \leq (m + u) \implies (u - v) \geq (n - m) \quad (3.60)$$

The above equation can be written in words as follows: The pole excess of the desired closed-loop transfer function must be larger than or equal to the pole excess of the plant. Within these constraints the closed-loop transfer function is free. The controller has the form given in Fig. 3.46.

For this case the linear model with mechanical parameters is employed (as this will result in a more complicated closed loop dynamics). The pole excess of the plant is 3 (see 3.41). Hence, the closed-loop transfer function must at least have 3 excessive poles. Let it have the simplest realizable form with 0 dB DC gain, triple poles which are far enough from the origin:

$$K_W(s) = \frac{60^3}{(s + 60)^3} \quad (3.61)$$

When one performs the design using the plant transfer function given in (3.41), the fifth order controller transfer function shown below is obtained

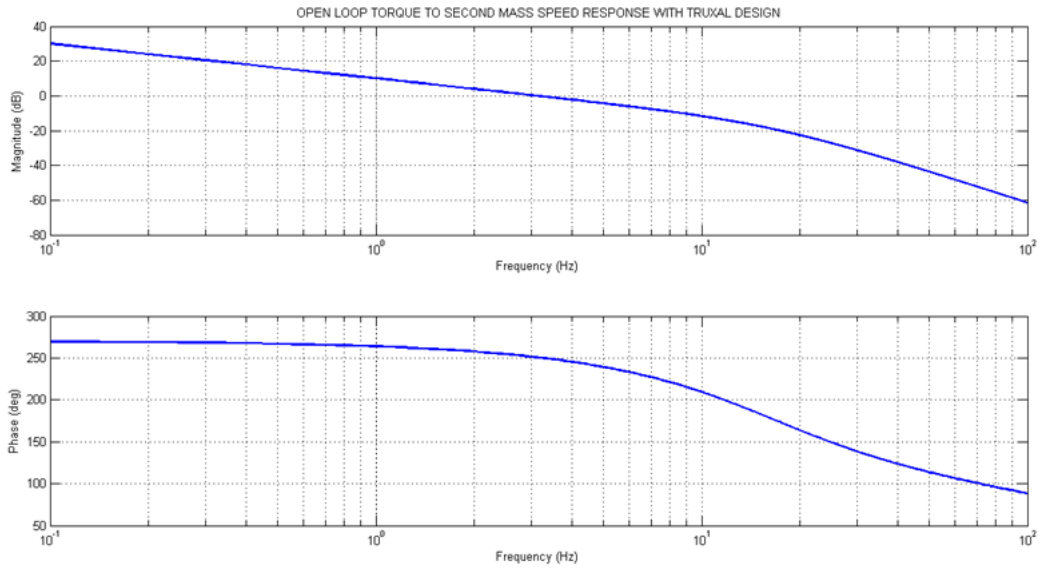


Figure 3.47: Open-loop FRF with Truxal-Guillemin design simulation of three mass linear system.

$$G_C(s) = \frac{3.888 \times 10^{10} + 5.576 \times 10^{10}s + 8.568 \times 10^7 s^2 + 3.674 \times 10^7 s^3 + 1.68 \times 10^4 s^4 + 3600s^5}{6.48 \times 10^6 s + 1.116 \times 10^5 s^2 + 1.146 \times 10^4 s^3 + 180.3s^4 + s^5} \quad (3.62)$$

This is the simplest controller form one can obtain with Truxal-Guillemin method, since the minimum number of pole excess in the controller with no zeros is utilised. Theoretical open-loop and closed FRF plots with this design are given in Fig. 3.47 and Fig. 3.48, respectively.

As seen in these figures, the anti-resonance of the open-loop plant has been completely eliminated via pole-placement. However, when one investigates the time-domain behaviour of the control signal (output of the controller) during an open-loop sine sweep (Fig. 3.49), it is easily observed that at the anti-resonance frequency the control signal reaches very high values, this is indeed something needed for control purpose in theory, however in practice any shift in the anti-resonance frequency will lead to very high open-loop gains and therefore possible instabilities.

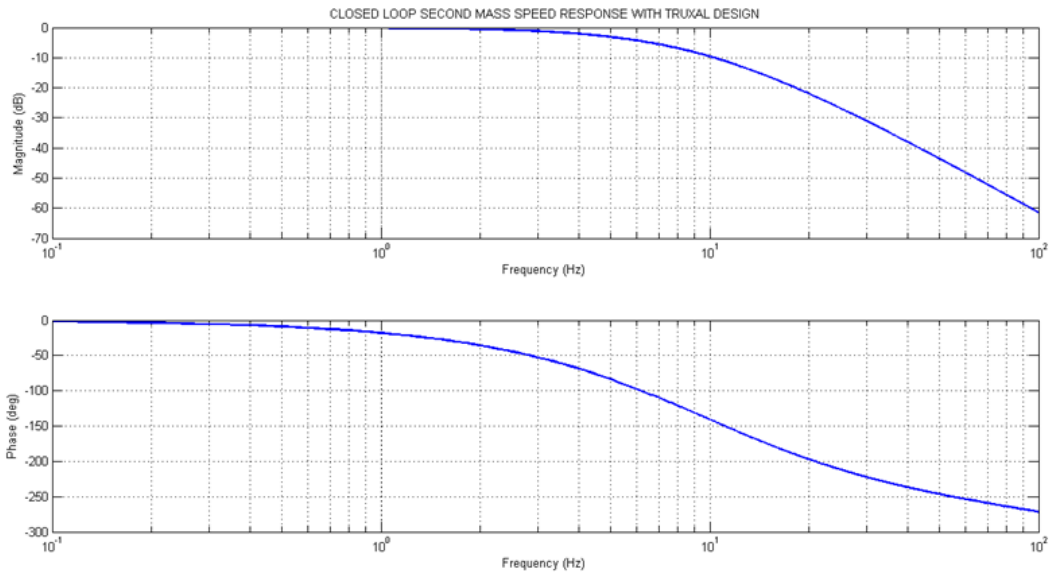


Figure 3.48: Closed-loop FRF with Truxal-Guillemine design simulation of three mass linear system.

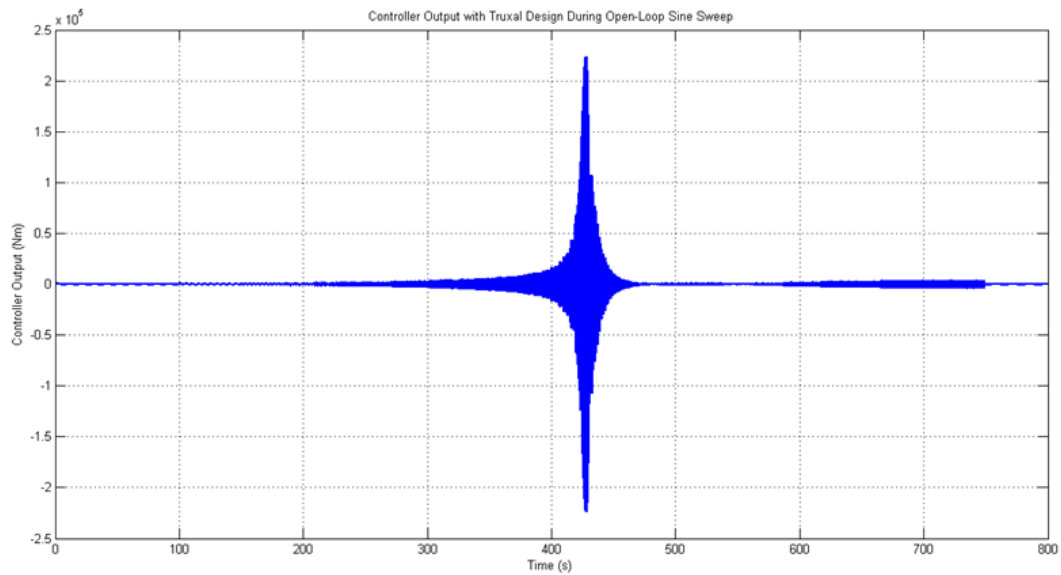


Figure 3.49: Controller output during a sine-sweep velocity reference with Truxal-Guillemine design simulation of three mass linear system.

3.4.4 Section Summary

This section has been dedicated to control designs with PIDF, fuzzy logic and direct pole-placement approaches. As the plant model, we employed either higher-order FRF fit (PIDF and fuzzy logic cases) or lower-order mechanical model (direct pole-placement). After performing these control designs, the following observations can be stated:

- PIDF controller may show a good performance for a linear time-invariant system. However, as the real system changes behaviour with different torque input levels, its practical performance would be limited.
- Fuzzy logic control design has been performed since it is a popular and well-studied non-linear control approach. At the end, it is possible to obtain an acceptable step response in simulations. However, practical application of fuzzy-logic controller would at least need adaptation of its fuzzy set parameters.
- Direct pole-placement is performed to show the fragility of the approach in a practical application: It is possible to set the closed-loop system transfer function to a high performance one (i.e. fast responding, nearly unity at frequencies of interest). As the open-loop poles are directly cancelled via the controller, any shift in these pole locations may cause instability.

3.5 Chapter Summary

In this chapter, efforts given to modeling and performing experiments in order to gain insight on different sub-problems of a motion platform were explained in detail. The findings on these efforts may be summarized as follows:

- Current control of brushless electric motors may be treated separately if one is concerned with the speed control of a motion platform, as long as bandwidth of the current control is carefully evaluated and set high enough. This can mainly be achieved by minimizing the transport delays in the current control loop.

Even if current loop interacts with the mechanical components in the system, this interaction can be compensated via the current controller.

- Backlash and friction are the main non-linear effects dominating in a motion platform - as in the case of any mechanical system. As long as our system is concerned, as the main focus is the speed control, and backlash value (being 0.043° on the motor side) and friction value (being 4%) are low enough, it might be said that they do not dominate statically.
- The analysis of the multi-body dynamics of the mechanical system showed that it is dominated especially by the stiffness of the second link (k_{s2}) and the inertia of the third mass (J_I), which determine the location of the very first anti-resonance for our case.
- Several experiments performed on the setup showed that, the non-linearities in the system are actually quite dynamic and dominant; making it an impractical effort to model them. They change behaviour both with the frequency and the amplitude of the input excitation. It was also shown that a multi-order (9 in our case) linear transfer function maybe fitted to the FRF to be employed as a plant model for controller design. However, as this model has no physical parameters, employing a lower order model corresponding to a three-mass mechanical system with physical parameters maybe more useful for simulation studies.
- PIDF, fuzzy-logic and direct-pole placement controllers were designed by utilising the linear system models evaluated in this chapter. The simulation results for all of the controller designs are promising. However, none of the controllers perform as expected on the real system. This is an expected result, as the real system possess several non-linear effects which are not taken into account by the controller designs.

Keeping the above evaluations in mind, one can say that a control architecture to perform the speed control of a motion platform should be best with an intelligent, fast converging, self-structuring, non-linear and adaptive controller, possessing an on-line system identifier as well.

In the next chapter, a novel control approach for the speed control of motion platforms will be proposed, analysed, simulated and experimented. Several findings from this chapter will be employed to evaluate the performance of the proposed method.

CHAPTER 4

SELF-RECURRENT WAVELET NEURAL NETWORK BASED INDIRECT ADAPTIVE CONTROLLER WITH OPTIMIZED ADAPTIVE LEARNING RATES AND STRUCTURE LEARNING

4.1 Wavelets and Wavelet Neural Networks

A wavelet is a small wave function (i.e. it grows and decays in finite time) ,usually denoted by $\psi(\cdot)$, with the following properties

$$\int_{-\infty}^{\infty} \psi(u)du = 0; \int_{-\infty}^{\infty} \psi^2(u)du = 1; 0 < \int_{-\infty}^{\infty} \frac{|\Psi(f)|^2}{f} df < \infty \quad (4.1)$$

where $\Psi(f)$ denotes the Fourier transform of $\psi(u)$. A typical wavelet, which is also employed in this study, is called the Gaussian derivative given by

$$\psi(u) = -ue^{-\frac{u^2}{2}} \quad (4.2)$$

Its mother wavelet plot (with no translation and unity dilation) is shown in Fig. 4.1.

In multi-resolution analysis (MRA) the mother wavelet $\psi(\cdot)$ is translated and dilated in order to build up resolution levels as indicated below:

$$\psi_{\lambda,t}(u) = \frac{1}{\sqrt{\lambda}}\psi\left(\frac{u-t}{\lambda}\right) \quad (4.3)$$

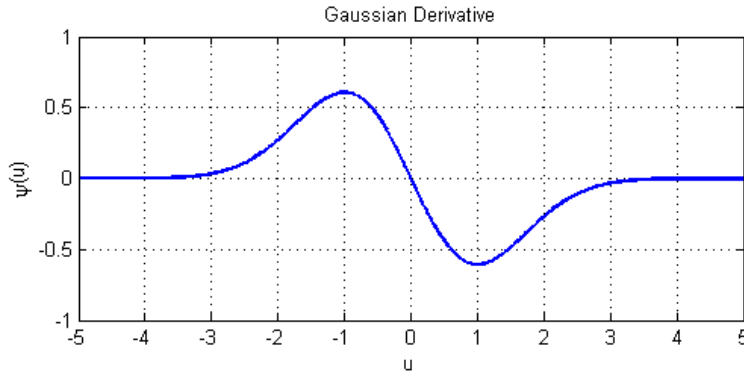


Figure 4.1: Plot of the Gaussian derivative wavelet.

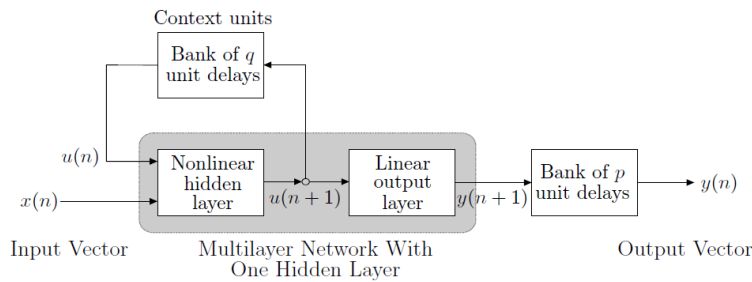


Figure 4.2: Recurrent Neural Network in State-Space Model form. ([58])

where λ is called the "dilation" and t is called the "translation" of the wavelet. Wavelet theory is a very versatile tool in signal processing and a comprehensive coverage of wavelets and wavelet analysis may be found in [43].

Wavelet Neural Networks (WNNs) are neural networks in which neurons' activation functions are wavelets (hence such neurons are termed as "wavelon"s.). The main advantage of WNNs with respect to the standard NNs is that they converge faster. Moreover, employing concepts from MRA, WNNs are able to mimic dynamic system behaviour with very high performance when used in recurrent form as given in Fig. 4.2. Such a neural network is literally termed as a "Self-Recurrent Wavelet Neural Network" (SRWNN).

4.1.1 Indirect Adaptive Controller Employing SRWNNs

The SRWNN structure used in this study was proposed in [60]. As seen in Fig. 4.3 this structure consists of mainly four layers:

- Layer 1: The input layer. It consists of N_i nodes representing inputs to the SR-

WNN.

- Layer 2: The mother wavelet layer. It consists of N_w wavelon groups each having N_i wavelons corresponding to every element of the input vector of the SRWNN. i^{th} wavelon of the j^{th} wavelon group performs the following calculation

$$\phi_{jk}(z_{jk}) = \phi\left(\frac{u_{jk} - m_{jk}}{d_{jk}}\right) \quad (4.4)$$

where

$$z_{jk} = \frac{u_{jk} - m_{jk}}{d_{jk}}, u_{jk}(n) = x_k(n) + \phi_{jk}(n-1)\theta_{jk} \quad (4.5)$$

In (4.4) and (4.5), x_k denotes the k^{th} element of the input vector; m_{jk} , d_{jk} and θ_{jk} denote the translation, dilation and feedback gain of the wavelon jk , respectively.

- Layer 3: The product layer. It consists of N_w product elements. j^{th} product element merges the corresponding mother wavelet group activation as

$$\Phi_j(x) = \prod_{k=1}^{N_i} \phi(z_{jk}) \quad (4.6)$$

- Layer 4: The output layer: Consists of a summer and calculates the output as

$$y = \sum_{j=1}^{N_w} w_j \Phi_j(x) + \sum_{k=1}^{N_i} a_k x_k \quad (4.7)$$

where w_j is the weight of the j^{th} wavelon group, and a_k is the weight of the k^{th} input vector element. Note that, in (4.7) the second sum denotes a linear component between the input and the output, which behaves similar to a proportional controller. In [88] this linear component is not used, but the SRWNN itself replaces the proportional part of a PID controller.

4.1.2 Modified Adaptive Learning Rates (MALR)

The SRWNN structure given in Fig. 4.3 is an adaptive structure, whose weight vector is defined as

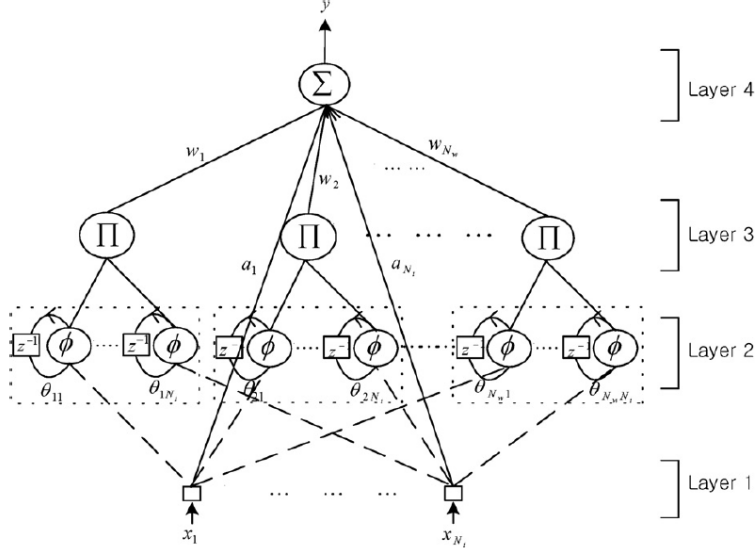


Figure 4.3: SRWNN internal structure proposed in [60]

$$\vec{W} = [\vec{a} \quad \vec{m} \quad \vec{d} \quad \vec{\theta} \quad \vec{w}] \quad (4.8)$$

\vec{W} is adapted according to the gradient descent algorithm, which is described by

$$\vec{W}(n+1) = \vec{W}(n) - \bar{\eta} \vec{\nabla}_W J \quad (4.9)$$

where $\bar{\eta}$ is the diagonal matrix of learning rates, $\bar{\eta} = \text{diag}(\eta^a, \eta^m, \eta^d, \eta^\theta, \eta^w)$, and $\vec{\nabla}_W J$ denotes the gradient of the cost function J with respect to the weights vector \vec{W} . Cost function is usually quadratic and it's in the form

$$J(n) = \frac{1}{2} [y_d(n) - y(n)]^2 = \frac{1}{2} e^2(n) \quad (4.10)$$

where $y_d(n)$ is the desired output at time step n . The above definition of cost function results in

$$\vec{\nabla}_W J = -e(n) \vec{\nabla}_W y \quad (4.11)$$

where the term $\vec{\nabla}_W y$ can be easily evaluated by applying the chain rule for each weight vector entry as given in [60]:

$$\frac{\partial y(n)}{\partial a_k(n)} = x_k \quad (4.12)$$

$$\frac{\partial y(n)}{\partial m_{jk}(n)} = -\frac{w_j}{d_{jk}} \frac{\partial \Phi_j(x)}{\partial z_{jk}} \quad (4.13)$$

$$\frac{\partial y(n)}{\partial d_{jk}(n)} = -\frac{w_j}{d_{jk}} z_{jk} \frac{\partial \Phi_j(x)}{\partial z_{jk}} \quad (4.14)$$

$$\frac{\partial y(n)}{\partial \theta_{jk}(n)} = \frac{w_j}{d_{jk}} \phi_{jk}(n-1) \frac{\partial \Phi_j(x)}{\partial z_{jk}} \quad (4.15)$$

$$\frac{\partial y_I(n)}{\partial w_j(n)} = \Phi_j(x) \quad (4.16)$$

one can evaluate the partial derivative of $\Phi_j(x)$ w.r.t. z_{jk} using chain rule as:

$$\frac{\partial \Phi_j(x)}{\partial z_{jk}} = \phi(z_{j1}) \phi(z_{j2}) \dots \dot{\phi}(z_{jk}) \dots \phi(z_{jN_i}) \quad (4.17)$$

and with simple differentiation of the Gaussian derivative wavelet as:

$$\dot{\phi}(z_{jk}) = (z_{jk}^2 - 1) e^{-\frac{1}{2} z_{jk}^2} \quad (4.18)$$

A set of adaptive upper bounds for learning rates have been proposed in [60] as follows:

$$\eta^a = \frac{1}{N_i |x_{I,max}|^2} \quad (4.19)$$

$$\eta^m = \eta^\theta = \frac{1}{N_i N_w} \left[\frac{1}{|w_{I,max}| \frac{2e^{-0.5}}{|d_{I,min}|}} \right]^2 \quad (4.20)$$

$$\eta^d = \frac{1}{N_i N_w} \left[\frac{1}{|w_{I,max}| \frac{2e^{0.5}}{|d_{I,min}|}} \right]^2 \quad (4.21)$$

$$\eta^w = \frac{1}{N_w} \quad (4.22)$$

where η represents the learning rate and its superscript represents the related adaptive parameter. However, the approach employed in evaluating these learning rates is based on Lyapunov stability theory and they guarantee the convergence of SRWNN at all times, rather than optimizing the speed of convergence. The following idea is employed to modify the learning rates in a different manner, in order to optimize the speed of convergence of error:

If we denote the system output as $y(n)$ and the identifier output as $y_I(n)$, one can write the identification error as

$$e(n) = y(n) - y_I(n) \quad (4.23)$$

in discrete-time, assuming the dynamics of the plant output y is much slower than that of the identifier output, y_I (the identifier designed should catch the bandwidth of the plant), i.e.

$$|y(n+1) - y(n)| \ll |y_I(n+1) - y_I(n)| \quad (4.24)$$

one can write

$$e(n+1) - e(n) = (y(n+1) - y(n)) - (y_I(n+1) - y_I(n)) \approx -(y_I(n+1) - y_I(n)) \quad (4.25)$$

If the identifier output error dynamics is considered in terms of the weight vector, one has:

$$\Delta e_I = \left[\frac{\partial e_I}{\partial W} \right]^T \Delta W(n) \quad (4.26)$$

For the change in weights, the following expression can be employed

$$\Delta W(n) = -\eta_I \frac{\partial J_I}{\partial W} = \eta_I \frac{\partial y_I}{\partial W} \quad (4.27)$$

and for the gradient of the error w.r.t the weights, one can write:

$$\vec{\nabla}_W e^T = -\left[\frac{\partial y_I}{\partial W}\right]^T \quad (4.28)$$

Combining the above expressions yields:

$$\Delta e_I(n) = -\eta_I e_I \left\| \frac{\partial y_I}{\partial W} \right\|^2 \quad (4.29)$$

Hence, we can control the change in the error using the learning rate η_I . Our aim is to make $e_I(n+1) = 0$, as in the case of a dead-beat controller -i.e. optimum transient performance. For this purpose, one should select

$$\Delta e_I(n) = -\eta_I e_I \left\| \frac{\partial y_I}{\partial W} \right\|^2 = e_I(n+1) - e_I(n) = -e_I(n) \quad (4.30)$$

yielding

$$\eta_I = \frac{1}{\left\| \frac{\partial y_I}{\partial W} \right\|^2} \quad (4.31)$$

This evaluation gives the approximate learning rate on the immediate convergence of the error to zero, not taking the stability into consideration. On the other hand, as error approaches to zero, main concern becomes the stability of the system and hence one should stick to Lyapunov theory results and use η^* as proposed in [60].

In conclusion the adaptive learning rates algorithm may be modified to have a better transient performance, as below:

$$\eta(n) = \begin{cases} \eta^*, & \text{if } n > n^* \\ \eta_I, & \text{if } n < n^* \end{cases} \quad (4.32)$$

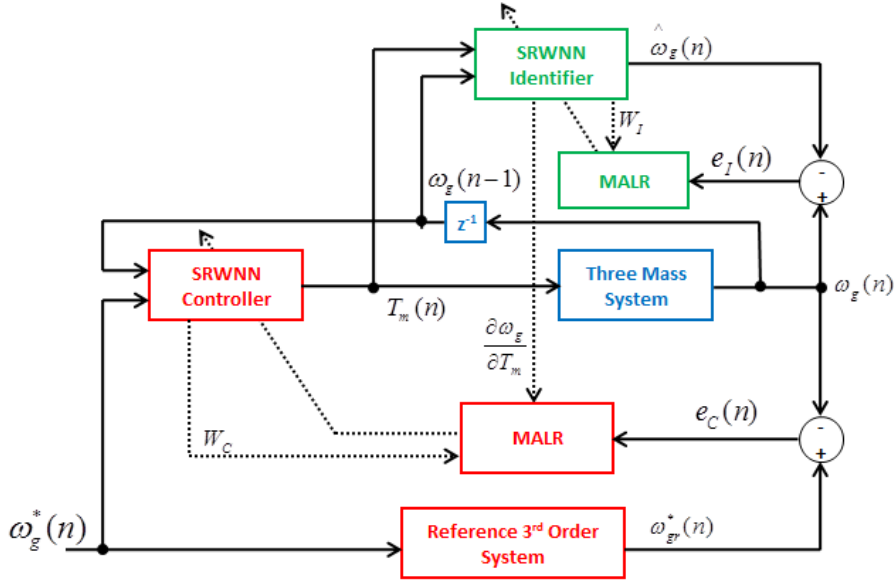


Figure 4.4: SRWNN based iterative adaptive controller (SRWNN IAC) structure similar to the one in [69].

where η^* is the adaptive learning rate, calculated as in [60], guaranteeing Lyapunov stability. In words, at the beginning of the adaptation process, by keeping higher learning rates, the process of learning is accelerated. The value n^* is determined by observing the convergence of error to 0. This learning rate update mechanism is termed as the Modified Adaptive Learning Rates (MALR) throughout this study.

4.1.3 Control Architecture

SRWNN structure has been used in various architectures for control purpose. These include a predictive controller ([60]), an indirect adaptive controller ([69]), and the proportional part of a standard PID controller([88]). In this study, the indirect adaptive control architecture ([69]) with modified learning rates update algorithm is used. The general structure of indirect adaptive control employing SRWNN-MALR components is shown in Fig. 4.4. As seen in this figure, there are two MALR structures along with two SRWNN structures: One being employed as the controller and other as the identifier.

Most of the studies based on model-reference control (e.q. [68]) use a second order linear system model as the reference for the closed-loop. However, one should keep in

mind that even in a linear pole-placement approach, for the controller to be realizable, the pole excess of the closed-loop system must be larger than or equal to the pole excess of the plant itself. If the simple three-mass linear system model is considered, it is seen that the plant has 3 excessive poles. Hence, in this study a reference model with three excessive poles is employed. If one puts triple poles to a frequency higher than the anti-resonance (see Fig. 3.20), and sets the DC gain to unity by adding a constant to the numerator, the following reference model is obtained:

$$G_R(s) = \frac{60^3}{(s + 60)^3} \quad (4.33)$$

Another issue in this control architecture is that the gradient given in (4.11) cannot be used directly because we have the cost function given as

$$J(n) = \frac{1}{2}[\omega_{gr}^*(n) - \omega_g(n)]^2 = \frac{1}{2}e_C^2(n) \quad (4.34)$$

and ω_g is not a direct output of the SRWNN. By applying the chain rule, one can write

$$\vec{\nabla}_W J = -e_C(n) \frac{\partial \omega_g}{\partial T_m} \vec{\nabla}_W T_m \quad (4.35)$$

where the $\vec{\nabla}_W T_m$ term can be easily found using the chain rule, as stated before. However, the sensitivity term given by $\frac{\partial \omega_g}{\partial T_m}$ cannot be calculated directly. For this purpose the approach given in [69] is utilized and an SRWNN identifier is incorporated into the architecture, for which the term $\frac{\partial \omega_g}{\partial T_m}$ can be calculated easily by utilising the chain rule (see Fig. 4.4 and [69] for details).

4.2 Simulations

During simulations the three-mass system linear model is employed as the plant. A speed command (in the form of unit step) reference has been applied to the system. SRWNN structures with $N_w = 4$ has been utilized for both the identifier and the controller. The results for the step response is shown in Fig. 4.5. In this figure, it is seen that when the SRWNN IAC is utilized with the standard adaptive learning algorithm,

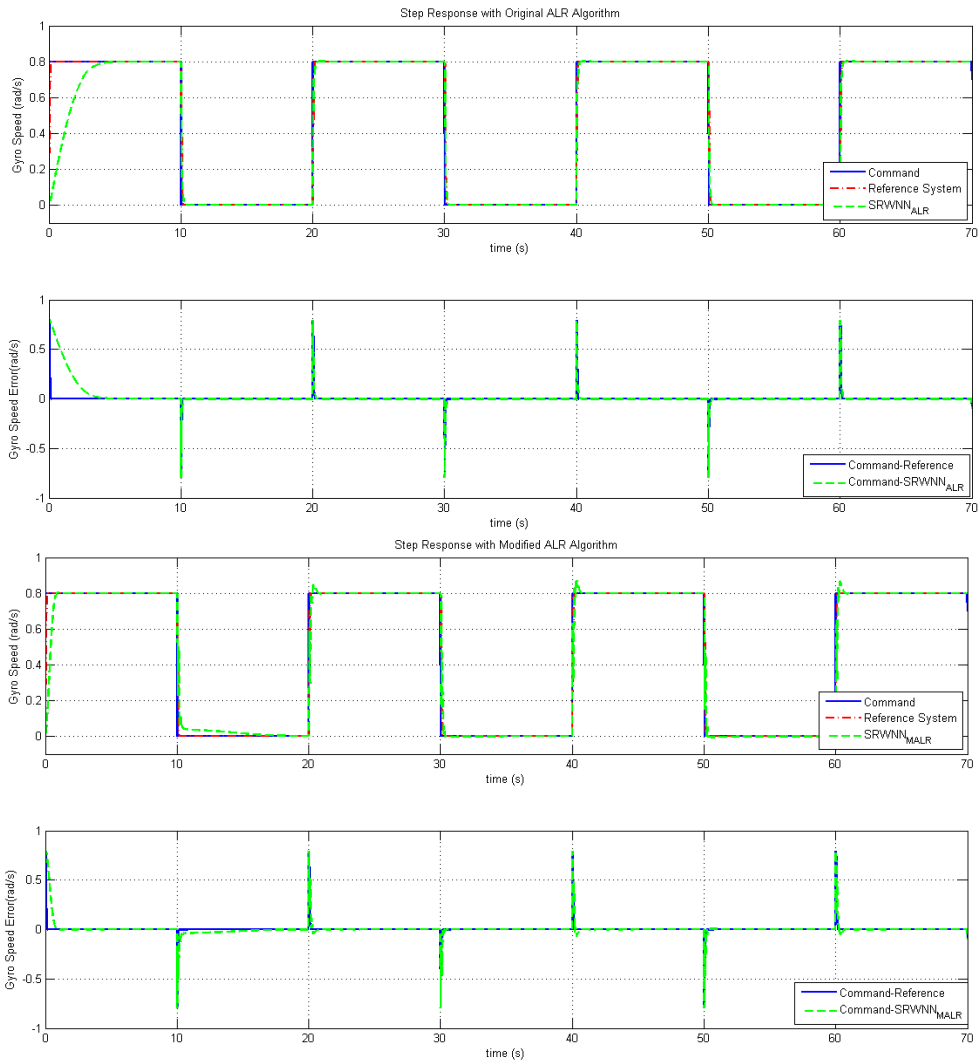


Figure 4.5: Step Response with the original ALR algorithm (Top two plots) and the Modified ALR algorithm (bottom two plots).

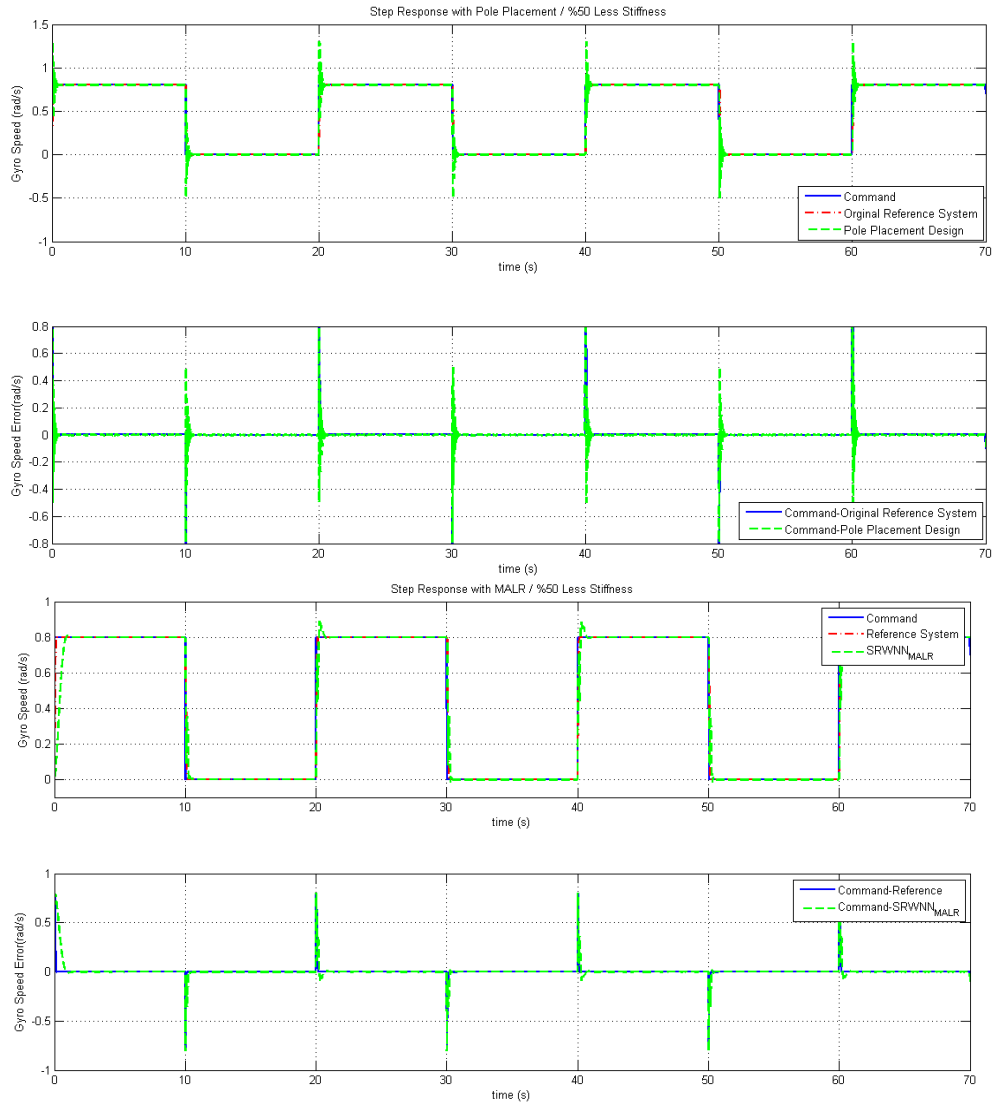


Figure 4.6: Step Response when stiffness values are reduced by 50%. The Truxal-Guillemain design(Top two plots) and SRWNN IAC (bottom two plots).

it takes around 4 seconds for the system to follow the command. But with the modified learning rate algorithm it takes about 0.5 seconds. The robustness performance of the SRWNN IAC is tested by reducing the stiffness values by a factor of 0.5 during the simulation. As expected, the pole placement (Truxal-Guillemin) design shows under damped oscillatory behavior; while SRWNN IAC controller adapts itself equally well to the new stiffness values as given in Fig. 4.6.

4.3 Experiments

During the experiments an SRWNN structure with $N_w = 4$ has been employed for both identifier and the controller parts, as in the simulations. With 2 inputs for the SRWNN, this sums up to a total of 30 learning parameters for both SRWNN structures. The comparison between the ALR and the proposed MALR learning rate updates are given in Fig. 4.8. It is easily observed that the SRWNNI converges to the system output at about 2.2 seconds for ALR, and 1.05 seconds for the MALR case. Note also from the same figure that the system is quite non-linear (producing a non-exponential speed output for a square torque input, and the response is different at each step cycle), however SRWNNI structure is complicated enough to capture these non-linearities and find the system sensitivity correctly. The performance of the controller is compared with a high performance PI speed controller as well. The PI controller is tuned so as to have a gain margin of only 2 dBs, making it non-robust, but with a stiff, high command tracking performance. As seen in Fig. 4.9 the SRWNN adaptive controller structure outperforms the high performance PI controller in step response, and it almost makes the overall system mimic the reference system behaviour. To make a few comments: The SRWNN controller saturates the motor torque very rapidly in the case of a step command and uses all the available acceleration of the system in an efficient way; hence using the torque loop bandwidth much more better than the PI controller. One can also state that the main reason for the SRWNN IAC cannot do better in making the system mimic the 3rd order reference system is the actuator saturation (note that the p.u. torque demand saturates to 1 immediately for the SRWNN IAC case).

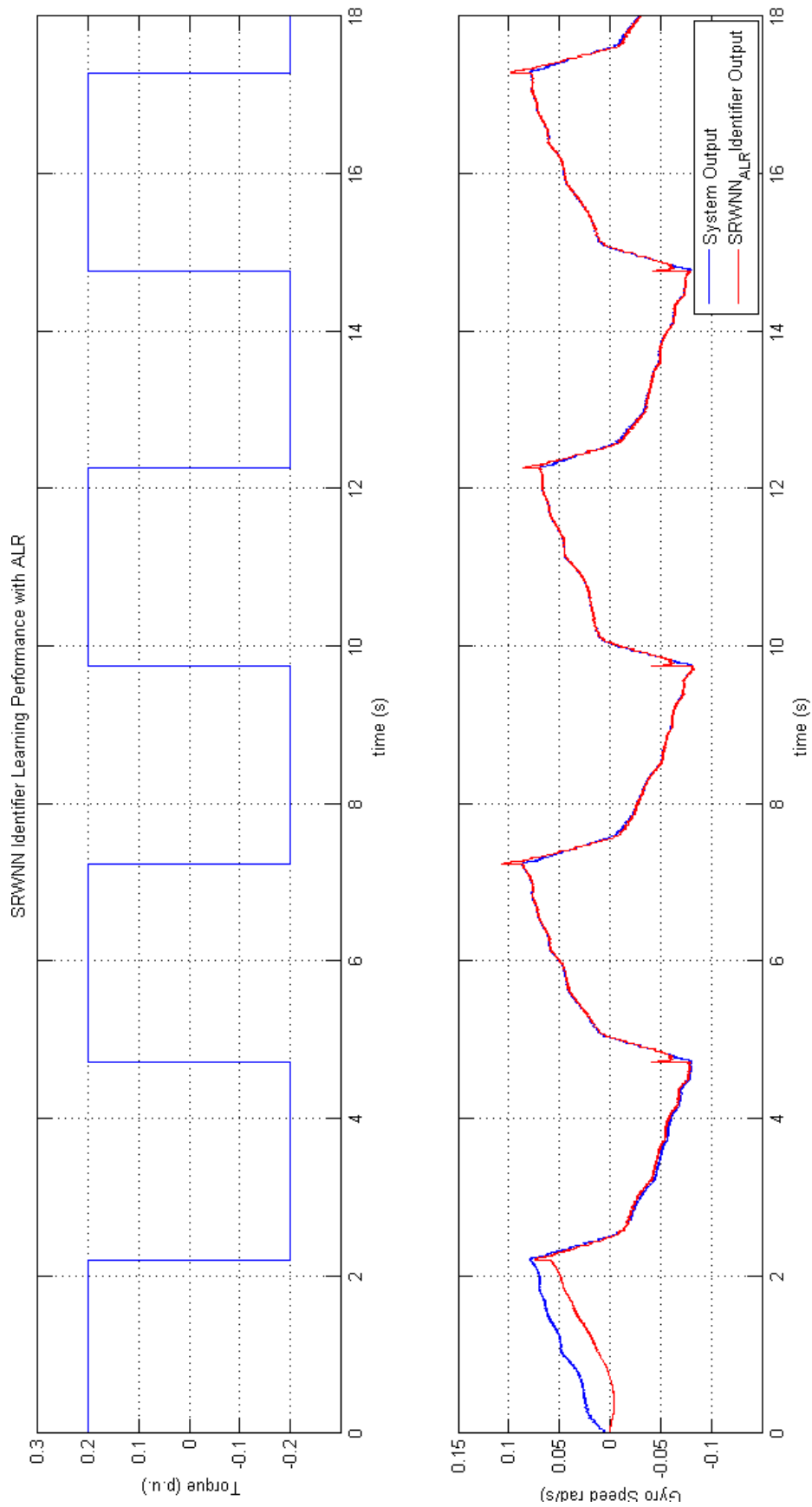


Figure 4.7: Experimental result showing the convergence performance of the SRWNN identifier with ALR.

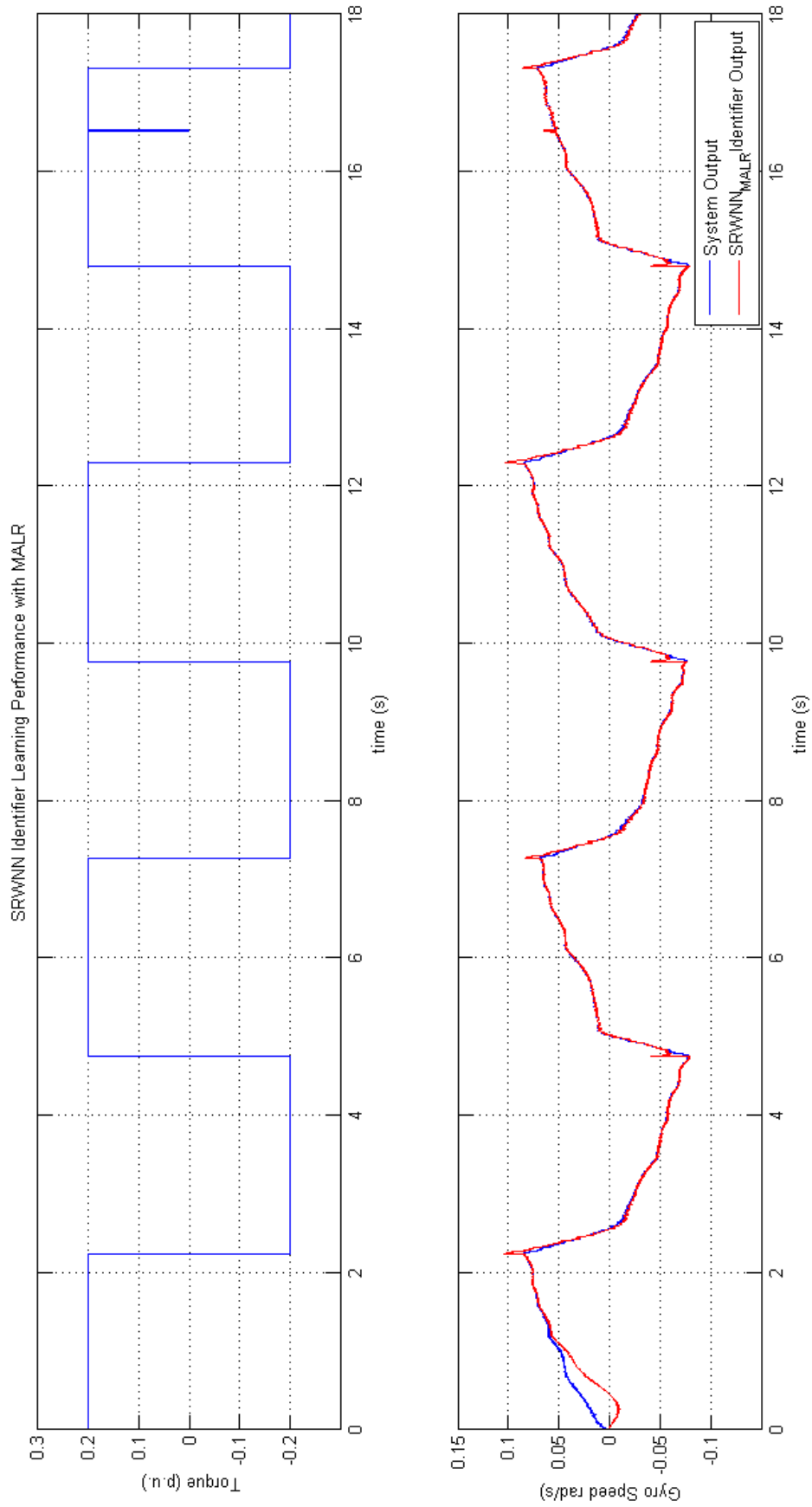


Figure 4.8: Experimental result showing the convergence performance of the SRWNN identifier with MALR.

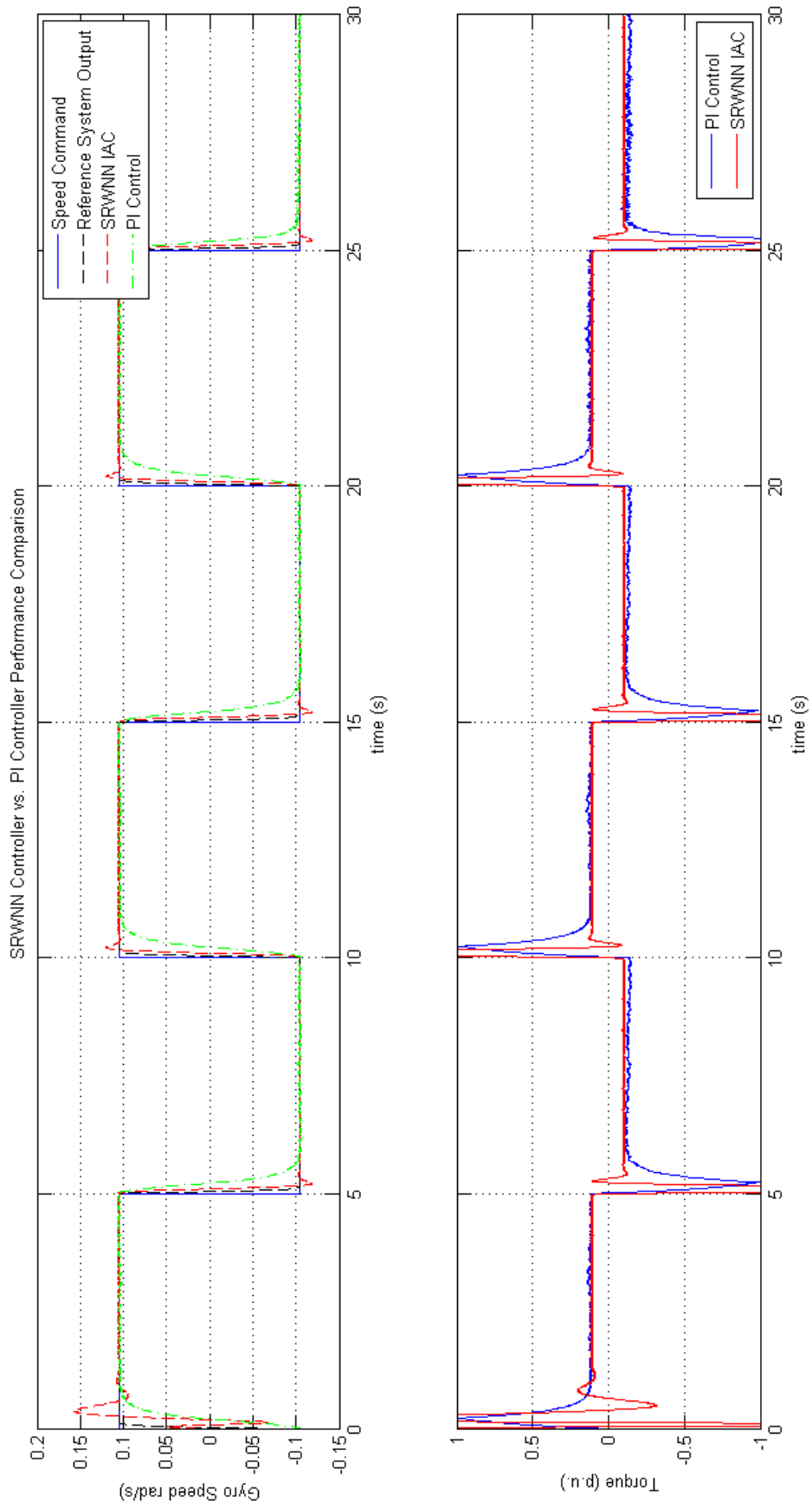


Figure 4.9: Experimental results for the comparison of proposed SRWNN IAC and high performance PI controller.

4.4 Performance Comparison with Robust Control Designs on a Benchmark System

As the performance of the proposed architecture has been verified with simulations and experiments; it is further compared with RST robust designs for a similar system. In European Control Conference of the year 1995, a benchmark system has been proposed to be controlled using the robust control design [33] for discrete-time RST control. This benchmark problem is basically a three-mass system with elastic couplings; which is very similar to the system considered in this study. A schematic describing the system is given in Fig. 4.10. Here, the aim is to control the third mass position, Φ_m by controlling the first mass position Φ_1 . Despite it has different input and output (when compared with the problem considered in this study), the basic challenge of keeping the system robust while providing high performance input-output response has similar difficulties, i.e. dealing with mechanical resonances and anti-resonances. Moreover, there exist several controller designs whose performance has been evaluated using this system, which can be compared with the proposed technique. Hence, this system is taken as a simulation playground to test the proposed control architecture performance and compare it with the originally proposed robust designs.

The following discrete-time system model has been provided as a plant model, after an identification procedure [33]

$$H(z^{-1}) = z^{-d} \frac{B(z^{-1})}{A(z^{-1})} \quad (4.36)$$

where z^{-1} is the unit delay operator, d is a fixed number representing transport delay. with a sampling time of $5ms$ (i.e. $20Hz$ sampling frequency), the following polynomials are provided for different configurations of the load:

Unloaded Case:

$$A(z^{-1}) = 1 - 1.41833z^{-1} + 1.58939z^{-2} - 1.31608z^{-3} + 0.88642z^{-4} \quad (4.37)$$

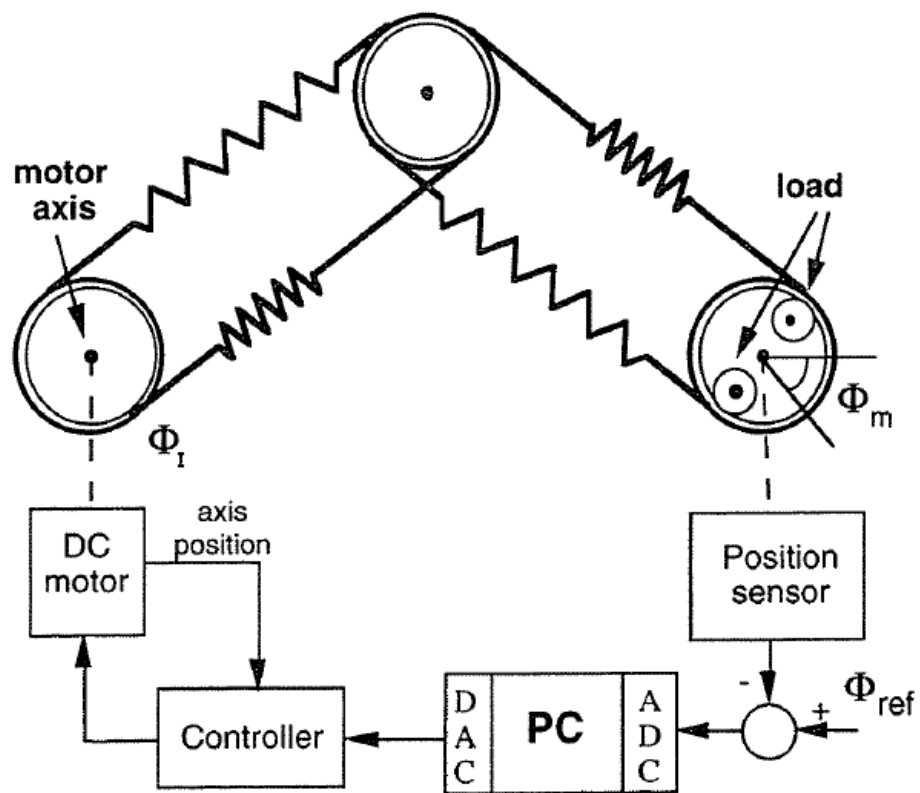


Figure 4.10: The schematic and block diagrams showing the structure of the benchmark three mass system ([33])

$$B(z^{-1}) = 0.28261z^{-1} + 0.50666z^{-2} \quad (4.38)$$

Half-loaded Case:

$$A(z^{-1}) = 1 - 1.99185z^{-1} + 2.20265z^{-2} - 1.84083z^{-3} + 0.89413z^{-4} \quad (4.39)$$

$$B(z^{-1}) = 0.10276z^{-1} + 0.18123z^{-2} \quad (4.40)$$

Full-loaded Case:

$$A(z^{-1}) = 1 - 2.209679z^{-1} + 2.31962z^{-2} - 1.93353z^{-3} + 0.87129z^{-4} \quad (4.41)$$

$$B(z^{-1}) = 0.06408z^{-1} + 0.10407z^{-2} \quad (4.42)$$

For every model the transport delay parameter d is provided as 2.

The frequency response plots for these discrete-time transfer functions are provided in Fig. 4.11. As seen in this figure, the gain margins for all three configurations are much less than 1, and it is not easy to control such a system with high performance using linear control techniques, at least in a robust manner.

Several (eight) designs have been performed by different engineering research teams and the performance results have been published in ECC '95 along with the comparison in [33]. When one investigates the designs and their comparison, the following drawbacks are obvious:

- The best performing controller is based on Quantitative Feedback Theory (QFT). The design procedure maps the performance criteria into frequency domain parameters and solves for three polynomials resulting in two 9th order and one 2nd order polynomials. Once the coefficients of these polynomials are determined, no adaptation is possible.

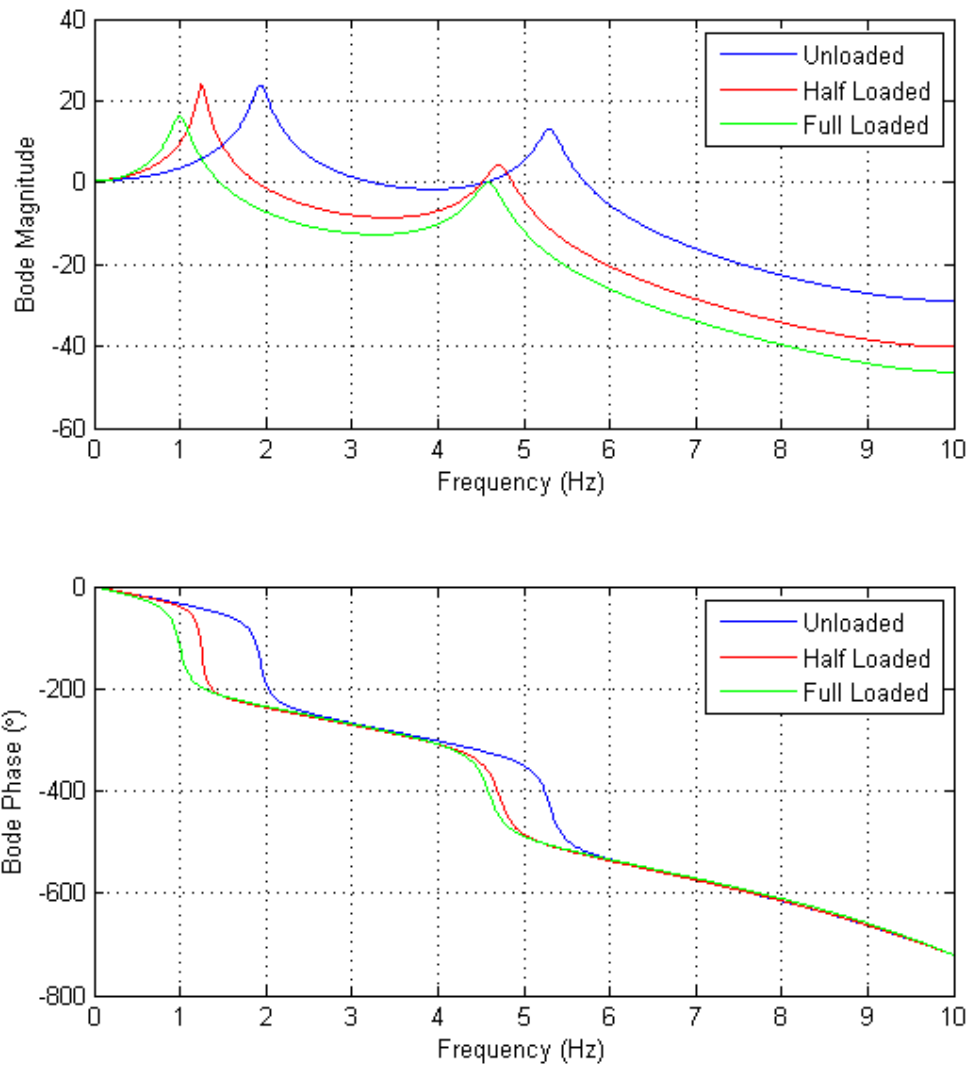


Figure 4.11: Frequency Response Functions of the benchmark system in [33].

Table 4.1: Performance Comparison on Benchmark System Control

Perf. Measure	Method	No Load	Half Load	Full Load
Rise Time (s)	RST - Robust	0.813	0.598	0.660
	IAC SRWNN-MALR	0.28	0.31	0.31
Overshoot (%)	RST - Robust	0.26	0.89	9.27
	IAC SRWNN-MALR	0	0	0
Settling Time (s)	RST - Robust	1.667	1.961	1.923
	IAC SRWNN-MALR	0.58	0.62	0.62

- During the design of the best performing controller, actually manual tuning of parameters has been employed. The tuning process was made easy by performing iterations via MATLAB scripts; nevertheless, the designer selects some loop parameters by visual inspection of the expected frequency response.
- While comparing the performance for different designs on the same experimental setup, the experimental setup parameters were different than the ones utilised for the design of the controllers. This caused a significant decrease in the performance values, as the controller designs were robust but not adaptive, hence a re-tuning was necessary before practical implementation.

Sample simulation responses for the unloaded case of the benchmark system with the proposed control architecture are given in Fig. 4.12 and Fig. 4.13. The first figure shows the performance of the identifier with identification error converging to zero. The second figure shows the performance of the controller, starting with an under-damped response and adapting quickly to a fast and over-damped closed-loop response. As seen in these figures, SRWNN-IAC with MALR can be used to control the given three mass system with high performance.

The comparison of the SRWNN-IAC with MALR and the designs given in [33] is given in Table 4.1. It is easily seen in this table that the proposed architecture outperforms the best performing robust design.

Having shown that the performance of the proposed controller is quite well as compared to classical robust control designs, an issue to address is the automatic determi-

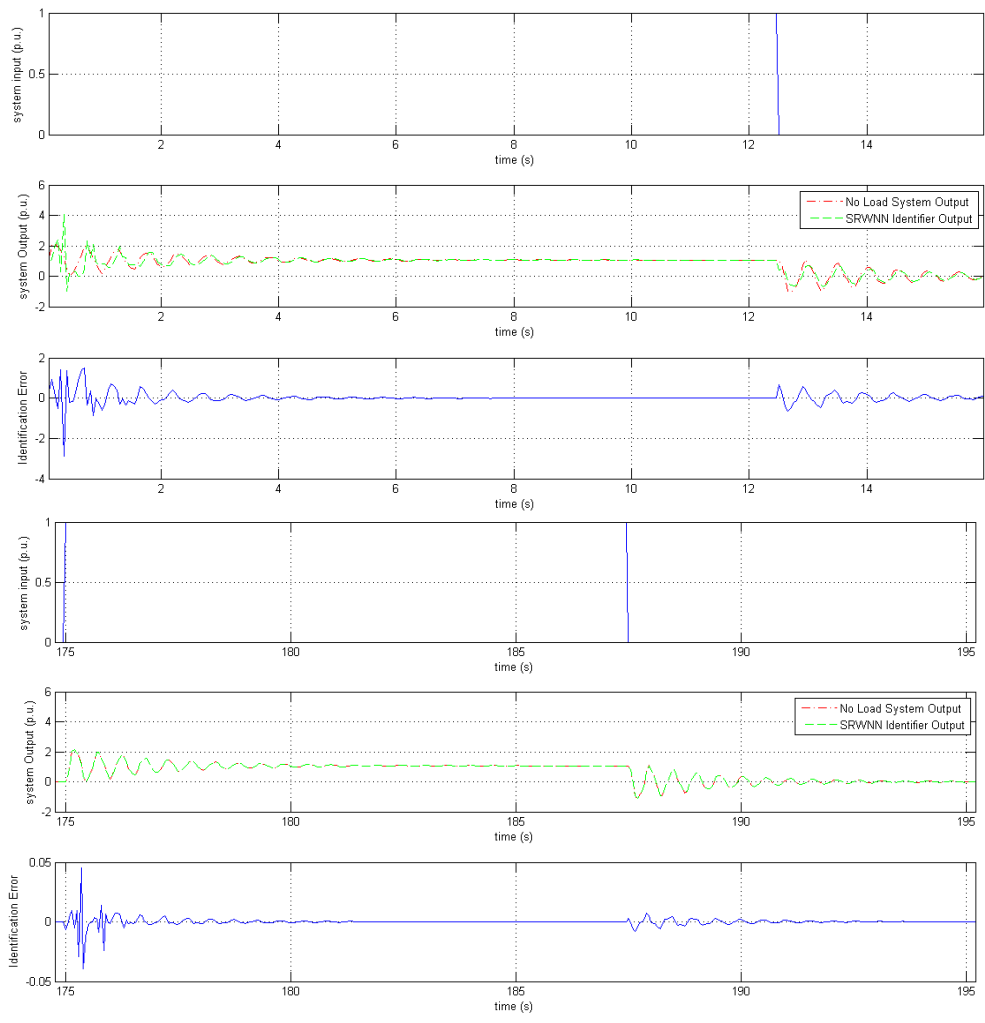


Figure 4.12: Performance of the SRWNN identifier for the un-loaded benchmark system in [33]. Initial (top 3 plots) and steady-state (bottom 3 plots)

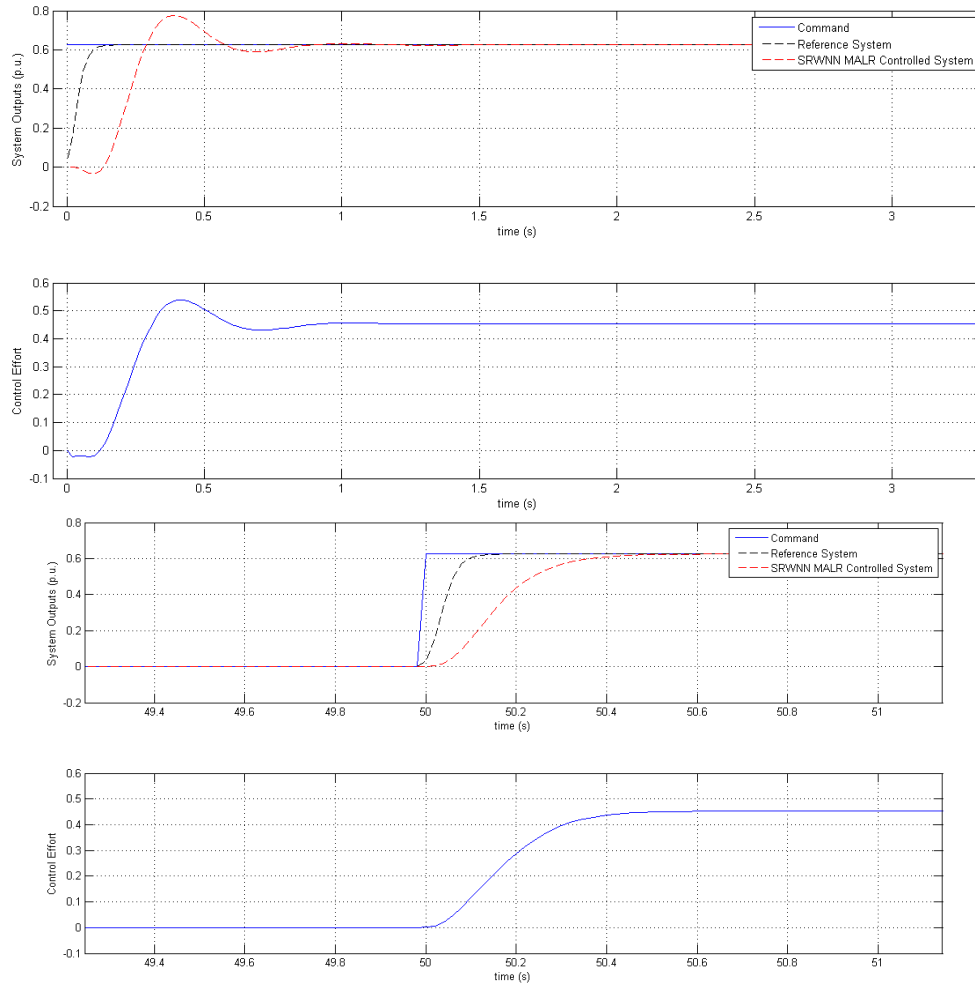


Figure 4.13: Step Response for the un-loaded benchmark system utilising SRWNN-MALR IAC. Initial (top 2 plots) and steady-state (bottom 2 plots).

nation of the complexity of the proposed controller, which corresponds to "structural learning" or "self-evolution". Next section is dedicated to a method proposed for this purpose.

4.5 Automatic Determination of the Network Complexity - Self Evolution

Since the early times of neural networks, automatic construction of the network structure has been a concern. For this purpose, a variety of approaches have been developed: For feed-forward neural networks used for function mapping, the evolutionary algorithms basically employ input space coverage measures (clustering, similarity measures etc.) ([42], [55]). For the neural networks used for control purposes, the structural learning algorithms are embedded into fuzzy rules, and the number of fuzzy rules ([70], [89] etc.) are adjusted using either the input space clustering or fuzzy rule firing strength thresholds.

For recurrent neural networks, the structural learning is based on genetic algorithms or reinforcement learning ([71]) which are not suitable for on-line purposes.

In our earlier studies, the utilized neural-network's complexity was determined manually, via the knowledge of a human expert. However, determination of the network complexity via trial and error makes it hard for the engineer to design and commission the final controller. As a remedy to this problem, the following algorithm to construct the neural network from scratch, while performing parameter learning in the mean-time is proposed:

1. Initialize the SRWNN structure with $N_w(0) = 1$.
2. Run the network and find $\Phi_i, i = 1, \dots, N_w$.
3. Run the network parameter updates.
4. if $\Phi_{max} = \max\{\Phi_i\} > \Phi_{th}$ (see below) then go to step-(2), else continue execution
5. Set $N_w(k + 1) = N_w(k) + 1$

6. Initialize the new wavelet parameters such that $d_{hN_w} = x_h(k)$ ($h = 1, \dots, N_i$) and assign other wavelet and connection parameters using the standard network initialization.
7. Go to step-(2).

In this algorithm, Φ_{th} determines the speed of complexity update of the neural network. Using a small value will cause a redundantly complex network while a big value will lead to an under-determining structure. Hence, a wise selection of this parameter is important for the sake of the evolution algorithm. For assigning Φ_{th} , the following equation is proposed:

$$\Phi_{th} = \frac{1}{N_i + 1} \prod_{k=1}^{N_i} \phi_{max} \quad (4.43)$$

where ϕ_{max} represents the maximum value of the wavelet function being employed (it is 0.6065 for the Gaussian derivative wavelet). This heuristic threshold corresponds to a fraction of the maximum possible wavelet activation. As the number of inputs (N_i) is increased Φ_{th} is lowered to make wavelet evolution faster. A sample result for the proposed self-evolving structure from the identifier of the un-loaded benchmark system is shown in Fig. 4.14 . As seen in this figure, the N_w parameter is determined automatically and it converges to 8. Note also that, as the proposed algorithm includes 1 mathematical comparison, 1 mathematical assignment and 3 random number generation steps only, it is suitable for running on-line.

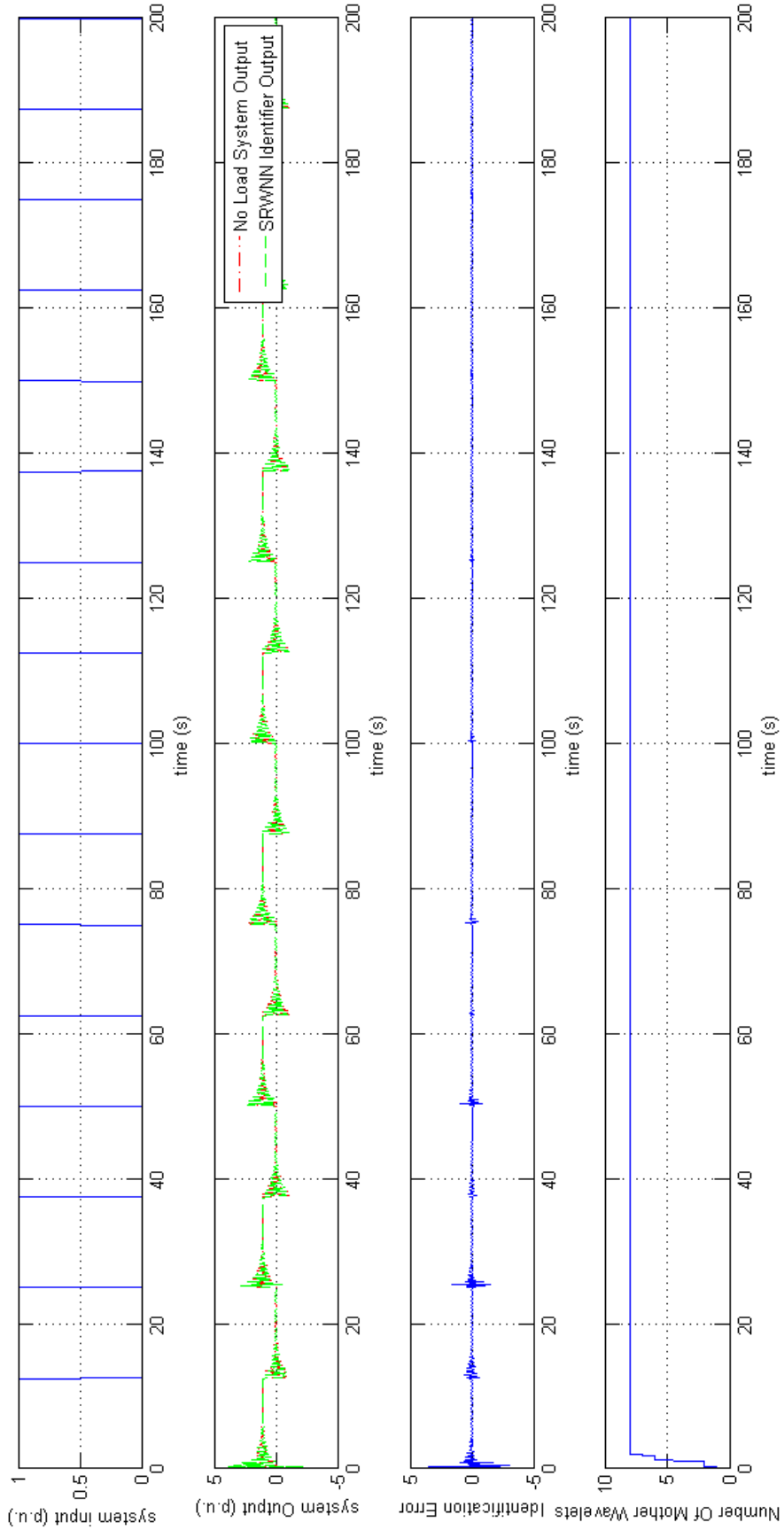


Figure 4.14: A Simulation showing the result of the evolutionary algorithm for the identifier during un-loaded benchmark system identification simulations.

4.6 Contributions

The problem of controlling the speed of a motion platform has been addressed. An SRWNN based controller architecture with modified adaptive learning rates for fast convergence has been proposed for providing a fast settling step response while preserving robustness and stability. High performance of the proposed architecture has been verified by both computer simulations and experiments conducted at ASELSAN facilities. Moreover, the effectiveness of the architecture with proposed modification has been proven with simulations on a benchmark system, over-performing the original robust RST designs. Finally, a structure learning algorithm for automatic determination of network complexity has been proposed and its performance has been verified via simulations on the benchmark three mass mechanical system.

CHAPTER 5

CONCLUSION

In conclusion, the speed control problem of a motion platform has been addressed in this study. First of all, some modelling and experiment effort has been performed in order to divide the problem to its sub-problems. During this process, it has been observed that the problem can be seen as a combination of "brushless AC motor current control", "suppression of non-linear effects like friction and backlash", and "control of a three-mass system connected with elastic elements". The first sub-problem has been investigated briefly and it was found that the bandwidth of the current control is high enough and any more improvements would not improve the overall performance. Moreover, with a modelling and experimental study it was shown that the motor current loop can be tuned independent of the mechanical components of the motion platform [85]. The second sub-problem (i.e. suppression of non-linear effects like friction and backlash) has also been investigated briefly and it was seen that modelling friction and backlash explicitly is usually very complicated. Moreover, controllers using such models do usually have complicated structures and are non-robust in general and they can be worked out with careful mechanical design or other methods before starting the controller design. In addition to this, during the literature survey, it was seen that using black-box models for the non-linear effects is a handy approach for the suppression of such non-idealities. Finally, the problem of controlling the speed of the second mass in an elastically connected three mass system has been addressed broadly. Several experiments have been performed on a real system, showing that the motion platform might be modelled as a three-mass linear system connected with elastic elements, whose behaviour changes with the amount of input torque. In other words, it is actually a non-linear system, but as long as one knows

about "the input sensitivity" of the system (i.e. the temporal dynamic behaviour), it might be controlled effectively. After the literature survey showing that linear controllers give limited performance both due to robustness performance and ineffective utilisation of the actuator (i.e. transient performance), it was decided to work on adaptive controllers employing black-box models. At this point, a Self-Recurrent Wavelet Neural Network (SRWNN) based controller architecture with adaptive learning rates has been found very effective for the solution of the problem so as to achieve a robust performance, while increasing the system bandwidth beyond the anti-resonance frequency of the open-loop system. The learning rate update algorithm of the original approach ([69]) has been modified to achieve a better convergence rate. High performance of the modified controller has been verified by both simulations and experiments. In addition to this, the effectiveness of the control architecture with proposed modification has been also compared with several robust RST designs evaluated on a three mass benchmark system ([33]), over-performing the original robust RST designs. Finally, an evolutionary algorithm in order to decide the complexity of the network has also been proposed and its performance was also tested with simulations on the benchmark system. A possible future work for this study is utilisation of the proposed approach on different motion platforms and optimization of the real-time implementation, in order to be able to append the proposed controller algorithm to a processor which is already being utilised for other purposes.

REFERENCES

- [1] K.S. Narendra, L.S. Valavani Stable Adaptive Observers and Controllers. *Proceedings of the IEEE*, vol. 64, No 8, pages 1198–1208, August 1976.
- [2] K.S. Narendra, L.S. Valavani Stable Adaptive Controller Design-Direct Control *IEEE Transactions on Automatic Control*, vol. AC-23, No 4, pages 570–583, August 1978.
- [3] T.R. Perkins, J.H. Groff Enhanced Armored Vehicle Fire Control System Design Modifications. *American Control Conference*, pages 841–846, 1986.
- [4] T.R. Perkins, J.H. Groff Further Studies on the Enhancement of Armored Vehicle Fire Control System Design. *American Control Conference*, pages 745–750, 1987.
- [5] K.J. Åström Adaptive Feedback Control. *Proceedings of the IEEE*, vol. 75, No 2, pages 185–217, February 1987.
- [6] J. Lyou Adaptive Controller Yielding Fast Convergence Rate. *Electronic Letters*, vol. 24, No 8, pages 465–466, April 1988.
- [7] H. Kang, G. Vachtsevanos, F. L. Lewis Structural Convergence Improvement Schemes on Adaptive Control. *Proceedings of the 27th Conference on Decision and Control*, vol. 24, No 8, pages 1941–1944, Texas, December 1988.
- [8] S.V. Rao, S.M. Mattice, N.P. Coleman Design of Reduced Order LQG/LTR Controllers for Turret-Gun System. *American Control Conference*, pages 312–315, 1989.
- [9] Goldberg, D. E. Genetic Algorithms in Search, Optimization and Machine Learning. Addison-Wesley Publishing, 1989.
- [10] S. Shah, R.L. Kosut Control of Articulated Structures on Maneuvering Platforms. *American Control Conference*, pages 33–38, 1990.
- [11] M. Hashimoto et. al., "Experimental Study on Torque Control Using Harmonic Drive Built-in Torque Sensors", Proceedings of ICRA, Nice, France, pp. 2026-2031, 1992.
- [12] B.E. Ydstie Transient Performance and Robustness of Direct Adaptive Control. *IEEE Transactions on Automatic Control*, vol. 37, No 8, pages 1091–1105, August 1992.

- [13] Y.L. Gu et. al. , "Control of Weapon Pointing Systems Based on Robotic Formulation", American Control Conference, pp. 413-419, 1992.
- [14] W. Chai et al., "Robust Digital Control of Gun-Turret Systems", American Control Conference, pp. 419-423, 1992.
- [15] N. Coleman, M. Mattice, S. Banks, "High Precision Weapon Control System Design", Proceedings of ICRA, Nice, France, pp. 726-731, 1992.
- [16] R. Dana, E. Kreindler, "Variable Structure Control of a Tank Gun", Proceedings of the American Control Conference, pp. 928-933, 1992.
- [17] S.V. Rao, S.M. Mattice, N.P. Coleman Reduced Order Modeling Techniques for Turret-Gun System. *American Control Conference*, pages 39–43, 1992.
- [18] S.C. Gomez et. al. "Dynamic Modeling and Friction Compensated Control of a Robot Manipulator Joint", Proceedings of ICRA, pp. 1429-1435, 1992.
- [19] J. Huang et. al. "A Nonlinear Controller for the Gun Turret System", American Control Conference ,pp. 424-428, 1992.
- [20] T.H.S. Li et. al. "Fuzzy Logic Control of Gun Turret System", American Control Conference,pp. 440-444, 1992.
- [21] J. Huang et. al. "A Nonlinear Controller for the Gun Turret System", IEEE Regional Conference on Aerospace Systems ,pp. 851-855, 1993.
- [22] Y. Hori et. al. "Basic consideration of vibration suppression and disturbance rejection control of multi-inertia system using SFLAC (state feedback and load acceleration control) ", Power Conversion Conference,pp. 309-315 1993
- [23] J.H. Taylor and J. Lu "Robust Non-linear Control System Synthesis Method for Electro-mechanical Pointing Systems with Flexible Modes", American Control Conference, pp. 424-428, 1993.
- [24] B.A. Helouvy, "Stick Slip and Control in Low-speed Motion", IEEE Transactions in Automatic Control, Vol. 38, No. 10, pp. 1483-1496, 1993.
- [25] J.L. Zhang and L.S. Shieh , "Hybrid Optimal Control of Turret-Gun System", American Control Conference, San Francisco, California, pp. 541-546, 1993.
- [26] F. Chen, M. Lin On the Learning and Convergence of the Radial Basis Networks. *International Journal of Information and Mathematical Sciences*, vol. 1, issue 3, pages 983–988, March 1993.
- [27] K. Yuki,T. Murakami,K. Ohnishi. Vibration Control of 2 Mass Resonant System by Resonance Ratio Control. *IECON'93 Proceedings*, pages 2009–2014, 1993.

- [28] R. Dhaouadi et. al. "Partial Optimal Implementation of Adaptive Resonance Theory 2", *IEEE Transactions on Neural Networks* Vol. 4, No. 4, pages 695-702, 1993.
- [29] S. Banks, N. Coleman, C.F. Lin and T.J. Yu "Advanced Integrated Control of Nonlinear Flexible Pointing Systems", *Proceedings of the American Control Conference*, vol. 2 pp. 947–952, 1994.
- [30] R. Dhaouadi et. al. "Analysis and Compensation of Speed Drive Systems with Torsional Loads", *IEEE Transactions on Industry Applications* Vol. 30, No. 3, pages 760-766, 1994.
- [31] Coleman et al. Real-Time, High-Performance, Adaptive, Robust Control System Design. *American Control Conference*, pages 500-504, 1995.
- [32] J. Ji, S. Sul. Kalman Filter and LQ Based Speed Controller for Torsional Vibration Suppression in a 2-Mass Motor Drive System. *IEEE Transactions on Industrial Electronics*, Vol. 42, No. 6, pages 564-571, 1995.
- [33] I.D. Landau et. al. A Flexible Transmission System as a Benchmark for Robust Digital Control. *European Journal of Control*, issue 1, pages 77–96, 1995.
- [34] S. Nomura, T. Murakami, K. Ohnishi Vibration Control of Multiple Mass System by Estimated Reaction Torque. *Proceedings of the 21st IEEE IECON Conference*, Vol. 2, pages 1091-1095, 1995.
- [35] Purdy D.J., Modelling and Simulation of a Weapon Control System for a Main Battle Tank, *8th US Army Symposium on Gun Dynamics*, Rhode Island, May 1996.
- [36] D.W. Novotny and T.A. Lipo, "Vector Control and Dynamics of AC Drives", New York: Oxford University Press, 1996.
- [37] G.W. Lee, F.T. Chen, "Robust Control of Manipulators Using the Computed Torque Plus H_∞ Compensation Method", *IEEE Proceedings of Control Theory Applications*, Vol. 143, No. 1, pp. 64-72, January 1996.
- [38] J.T. Teeter et. al., "A Novel Fuzzy Friction Compensation Approach to Improve the Performance of a DC Motor Control System", *IEEE Transactions on Industrial Electronics*, Vol. 43, No. 1, pp. 113-120, February 1996.
- [39] Sugiura K., Hori Y. Vibration Suppression in 2- and 3-Mass System Based on the Feedback of Imperfect Derivative of the Estimated Torsional Torque, *IEEE Transactions on Industrial Electronics*, Vol. 43, No. 1, pp 56-64, February 1996.
- [40] Nordin M., Galic J., Gurman P. "New Models for Backlash and Gear Play", *International Journal of Adaptive Control and Signal Processing*, Vol. 11, 49-63, 1997.

- [41] D. Giebler, J. Holtz, "Identification and Compensation of Gear Backlash without Output Position Sensor in High-Precision Servo Systems", Proceedings of IEEE IECON, pp. 662-666, 1998.
- [42] C.F. Juang and C.T. Lin An On-Line Self Constructing Neural Fuzzy Inference Network and Its Applications. *IEEE Transactions on Fuzzy Systems*, vol. 6, no. 1, pages 12–32, February 1998.
- [43] J.C. Goswami,A.K. Chan Fundamentals of Wavelets: Theory, Algorithms and Applications. *Wiley Series in Microwave and Optical Engineering*, 1999.
- [44] F.B. Blanco, M.W. Degner, R. D. Lorentz, "Dynamic Analysis of Current Regulators for AC Motors Using Complex Vectors", IEEE Transactions on Industry Applications, Vol. 35, No. 6, November/December 1999.
- [45] G. Zhang,J. Furusho. Speed Control of Two-Inertia System by PI/PID Control. *International Conference on Power Electronics and Drive Systems*, pages 567–572, 1999.
- [46] Zhang G., Furusho J. Vibration Control of Three-Inertia System, *IECON'99 Proceedings*, Vol. 3,pp 1045-1050 ,1999.
- [47] G.D. Magoulas, V.P. Plagianakos, M.N. Vrabatis Development and Convergence Analysis of Training Algorithms with Local Learning Rate Adaptation. *International Journal of Information and Mathematical Sciences*, vol. 1, issue 3, pages 21–26, March 2000.
- [48] G. Ellis,R.D. Lorenz. Resonant Load Control Methods for Industrial Servo Drives. *Industry Applications Conference Proceedings*,vol. 3, pages 1438–1445, 2000
- [49] G. Ellis,Z. Gao. Cures for Low-Frequency Mechanical Resonance in Industrial Servo Systems. *Industry Applications Conference Proceedings*,vol. 1, pages 252–258, 2001
- [50] F.J. Lin, R.J. Wai, "A Hybrid Computed Torque Controller Using Fuzzy Neural Network for Motor-Quick-Return Servo Mechanism", IEEE/ASME Transactions on Mechatronics, Vol. 6, No. 1, pp. 75-89, March 2001.
- [51] M.L. Corradini and G. Orlando, "Robust Stabilization of Nonlinear Uncertain Plants with Backlash or Dead Zone in the Actuator", IEEE Transactions On Control Systems Technology, Vol. 10, No. 1, January 2002.
- [52] Nordin M., Gutman P., "Controlling Mechanical Systems with Backlash - A Survey", *Automatica* Vol. 38, pp 1633-1649, 2002.

- [53] S.C. Ng C.C. Cheung S.H. Leung A. Luk Fast Convergence for Back-Propagation Network with Magnified Gradient Function. *International Journal of Information and Mathematical Sciences*, vol. 1, issue 3, pages 983–988, March 2003.
- [54] K. Jang et. al., "Friction and Output Backlash Compensation of Systems using Neural Network and Fuzzy Logic", Proceedings of the American Control Conference, Massachusetts, pp. 1758-1763, 2004.
- [55] G.B. Huang et. al. An Efficient Sequential Learning Algorithm for Growing and Pruning RBF (GAP-RBF) Networks. *IEEE Transactions on Systems, Man, and Cybernetics*, vol. 34, no. 6, pages 2284–2232, December 2004.
- [56] A. Sabanovic et. al. Sliding Modes in Motion Control Systems. *Automatika*, Vol. 46, No. 1-2, pp. 17–27, 2005
- [57] M. Tallfors Parameter Estimation and Model Based Control Design of Drive Train Systems. *Ph.D. Thesis* , KTH, Stockholm, 2005
- [58] D. Veitch Wavelet Neural Networks and Their Application in the Study of Dynamical Systems. *Department of Mathematics, University of York*, M.Sc. Thesis, August 2005.
- [59] J. Velagic, A. Aksamovic, "Fuzzy Logic System for Position Control and Current Stabilization of a Robot Manipulator", EuroCon 2005, , Belgrade ,Serbia and Montengro, pp. 334-337, November 2005.
- [60] S.J. Yoo,J.B. Park,Y.H. Choi. Stable Predictive Control of Chaotic Systems Using Self-Recurrent Wavelet Neural Network. *International Journal of Control, Automation, and Systems*, vol. 3, no. 1, pages 43–55, March 2005.
- [61] Z. Zainuddin,N. Mahat,Y. Abu Hassan. Improving the Convergence of the Backpropagation Algorithm Using Local Adaptive Techniques. *International Journal of Information and Mathematical Sciences*, vol. 1, issue 3, pages 172–175, March 2005.
- [62] Y. Xu, J. Chen, X. Wang. Robust Vibration Control of Uncertain Flexible Structures With Poles Placement. *ISSCAA Proceedings*,vol. 1, pages 354–358, 2006
- [63] Hosaka M., Murakami T. Vibration Control of Flexible Arm by Multiple Observer Structure, *Electrical Engineering in Japan*, Vol. 154, No. 2, pp. 68-75, 2006.
- [64] T.M. O’Sullivan,C.M. Bingham,N. Schofield. High-Performance Control of Dual-Inertia Servo-Drive Systems Using Low-Cost Integrated SAW Torque Transducers. *IEEE Transactions on Industrial Electronics*, Vol. 53, No. 4, pages 1124–1132, August 2006.

- [65] T. Pajchrowski, "Application of Artificial Neural Network to Robust Speed Control of Servodrive", *IEEE Transactions on Industrial Electronics*, Vol. 54, No. 1, February 2007.
- [66] O'Sullivan T.M., Bingham C.M., Schofield N. "Observer-Based Tuning of Two-Inertia Servo-Drive Systems with Integrated SAW Torque Transducers", *IEEE Transactions on Industrial Electronics*, Vol. 54, No. 2, pp 1080-1091, April 2007.
- [67] K. Szabat, T. Orłowska-Kowalska. Vibration Suppression in a Two-Mass Drive System Using PI Speed Controller and Additional Feedbacks - Comparative Study. *IEEE Transactions on Industrial Electronics*, Vol. 54, No. 2, pages 1193–1206, April 2007.
- [68] Kowalska T., Szabat K. "Control of the Drive System with Stiff and Elastic Couplings Using Adaptive Neuro-Fuzzy Approach", *IEEE Transactions on Industrial Electronics*, pp 228-240, 2007.
- [69] S.J. Yoo, J.B. Park, Y.H. Choi. Indirect Adaptive Control of Nonlinear Dynamic Systems. *Information Sciences*, vol. 177, issue 15, pages 3074–3098, August 2007.
- [70] C.F. Hsu Self-Organizing Adaptive Fuzzy Neural Control for a Class of Nonlinear Systems. *IEEE Transactions on Neural Networks*, vol. 18, no. 4, pages 1232–1241, July 2007.
- [71] C.J. Lin, Y.C. Hsu Reinforcement Hybrid Evolutionary Learning for Recurrent Wavelet-Based Neurofuzzy Systems. *IEEE Transactions on Fuzzy Systems*, vol. 15, no. 4, pages 729–745, August 2007.
- [72] Mahmood I.A., Moheimani R., Bhikkaji B. Precise Tip Positioning of a Flexible Manipulator Using Resonant Control, *IEEE/ASME Transactions on Mechatronics*, Vol. 13, No. 2, pp 180-186, April 2008.
- [73] K. Szabat and T.O. Kowalska Performance Improvement of Industrial Drives with Mechanical Elasticity Using Nonlinear Adaptive Kalman Filter, *IEEE Transactions on Industrial Electronics*, Vol. 55, No. 3, pages 1075–1084, March 2008.
- [74] K. Szabat and T.O. Kowalska Performance Improvement of Industrial Drives with Mechanical Elasticity Using Nonlinear Adaptive Kalman Filter, *IEEE Transactions on Industrial Informatics*, Vol. 4, No. 1, pages 47–57, February 2008.
- [75] G. Kumar et. al., "A Study of a Gun-Turret Assembly in an Armored Tank Using Model Predictive Control", 2009 American Control Conference, St. Louis, MO, USA, June 10-12 2009.

- [76] Guo et. al., "Adaptive Robust Control for Nonlinear System with Input Backlash or Backlash-like Hysteresis", IEEE International Conference on Control and Automation, New Zealand, pp. 1962-1967, 2009.
- [77] S. Chen et. al. , "Friction Modeling and Compensation of Servomechanical Systems with Dual-Relay Feedback Approach", IEEE Transactions on Control, Systems and Technology, Vol. 17, No. 6, pp. 1295-1305, November 2009.
- [78] D.E. Miller, N. Mansouri Model Reference Adaptive Control Using Simultaneous Probing, Estimation, and Control. *IEEE Transactions on Automatic Control*, vol. 55, No 9, pages 2014–2029, September 2010.
- [79] Cychowski M., Jaskiewicz R. Szabat K. Model Predictive Control of an Elastic Three-Mass Drive System with Torque Constraints, *ICIT 2010 Proceedings*, pp 379-385 ,2010.
- [80] Celebi B. et. al. Motion Control and Vibration Suppression of Flexible Lumped Systems via Sensorless LQR Control, *Automatika*, Issue 51, pp 313-324, 2010.
- [81] Cychowski M. et. al. Model Predictive Speed and Vibration Control of Dual-Inertia PMSM Drives. *IEEE ISIE 2011 Proceedings*, pp 1919-1924 ,2011.
- [82] K. Szabat and T.O. Application of the Kalman Filters to the High-Performance Drive System with Elastic Coupling, *IEEE Transactions on Industrial Electronics*, Vol. 55, No. 3, pp. 1075–1084 ,November 2012.
- [83] E.O. Arı, E. Kocaoğlan "Yüksek Başarılı Stabilize Bir Platformun Kontrolü", Otomatik Kontrol Türk Milli Komitesi Ulusal Toplantısı 2012 Bildiri Kitabı, sayfa 874-879, 2012
- [84] Survey of Model Reference Adaptive Control. *Nirma University International Conference on Engineering*, pages 1–6, December 2012.
- [85] E.O. Ari and E. Kocaoglan. Investigation of Interactions between Mechanical and Electrical Components of a Motion Platform. *Asian Control Conference Proceedings*, pp. 1–6, 2013.
- [86] Sincar E., Friction Identification and Compensation in Stabilized Platforms, M.Sc. Thesis, Mechanical Engineering Department, Middle East Technical University, September 2013.
- [87] Yumrukcal Z., Dynamic Modeling of High Precision Servo Systems with Gear Backlash, M.Sc. Thesis, Mechanical Engineering Department, Middle East Technical University, September 2013.
- [88] M. Alizadeh, S. Ganjefar, M. Alizadeh. Wavelet Neural Adaptive Proportional Plus Conventional Integral-Derivative Controller Design of SSSC for Transient Stability Improvement. *Engineering Applications of Artificial Intelligence*, vol. 26, issue 9, pages 2227–2242, October 2013.

- [89] R. Rosa et. al. Evolving Hybrid Neural Fuzzy Network for System Modeling and Time Series Forecasting. *12th International Conference on Machine Learning and Applications*, pages 378–383, July 2013.

APPENDIX A

GENETIC ALGORITHMS USED TO FIT TRANSFER FUNCTION TO FRF DATA

"Genetic Algorithms" (GA), first introduced by John Holland of University of Michigan in the mid 1970s, is a branch of evolutionary computing. This topic is an inspiration from Darwin's theory of evolution. Genetic algorithms uses concepts from the genetics of living creatures, and optimization problems are tried to be solved using a similar approach. If we are solving a problem, we are usually looking for some solution that will be the best among others. The space of all feasible solutions (the set of solutions among which the desired solution resides) is called search space (also state space). Each point in the search space represents one possible solution. Each possible solution can be "marked" by its value (or fitness) for the problem. With GA we look for the best solution among a number of possible solutions - represented by one point in the search space. Looking for a solution is then equal to looking for some extreme value (minimum or maximum) in the search space. At times the search space may be well defined, but usually we know only a few points in the search space. In the process of using GA, the process of finding solutions generates other points (possible solutions) as evolution proceeds. The problem is that the search can be very complicated. One may not know where to look for a solution or where to start. There are many methods one can use for finding a suitable solution, but these methods do not necessarily provide the best solution. Some of these methods are hill climbing, tabu search, simulated annealing and the genetic algorithm. The solutions found by these methods are often considered as good solutions, because it is not often possible to prove what the optimum is. Genetic algorithm begins with a set of solutions (represented by chromosomes) called (initial) population. Solutions from one population

are taken and used to form a new population. This is motivated by a hope, that the new population will be better than the old one. Solutions which are then used to form new solutions (offspring) are selected according to their fitness - the more suitable they are the more chances they have to reproduce. This is repeated until some condition (for example number of populations or improvement of the best solution) is satisfied. Outline of the Basic Genetic Algorithm can be described with the following steps [9]

1. (Start) Generate random population of n chromosomes (suitable solutions for the problem)
2. (Fitness) Evaluate the fitness $f(x)$ of each chromosome x in the population
3. (New population) Create a new population by repeating following steps until the new population is complete
 - (a) (Selection) Select two parent chromosomes from a population according to their fitness (the better fitness, the bigger chance to be selected)
 - (b) (Crossover) With a crossover probability cross over the parents to form new offspring (children). If no crossover was performed, offspring is the exact copy of parents.
 - (c) (Mutation) With a mutation probability mutate new offspring at each locus (position in chromosome).
 - (d) (Accepting) Place new offspring in the new population
4. (Replace) Use new generated population for a further run of the algorithm
5. (Test) If the end condition is satisfied, stop, and return the best solution in current population
6. (Loop) Go to step 2.

Since genetic algorithms is not a basic element of this thesis; but rather used for implementing a search algorithm for system identification; details of it are not given in this study. However, several works concerning this topic may be found in the artificial intelligence literature. For a thorough introduction to the topic of genetic algorithms the reader may refer to [9]. The genetic algorithm search parameters employed in this

study are given in Table A.1. Some performance figures of the algorithm are given in Table A.2.

Table A.1: Parameters of the Genetic Algorithm Used for Transfer Function Fitting to FRF.

PROPERTY	VALUE
Population Size	100
Elite Count	2
Mutation Function	Adaptation of Feasible
Population Range	[0, 240]
Number of Poles (Complex,Real)	3, 3
Number of Zeros (Complex,Real)	2, 3
Selection Function	Stochastic Uniform
Cost Function	Scaled RMS Error

Table A.2: Basic Performance Figures of the Employed Genetic Algorithm.

PROPERTY	VALUE
Initial Average Cost (Scaled)	89
Final Average Cost (Scaled)	1.8
Number of Populations Needed for Convergence	641

CURRICULUM VITAE

PERSONAL INFORMATION

Surname, Name: ARI, Evrim Onur

Nationality: Turkish (TC)

Date and Place of Birth: 25 October 1980, Ankara

Marital Status: Married

Phone: 0542 393 85 04

Fax: 0312 592 30 30

E-mail: eari@cern.ch

EDUCATION

Degree	Institution	Year of Graduation
M.S.	METU Electrical and Electronics Eng.	2005
B.S.,Minor	METU Mechanical Eng. Mechatronics	2003
B.S.	METU Electrical and Electronics Eng.	2002
High School	İncirli High School	1998

PROFESSIONAL EXPERIENCE

Year	Place	Enrollment
2014-Present	CERN / TE-EPC-HPM	Design Engineer
2012-2014	ASELSAN Inc. Unmanned Sys. Dpt.	Lead Design Eng.
2009-2012	ASELSAN Inc. Unmanned Sys. Dpt.	Senior Expert Eng.
2008-2009	Naval Research Center Command	Engineer Lt.
2006-2008	ASELSAN Inc. Electronic Hardware Dpt.	Expert Engineer
2003-2006	ASELSAN Inc. Electronic Hardware Dpt.	Engineer
2002-2003	METU Elec. and Electronics Eng. Dpt.	Res. Assist.
2000-2002	ASELSAN Inc. Electronic Hardware Dpt.	Assistant Engineer

PUBLICATIONS

International Journal Publications

E.O. Ari and E. Kocaoglan. An SRWNN Based Approach on Developing a Self-Learning and Self-Evolving Adaptive Control System for Motion Platforms. *International Journal of Control (under review)*.

International Conference Publications

E.O. Ari and E. Kocaoglan. Controlling a Motion Platform Beyond Its Anti-resonance. *International Federation of Automatic Control World Congress 2014*, pages 1742–1747, 2014.

E.O. Ari and E. Kocaoglan. Investigation of Interactions between Mechanical and Electrical Components of a Motion Platform. *Asian Control Conference Proceedings*, pages 1–6, 2013.

E.O. Ari "Hareketli Bir Platformu Oluşturan Mekanik ve Elektriksel Bileşenler Arası Etkileşimin İncelenmesi", Otomatik Kontrol Türk Milli Komitesi Ulusal Toplantısı 2013 Bildiri Kitabı, sayfa 1001-1006.

E.O. Arı, E. Kocaođlan "Yüksek Başarımlı Stabilize Bir Platformun Kontrolü", Otomatik Kontrol Türk Milli Komitesi Ulusal Toplantısı 2012 Bildiri Kitabı, sayfa 874-879.

A. Erdener, E.O. Arı et. al. "Team Cappadocia Design for MAGIC 2010", Land Warfare Conference 2010, Brisbane.

E.O. Ari, I. Erkmen and A. Erkmen. FACL Based 3D Grasping Controller for a Snake Robot During Locomotion. *Proceedings of International Conference on Intelligent Robots and Systems*, pages 4030–4035, 2006.

E.O. Ari, I. Erkmen and A. Erkmen. A FACL Controller Architecture for a Grasping Snake Robot. *Proceedings of International Conference on Intelligent Robots and Systems*, pages 1478–1753, 2005.